UNIVERSITY OF CALIFORNIA, SAN DIEGO

Development and Applications of Velocity Selectivity in MRI

A dissertation submitted in partial satisfaction of the requirements for the degree of Doctor of Philosophy

in

Bioengineering with a Specialization in Multi-Scale Biology

by

Jia Guo

Committee in charge:

Professor Eric Wong, Chair
Professor Lanping Amy Sung, Co-Chair
Professor Richard Buxton
Professor David Dubowitz
Professor Gabriel Silva

2014

The Dissertation of Jia Guo is approved, and it is acceptable in quality and form for publication on microfilm and electronically:

_____

_____

_____

_____
Co-Chair

_____
Chair

University of California, San Diego

2014

TABLE OF CONTENTS

LIST OF ABBREVIATIONS

ASL	Arterial spin labeling
ATT	Arterial transit time, equivalent to TD
BD	Bolus duration
BGS	Background suppression
BIR	B_1-insensitive rotation
BOLD	Blood oxygenation level dependent
CaO_2	Arterial oxygen content
CBF	Cerebral blood flow
CBV	Cerebral blood volume
$CMRO_2$	Cerebral metabolic rate of oxygen metabolism
CP	Carr-Purcell spin echo train
CPMG	Carr-Purcell-Meiboon-Gill spin echo train
CSF	Cerebral spinal fluid
DRHS	Dual-refocused hyperbolic secant pulses
EC	Eddy current
FOV	Field of view
GM	Gray matter
MRI	Magnetic resonance imaging
OEF	Oxygen extraction fraction
PLD	Post-labeling delay
qBOLD	quantitative BOLD
QUIXOTIC	Quantitative imaging of extraction of oxygen and tissue consumption
RF	Radio frequency
ROI	Region of interest
SE	Spin echo
SNR	Signal-to-noise ratio
TD	Transit delay
TE	Echo time
TI	Time interval between labeling and/or imaging modules
TR	Repetition time
TRUST	T_2-relaxation under spin tagging
VS	Velocity-selective
VSE	Velocity-selective excitation
VSASL	Velocity-selective ASL
VSEAN	Velocity-selective excitation and arterial nulling
VSS	Velocity-selective saturation
WM	White matter

LIST OF SYMBOLS

B_0	Main magnetic field strength
B_1	RF field strength
$D_{GM,WM,CSF}$	Diffusion constant for water in GM, WM and CSF
$M_{x,y}$	Transverse magnetization
M_z	Longitudinal magnetization
T_1	Longitudinal magnetization decay time constant
T_2	Transverse signal decay time constant measured in spin echo experiment
T_2*	Transverse signal decay time constant measured in GRE experiment
V_c	Cut-off velocity
Y	Venous oxygen saturation
α	Labeling efficiency

LIST OF FIGURES

LIST OF TABLES

ACKNOWLEDGEMENTS

I would like to thank Dr. Eric Wong for incredible mentorship, for always being available to talk about experiments, exciting new ideas, or just science and life in general, for making my life as a graduate student fun and exciting and intellectually stimulating.

I would also like to acknowledge Dr. David Dubowitz and Zach Smith for helping me with hypoxia experiments.

Finally, I would like to acknowledge Aaron Simon, Chi Wah (Alec) Wong, David Shin, Kun Lu, and everyone else at the Keck center for functional MRI for their countless useful suggestions and help for improving experiments, solving problems and sharing interesting ideas.

Chapter 1, in full, is a reprint of the material as it appears in Magnetic Resonance in Medicine 2014. Guo J, Meakin JA, Jezzard P, Wong EC. An optimized design to reduce eddy current sensitivity in velocity-selective arterial spin labeling using symmetric BIR-8 pulses. Magn Reson Med 2014. doi: 10.1002/mrm.25227. The dissertation author was the primary investigator and author of this paper.

Chapter 2, in full, has been accepted for publication as it may appear in Magnetic Resonance in Medicine 2014. Guo J, Wong EC. Increased SNR Efficiency in Velocity Selective Arterial Spin Labeling using Multiple Velocity Selective Saturation Modules (mm-VSASL). Magn Reson Med 2014. doi: 10.1002/mrm.25462. The dissertation author is the primary investigator and author of this material.

Chapter 3, in full, is a reprint of the material as it appears in Magnetic Resonance in Medicine 2012. Guo J, Wong EC. Venous oxygenation mapping using velocity-selective excitation and arterial nulling. Magn Reson Med. 2012 Nov;68(5):1458-71. doi: 10.1002/mrm.24145. The dissertation author was the primary investigator and author of this paper.

Chapter 4, in full, is a reprint of the material as it appears in Magnetic Resonance Materials in Physics Biology and Medicine 2012. Wong EC, Guo J. Blind detection of vascular sources and territories using random vessel encoded arterial spin labeling. Magn Reson Mater Phy. 2012 Apr;25(2):95-101. doi: 10.1007/S10334-011-0302-7. The dissertation author was a co-investigator and co-author of this paper.

VITA

2005	Bachelor of Engineering, University of Electronic Science and Technology of China, Chengdu, China
2008	Master of Science, Peking University, Beijing, China
2014	Doctor of Philosophy, University of California, San Diego

PUBLICATIONS

Guo J, Wong EC. Increased SNR Efficiency in Velocity Selective Arterial Spin Labeling using Multiple Velocity Selective Saturation Modules (mm-VSASL). Magn Reson Med 2014. doi: 10.1002/mrm.25462 [In press].

J. Guo, J. Meakin, P. Jezzard, EC. Wong. An Optimized Design to Reduce Eddy Current Sensitivity in Velocity-Selective Arterial Spin Labeling using Symmetric BIR-8 Pulses. Mag. Reson. Med. 2014 Apr 7. doi:10.1002/mrm.25227 [Epub ahead of print].

ZM. Smith, E. Krizay, J. Guo, DD. Shin, M. Scadeng, DJ. Dubowitz. Sustained high-altitude hypoxia increases cerebral oxygen metabolism. J Appl Physiol. 2013 Jan 1;114(1):11-8.

EC. Wong, J. Guo. Blind detection of vascular sources and territories using random vessel encoded arterial spin labeling. MAGMA. 2012 Apr;25(2):95-101.

J. Guo, EC. Wong. Venous oxygenation mapping using velocity-selective excitation and arterial nulling. Magn Reson Med. 2012 Nov;68(5):1458-71.

B. Wu, X. Wang, J. Guo, S. Xie, EC. Wong, J. Zhang, X. Jiang, J. Fang. Collateral circulation imaging: MR perfusion territory arterial spin-labeling at 3T. AJNR Am J Neuroradiol. 2008 Nov;29(10):1855-60.

FIELDS OF STUDY

Major field: Bioengineering (Specialization in Multi-Scale Biology)

Studies in MRI Physics
Professor Eric Wong

ABSTRACT OF THE DISSERTATION

Development and Applications of Velocity Selectivity in MRI

by

Jia Guo

Doctor of Philosophy in Bioengineering with a Specialization in Multi-Scale Biology

University of California, San Diego, 2014

Professor Eric Wong, Chair
Professor Lanping Amy Sung, Co-Chair

Magnetic resonance imaging (MRI) is a powerful and noninvasive tool for measuring brain physiology and functions, including mapping perfusion and oxygen metabolism. Arterial spin labeling (ASL) uses magnetically labeled arterial blood water as an endogenous contrast agent to map regional perfusion. Velocity-selective ASL (VSASL) labels arterial water based on the flow velocity instead of location, eliminating the need for a spatial gap and associated heterogeneous transit delays (TDs) encountered in conventional ASL techniques. However, the

velocity-selective (VS) gradients used under the label condition may generate eddy currents (ECs) and result in artificial perfusion signal from erroneously labeled static tissue. To address this, a VS preparation based on symmetric arrangement of eight-segment B_1-insensitive rotation (BIR-8) RF and gradient pulses (sym-BIR-8) has been developed to effectively minimize the EC effects across a wide range of EC time constants with robust B_0 and B_1 insensitivity. Because VSASL uses saturation instead of inversion, its labeling efficiency is compromised. To improve the signal-to-noise ratio (SNR) efficiency of VSASL, a strategy using multiple VSS modules (mm-VSASL) has been developed, resulting in an SNR efficiency improvement of more than 20% compared to conventional VSASL. In the process of developing mm-VSASL, the TDs of VSASL were measured, providing the first direct evidence of VSASL being insensitive to TD effects in contrast to other ASL techniques. In an application of mapping the venous oxygenation in the brain, the VS preparation was modified to excite the moving arterial and venous spins. With arterial nulling, the intravascular signals in venules were extracted for oxygenation measurement, providing information on the oxygen metabolism of brain tissue *in situ*. In vascular territory imaging, the spins from each supplying artery are labeled uniquely and decoded later to yield the territory information. The planning typically requires prior knowledge of the location of each supplying vessel and may be time consuming or inefficient for detecting collateral flows. To address this, a labeling strategy based on random-encoding the vessels has been developed to label arbitrary number of vessels without planning.

INTRODUCTION

Arterial spin labeling: a completely noninvasive MRI technique to measure blood flow

Blood delivers oxygen and nutrition to tissue. The measurement of the delivering rate of blood flow (perfusion) provides vital information on the function and viability of tissue. There are different techniques for measuring blood flow, such as Xenon-enhanced computerized tomography (XeCT) (1), dynamic perfusion computed tomography (PCT) (2), single photon emission computed tomography (SPECT) (3), positron-emission tomography (PET) using $H_2{}^{15}O$ as contrast agent (4,5), dynamic susceptibility contrast (DSC) MRI (6) and dynamic contrast enhancement (DCE) (7). These techniques require injection or inhalation of contrast agents, some are radioactive, some may cause complications in patients with advanced kidney disease (8). Some of the methods involve ionized radiation in the imaging process, e.g., CT. In contrast, arterial spin labeling (ASL) is a completely noninvasive MRI technique to directly measure blood flow, in which magnetically labeled arterial blood water is used as an endogenous contrast agent. Unlike the other techniques, ASL experiment can be repeated as many times as needed without concerning about the exposure of patients to radiation or the clearance of contrast agent, as the lifetime of the magnetization of labeled water is on the order of a couple of seconds.

ASL was invented in 1992 by Detre and colleagues (9), where the arterial water flowing into the rat brain was magnetically labeled by a series of saturation pulses under one condition (label) and was unperturbed under the other condition (control). The difference of the tissue signals between the two conditions was measured and quantified to yield perfusion maps of rat brain *in vivo*. Later, the same group improved the labeling efficiency by using continuous radiofrequency (RF) pulses to invert instead of saturate arterial spins under the label condition

(continuous ASL, CASL) (10). Since then, different labeling methods have been developed, such as echo-planar imaging and signal targeting with alternating radiofrequency (EPISTAR) (11), flow-sensitive alternating inversion recovery (FAIR) (12,13), proximal inversion with a control for off-resonance effects (PICORE) (14), transfer-insensitive labeling technique (TILT) (15), pseudo-continuous ASL (PCASL) (16,17), velocity-selective ASL (VSASL) (18-20) and variations.

Based on how the labeling process is performed, these different ASL techniques can be categorized into three types (21): 1) CASL, including the original CASL and PCASL; 2) pulsed ASL (PASL), including EPISTAR, FAIR, PICORE and TILT; 3) VSASL.

CASL, PASL and their transit delay effects

In CASL, the magnetization of arterial blood water is continuously inverted as the blood flows through a plane (labeling plane) upstream of the target tissue (imaging slab). Either a combination of continuous and constant RF and gradient waveforms (CASL) (10) or a series of closely placed small-tip RF pulses combined with gradient pulses (PCASL) (16,17) can be used to induce (CASL) or simulate (PCASL) an effect called flow-driven adiabatic inversion (22) as the blood flows through the labeling plane under the label condition.

In PASL, the labeling is done by inversion of the magnetization of a slab containing the feeding arteries upstream of the target tissue with one or a small number of pulses (21). The slab-selective inversion is created by a sharp-edged slab-selective adiabatic inversion pulse (EPISTAR, FAIR and PICORE), or a pair of slab-selective 90° pulses (TILT).

For both the CASL and PASL, it is required to have a gap between the labeling location and the imaging volume, so that the labeling process will have minimal perturbation on the magnetization of tissue in the imaging volume. This gap is bigger for the tissue that is more downstream in the imaging volume. Because of the tortuosity of the vascular structure and the

various velocities of blood in the vasculature, heterogeneous delays are needed for the blood to travel from the labeling site to the tissue at different locations. These delays are called transit delays (TDs). If the images are collected too early, that is, the delay after the labeling process (post-labeling delay, PLD) is not long enough to allow the full length of designated labeling bolus to reach the tissue, the blood flow will be underestimated. On the other hand, if the images are collected too late, the ASL signal will decay unnecessarily more, resulting in reduced signal-to-noise ratio (SNR), as the lifetime of each labeling is on the order of a couple of seconds. In tissues (23,24) or pathologies (25,26) where slow or collateral flows exist, the TDs may be so long that the ASL signal may decay significantly before it can be reliably measured. This may result in completely lack of signal under extreme circumstances. To overcome this limitation of CASL and PASL due to their sensitivity to TD effects, VSASL is desired in these applications because of its TD insensitivity.

Velocity-selective (VS) preparation and VSASL

It has been discovered long ago that position and velocity can be phase encoded by pulsed gradient pulses (27-29). If the gradient pulses are arranged in ways such that their zeroth moment is nulled but the first moment is nonzero, e.g., using bipolar gradient pulses, the gradient pulses are then velocity-sensitive but not position-sensitive, a desired property in VS preparation. Application of VS preparation in ASL was suggested by Norris and Schwazbauer (30), but the first implementation was developed by our lab in 2002 (18), investigated and refined later (19,20).

In VSASL (20), the magnetization of arterial blood spins flowing above a cutoff velocity (V_c) is saturated by global VS preparation (VSS) pulses with the VS gradients turned on under the label condition, and is unperturbed under the control condition with the VS gradients turned off. After a delay period TI for the arterial blood to decelerate along the

vascular tree, the label and the control images are collected with either another VSS module right before or VS gradients embedded in the imaging, so that only signals coming from spins with velocities $V < V_c$ are acquired. With the signal from static tissue subtracted out, the signal difference between these two types of images is solely from the arterial blood delivered during TI. This is because: 1) arterial blood continuously decelerates as it travels down the vascular tree, i.e., from $V \geq V_c$ at labeling to $V < V_c$ at imaging; and 2) venous blood accelerates as it travels up the vascular tree, so the labeled venous blood will be filtered out by the restriction $V < V_c$ in imaging, therefore not contributing to the ASL signal.

In theory, labeled arterial blood decelerates and passes the $V = V_c$ boundary immediately after labeling. With a properly chosen V_c such that the arterial blood with $V < V_c$ is readily located in its destination voxel, VSASL will have zero TDs regardless the location of the voxel, i.e., global labeling. Here the word "global" refers to the field of view (FOV) of the RF coil, within which the magnetization of the voxel can be effectively labeled. To validate this, the TDs of VSASL were directly measured *in vivo* in human subjects by multi-TI experiments, and the first experimental evidence of VSASL being TD-insensitive is presented in Chapter 2.

Taking the advantage of VSASL being TD-insensitive, VSASL can be applied in measurement of pulmonary blood flow (31), where other labeling technique may not be optimal for accurate blood flow quantification because of the heterogeneous TDs. The TD effects in this application are difficult to mitigate with a long PLD (32), because when blood flows by alveoli, there is only limited time before it exit the tissue voxels though venous flow, and the water exchange between the blood and the alveolar tissue is limited due to low proton density in the lungs (20 ~ 30%) (33).

Reduction of eddy current (EC) effects in VSASL

In VSASL for creating non-zero first moment for VS labeling (20), gradients are used under the label condition to, but not under the control condition. The ECs generated by these gradients may interact with the labeling RF pulses, resulting in perturbation of the magnetization of static spins under the label condition, but not under the control condition. As a result, the signal difference created by these ECs gives rise to artificial ASL signal, potentially leading to blood flow overestimation (20,34). Though the EC effects could be small, e.g., less than 1% of the tissue signal; however, because the ASL signal is only on the order of 1-2% of tissue signal, small EC effects may cause significantly errors in VSASL. In the original implementation of VSASL (20), a VS gradient arrangement introduced by Reese et al (35) was adopted to reduce EC effects, especially those from ECs with long time constants. To improve the B_0 and B_1 insensitivity of VSASL, a four-segment B_1-insensitive-rotation (BIR-4) preparation was proposed by our lab (36); however, the gradient arrangement for EC reduction was not compatible with this BIR-4 design. Later in a refinement of VSASL pulse design (34), eight-segmented B_1-insensitive-rotation (BIR-8) preparation was proposed, where Reese's gradient arrangement can be implemented to provide EC reduction and B_0 and B_1 insensitivity. However, this BIR-8 design was not optimized for EC reduction and the effect of inserting delay after each gradient pulse was not explored. To address these issues, I have proposed a symmetric arrangement of the BIR-8 pulses and VS gradients (sym-BIR-8) to optimally cancel ECs with long time constants; while delays inserted after gradient pulses were used to reduce ECs with relatively short time constants. The sym-BIR-8 design was demonstrated by simulations, phantom and *in vivo* experiments to be the most robust VS preparation among all tested VS preparations and across different MR scanners from different venders (GE and Siemens). Details of this work are presented in Chapter 1.

Improvement of SNR efficiency of VSASL

VSASL is insensitive to TD effects. This gives VSASL advantages over other labeling techniques (PASL and CASL) in applications where long and/or heterogeneous TDs are expected; however, the SNR efficiency of VSASL is compromised due to the saturation-based labeling, compared to inversion-based PASL and CASL. As mentioned above, ASL techniques are SNR-limited in essence (ASL signal is on the order of 1-2% of tissue signal), therefore improvement on the SNR efficiency is very important and desired in ASL, especially so in VSASL.

To improve the SNR efficiency in VSASL, I have proposed a strategy of using multiple instead of one VSS modules in the labeling process (mm-VSASL) (37,38), where the extra VSS modules serve mainly as a means to re-label the somewhat relaxed arterial spins for a stronger ASL signal at the time of acquisition. An mm-VSASL signal model was developed and verified to be accurate compared to other more validated ASL techniques (PASL and CASL) by *in vivo* measurement of cerebral blood flow (CBF) in both gray matter (GM) and white matter (WM). Using two VSS modules in VSASL improves the SNR efficiency by about 22%, a good agreement between simulations and *in vivo* experiments.

In the process of designing mm-VSASL, the temporal bolus duration (BD) created by a VSS is needed for accurate quantification of blood flow and optimization of the timing parameters for an optimal SNR efficiency improvement. To measure this parameter, a series of conventional VSASL (with one VSS module) experiments were performed with different TIs to capture the dynamic change of VSASL signal. These ASL signals were fitted to a dynamic ASL model (39) to yield the BDs. As a by-product, the TDs of VSASL were also estimated in the fitting process to be zero, verifying that VSASL is indeed TD-insensitive. For comparison, the TDs and BDs (only PASL) of PCASL and PASL were also measured in the multi-TI experiments.

Details of development of the mm-VSASL signal model, optimization of the labeling timing parameters and related results are presented in Chapter 2.

VS excitation (VSE) and venous oxygenation measurement

Measurement of oxygen metabolism of the brain has very important meanings in understanding the functions of brain, both in normal and diseased states. VS preparation can also be applied in measurement of venous oxygenation. In studies of brain function, the uncoupling of flow and oxygen metabolism gives rise to Blood Oxygenation Level Dependent (BOLD) effect (40). However, due to the complex dynamic interaction between CBF, cerebral blood volume (CBV) and cerebral metabolic rate of O_2 ($CMRO_2$) in BOLD signal (41), more direct measurement of $CMRO_2$ is desired, which can be estimated from oxygen extraction fraction (OEF), CBF and arterial oxygen content (CaO_2): $CMRO_2 = CaO_2*CBF*OEF$, where OEF can be estimated from arterial and venous blood oxygenation difference. Noninvasively MRI-based venous oxygenation measurements include: 1) phase/susceptibility-based methods (42-45), where the measurements are taken from MRI-resolvable veins, and therefore have limited spatial localization as the tissue of interest may reside far from the veins being measured; 2) quantitative BOLD (qBOLD) methods (46-50), where the model is complicated and high SNR is necessary to produce good fitting results (51); and 3) measurement and conversion of T_2/T_2* of venous blood to oxygenation through a model or calibration curve (52-58), where extraction of venous signal from arterial and tissue signals is challenging. Methods that can be performed *in situ* (well-localized with the tissue of interest) and are relatively robust (e.g., not relying on complex modeling) are highly desirable, such as the T_2-based methods that measure venous signal from venules localized in the same voxel with the tissue of interest.

To separate venous signal from tissue and arterial signals, the VS module can be modified to selectively excite (VSE) instead of saturate the magnetization of flowing spins by

an addition of $\pi/2$ phase on the last tip-up RF segment of the VSS module. Arterial signal is removed from the measurement by inverting and imaging at the null point of the arterial magnetization. Hence this method is named velocity-selective excitation with arterial nulling (VSEAN) (59,60). Compared to a similar method called QUIXOTIC (61), where accelerating venous blood is selected by applications of VSS modules and subtraction of signals measured under different conditions, VSEAN provides: 1) higher venous signal by preserving the tissue signal from which the venous blood is originated; 2) improved temporal efficiency by using a signal-projection methods, which only requires a small number of reference images in addition to the actual measurements, whereas QUIXOTIC requires half of the images to be "reference" images; 3) measurements free of artifacts from EC effects and cerebrospinal fluid (CSF) contamination due to diffusion attenuation, whereas QUIXOTIC is demonstrated to be contaminated by these artifacts (60,61), resulting in elevated venous T_2 and therefore oxygenation estimates.

The implementation of VSEAN and its performance in measuring venous oxygenation both *in situ* in GM and in sagittal sinus (SS) are detailed in Chapter 3.

Vessel-encoded ASL: from optimized to randomized encoding

In clinical applications such as imaging of stroke, cerebrovascular diseases, and planning of treatment for tumors, vessel territory information, i.e., which artery supplies a certain region of tissue, is very useful, in addition to the blood flow information. ASL-based vessel territory imaging techniques include ones that label a single source vessel at a time (62-64) and those that simultaneously encode a few vessels at a time and decode the territory information later (65-67). In vessel-encoded PCASL (VEPCASL), all the source vessels are simultaneously encoded in a series of labeling steps. Uniquely labeling patterns is generated and decoded for each vessel to yield its territory information. VEPCASL utilizes Hadamard

encoding matrix in the labeling/encoding process for an optimal temporal efficiency (66-68). However, as the position of target vessels in the labeling plane is typically not regular and varies across people, planning of Hadamard encoding more than three vessels may be not straightforward by simple geometrical calculation. This may lead to sub-optimized labeling efficiency and compromised SNR, especially in cases a large number of vessels to be encoded, e.g., labeling vessels above the Circle of Willis (CoW).

To improve the overall labeling efficiency and simplify the planning, the labeling profile of VEPCASL *in vivo* is measured and modeled, and a numerical optimization process on the choice of the vessel-encoding gradients (e.g., gradient strength and direction) is performed for an optimized (Hadamard encoding) labeling strategy (69). This method can in theory realize Hadamard encoding for any given vessel location and in practice works well in a typical VEPCASL experiment labeling vessels below the CoW; however, due to the hardware limitation of the scanner (performance of the gradient system), off-resonance effects in the labeling plane, and the complexity of optimization algorithm, it is still time-consuming to plan and optimize the encoding strategy for labeling of a large number of vessels in practice. In addition, there is also clinical interest of imaging territories of collateral flows (70), in which case the supplying vessels may be unknown at the time of planning. These reasons promoted our development of VEPCASL using a randomized encoding strategy (re-VEPCASL) (71,72). Re-VEPCASL works for arbitrary number of vessels (including those unknown collateral source vessels) in the labeling plane without any planning before the scan. It also handles the off-resonance effects to produce unbiased perfusion estimates. Details of the work on re-VEPCASL are presented in Chapter 4.

References

1. Gur D, Good WF, Wolfson SK, Yonas H, Shabason L. Invivo Mapping of Local Cerebral Blood-Flow by Xenon-Enhanced Computed-Tomography. Science 1982;215(4537):1267-1268.

2. Axel L. Cerebral Blood-Flow Determination by Rapid-Sequence Computed-Tomography - a Theoretical-Analysis. Radiology 1980;137(3):679-686.

3. Warwick JM. Imaging of brain function using SPECT. Metab Brain Dis 2004;19(1-2):113-123.

4. Frackowiak RSJ, Lenzi GL, Jones T, Heather JD. Quantitative Measurement of Regional Cerebral Blood-Flow and Oxygen-Metabolism in Man Using O-15 and Positron Emission Tomography - Theory, Procedure, and Normal Values. J Comput Assist Tomogr 1980;4(6):727-736.

5. Raichle ME, Martin WRW, Herscovitch P, Mintun MA, Markham J. Brain Blood-Flow Measured with Intravenous (H2o)-O-15 .2. Implementation and Validation. J Nucl Med 1983;24(9):790-798.

6. Rosen BR, Belliveau JW, Vevea JM, Brady TJ. Perfusion imaging with NMR contrast agents. Magn Reson Med 1990;14:249-265.

7. Tofts PS, Brix G, Buckley DL, Evelhoch JL, Henderson E, Knopp M, Larsson HBW, Lee TY, Mayr NA, Parker GJM, Port RE, Taylor J, Weisskoff RM. Estimating kinetic parameters from dynamic contrast-enhanced T(1)-weighted MRI of a diffusable tracer: Standardized quantities and symbols. J Magn Reson Imaging 1999;10(3):223-232.

8. Perazella MA. Current Status of Gadolinium Toxicity in Patients with Kidney Disease. Clin J Am Soc Nephrol 2009;4(2):461-469.

9. Detre JA, Leigh JS, Williams DS, Koretsky AP. Perfusion imaging. Magn Reson Med 1992;23(1):37-45.

10. Williams DS, Detre JA, Leigh JS, Koretsky AP. Magnetic-Resonance-Imaging of Perfusion Using Spin Inversion of Arterial Water. Proc Natl Acad Sci U S A 1992;89(1):212-216.

11. Edelman RR, Siewert B, Darby DG, Thangaraj V, Nobre AC, Mesulam MM, Warach S. Qualitative mapping of cerebral blood flow and functional localization with echo-planar MR imaging and signal targeting with alternating radio frequency. Radiology 1994;192(2):513-520.

12. Kim SG. Quantification of relative cerebral blood flow change by flow-sensitive alternating inversion recovery (FAIR) technique: application to functional mapping. Magn Reson Med 1995;34(3):293-301.

13. Kwong KK, Chesler DA, Weisskoff RM, Donahue KM, Davis TL, Ostergaard L, Campbell TA, Rosen BR. MR perfusion studies with T1-weighted echo planar imaging. Magn Reson Med 1995;34(6):878-887.

14. Wong EC, Buxton RB, Frank LR. Implementation of quantitative perfusion imaging techniques for functional brain mapping using pulsed arterial spin labeling. NMR Biomed 1997;10(4-5):237-249.

15. Golay X, Stuber M, Pruessmann KP, Meier D, Boesiger P. Transfer insensitive labeling technique (TILT): application to multislice functional perfusion imaging. J Magn Reson Imaging 1999;9(3):454-461.

16. Garcia DM, de Bazelaire C, Alsop D. Pseudo-continuous flow driven adiabatic inversion for arterial spin labeling. In Proceedings of the 13 th Annual Meeting of ISMRM; Miami, Florida, USA. 2005. p. 37.

17. Dai WY, Garcia D, de Bazelaire C, Alsop DC. Continuous Flow-Driven Inversion for Arterial Spin Labeling Using Pulsed Radio Frequency and Gradient Fields. Magn Reson Med 2008;60(6):1488-1497.

18. Wong EC, Liu T, Sidaros K, Frank LR, Buxton RB. Velocity selective arterial spin labeling. In Proceedings of the 10 th Annual Meeting of ISMRM; Honolulu, Hawai'i, USA. 2002. p. 621.

19. Duhamel G, de Bazelaire Cd, Alsop DC. Evaluation of systematic quantification errors in velocity-selective arterial spin labeling of the brain. Magn Reson Med 2003;50(1):145-153.

20. Wong EC, Cronin M, Wu W-C, Inglis B, Frank LR, Liu TT. Velocity Selective Arterial Spin Labeling. Magn Reson Med 2006;55:1334-1341.

21. Wong EC. An introduction to ASL labeling techniques. J Magn Reson Imaging 2014;40(1):1-10.

22. Dixon WT. Simple proton spectroscopic imaging. Radiology 1984;153:189-194.

23. Wu WC, Wang J, Detre JA, Ratcliffe SJ, Floyd TF. Transit delay and flow quantification in muscle with continuous arterial spin labeling perfusion-MRI. J Magn Reson Imaging 2008;28(2):445-452.

24. van Osch MJP, Teeuwisse WM, van Walderveen MAA, Hendrikse J, Kies DA, van Buchem MA. Can Arterial Spin Labeling Detect White Matter Perfusion Signal? Magn Reson Med 2009;62(1):165-173.

25. Bokkers RPH, Bremmer JP, van Berckel BNM, Lammertsma AA, Hendrikse J, Pluim JPW, Kappelle LJ, Boellaard R, Klijn CJM. Arterial spin labeling perfusion MRI at multiple delay times: a correlative study with (H2O)-O-15 positron emission tomography in patients with symptomatic carotid artery occlusion. J Cereb Blood Flow Metab 2010;30(1):222-229.

26. Yun TJ, Sohn CH, Han MH, Kang HS, Kim JE, Yoon BW, Paeng JC, Choi SH, Kim JH, Song IC, Chang KH. Effect of delayed transit time on arterial spin labeling: correlation with dynamic susceptibility contrast perfusion magnetic resonance in moyamoya disease. Invest Radiol 2013;48(11):795-802.

27. Hahn EL. Detection of Sea-Water Motion by Nuclear Precession. J Geophys Res 1960;65(2):776-777.

28. Moran PR. A flow velocity zeugmatographic interlace for NMR imaging in humans. Magn Reson Imaging 1982;1(4):197-203.

29. Redpath TW, Norris DG, Jones RA, Hutchison JM. A new method of NMR flow imaging. Phys Med Biol 1984;29(7):891-895.

30. Norris DG, Schwartzbauer C. Velocity Selective Radiofrequency Pulse Trains. J Magn Reson 1999;137:231-236.

31. Guo J, Wong EC. Pulmonary Blood Flow Measurement using Velocity-Selective Arterial Spin Labeling at 3.0T. In Proceedings of the 21 st Annual Meeting of ISMRM; Salt Lake City, Utah, USA. 2013. p. 6823.

32. Bolar DS, Levin DL, Hopkins SR, Frank LF, Liu TT, Wong EC, Buxton RB. Quantification of regional pulmonary blood flow using ASL-FAIRER. Magn Reson Med 2006;55(6):1308-1317.

33. Harris P, Heath D. The human pulmonary circulation : its form and function in health and disease. Edinburgh ; New York: Churchill Livingstone; 1986. xiv, 702 p. p.

34. Meakin JA, Jezzard P. An optimized velocity selective arterial spin labeling module with reduced eddy current sensitivity for improved perfusion quantification. Magn Reson Med 2013;69(3):832-838.

35. Reese TG, Heid O, Weisskoff RM, Wedeen VJ. Reduction of eddy-current-induced distortion in diffusion MRI using a twice-refocused spin echo. Magn Reson Med 2003;49(1):177-182.

36. Wong EC, Guo J. BIR-4 based B1 and B0 insensitive velocity selective pulse trains. In Proceedings of the 18 th Annual Meeting of ISMRM; Stockholm, Sweden. 2010. p. 2853.

37. Guo J, Wong EC. Increased Tagging Efficiency in Velocity Selective ASL using Multiple Velocity Selective Saturation Modules. In Proceedings of the 19 th Annual Meeting of ISMRM; Montréal, Québec, Canada. 2011. p. 296.

38. Guo J, Wong EC. Increased SNR Efficiency in Velocity Selective Arterial Spin Labeling using Multiple Velocity Selective Saturation Modules (mm-VSASL). Magn Reson Med 2014. doi: 10.1002/mrm.25462 [In press].

39. Buxton RB, Frank LR, Wong EC, Siewert B, Warach S, Edelman RR. A general kinetic model for quantitative perfusion imaging with arterial spin labeling. Magn Reson Med 1998;40:383-396.

40. Ogawa S, Lee T-M. Magnetic resonance imaging of blood vessels at high fields: in vivo and in vitro measurements and image simulation. Magn Reson Med 1990;16:9-18.

41. Buxton RB. Introduction to functional magnetic resonance imaging : principles and techniques. Cambridge ; New York: Cambridge University Press; 2009. 457 p. p.

42. Jain V, Langham MC, Wehrli FW. MRI estimation of global brain oxygen consumption rate. J Cereb Blood Flow Metab 2010;30(9):1598-1607.

43. Fernández-Seara MA, Techawiboonwong A, Detre JA, Wehrli FW. MR susceptometry for measuring global brain oxygen extraction. Magn Reson Med 2006;55(5):967-973.

44. Haacke EM, Lai S, Reichenbach JR, Kuppusamy K, Hoogenraad FGC, Takeichi H, Lin WL. In vivo measurement of blood oxygen saturation using magnetic resonance imaging: A direct validation of the blood oxygen level-dependent concept in functional brain imaging. Hum Brain Mapp 1997;5(5):341-346.

45. Fan AP, Bilgic B, Gagnon L, Witzel T, Bhat H, Rosen BR, Adalsteinsson E. Quantitative oxygenation venography from MRI phase. Magn Reson Med 2014;72(1):149-159.

46. He X, Yablonskiy DA. Quantitative BOLD: Mapping of human cerebral deoxygenated blood volume and oxygen extraction fraction: Default state. Magn Reson Med 2007;57(1):115-126.

47. Yablonskiy DA, Haacke EM. Theory of Nmr Signal Behavior in Magnetically Inhomogeneous Tissues - the Static Dephasing Regime. Magn Reson Med 1994;32(6):749-763.

48. Christen T, Lemasson B, Pannetier N, Farion R, Segebarth C, Remy C, Barbier EL. Evaluation of a quantitative blood oxygenation level-dependent (qBOLD) approach to map local blood oxygen saturation. NMR Biomed 2011;24(4):393-403.

49. Lu HZ, van Zijl PCM. Experimental measurement of extravascular parenchymal BOLD effects and tissue oxygen extraction fractions using multi-echo VASO fMRI at 1.5 and 3.0 T. Magn Reson Med 2005;53(4):808-816.

50. An HY, Lin WL. Quantitative measurements of cerebral blood oxygen saturation using magnetic resonance imaging. J Cereb Blood Flow Metab 2000;20(8):1225-1236.

51. Yablonskiy DA. Quantitation of intrinsic magnetic susceptibility-related effects in a tissue matrix. Phantom study. Magn Reson Med 1998;39(3):417-428.

52. Foltz WD, Merchant N, Downar R, Stainsby TA, Wright GA. Coronary venous oximetry using MRI. Magn Reson Med 1999;42(5):837-848.

53. Oja JM, Gillen JS, Kauppinen RA, Kraut M, van Zijl PC. Determination of oxygen extraction ratios by magnetic resonance imaging. J Cereb Blood Flow Metab 1999;19(12):1289-1295.

54. Golay X, Silvennoinen MJ, Zhou J, Clingman CS, Kauppinen RA, Pekar JJ, van Zij PC. Measurement of tissue oxygen extraction ratios from venous blood T(2): increased precision and validation of principle. Magn Reson Med 2001;46(2):282-291.

55. Wright GA, Hu BS, Macovski A. Estimating Oxygen Saturation of Blood In vivo with MR Imaging at 1.5T. J Magn Reson Im 1991;1(3):275-283.

56. Chien D, Levin DL, Anderson CM. MR gradient echo imaging of intravascular blood oxygenation: T2* determination in the presence of flow. Magn Reson Med 1994;32(4):540-545.

57. Lee T, Stainsby JA, Hong J, Han E, Brittain J, Wright GA. Blood Relaxation Properties at 3T -- Effects of Blood Oxygen Saturation. In Proceedings of the 11 th Annual Meeting of Proc Intl Soc Mag Reson Med. 2003. p. 131.

58. Lu HZ, Ge YL. Quantitative evaluation of oxygenation in venous vessels using T2-Relaxation-Under-Spin-Tagging MRI. Magn Reson Med 2008;60(2):357-363.

59. Guo J, Wong EC. Imaging of Oxygen Extraction Fraction Using Velocity Selective Excitation with Arterial Nulling (VSEAN). In Proceedings of the 18 th Annual Meeting of ISMRM; Stockholm, Sweden. 2010. p. 4057.

60. Guo J, Wong EC. Venous oxygenation mapping using velocity-selective excitation and arterial nulling. Magn Reson Med 2012;68(5):1458-1471.

61. Bolar DS, Rosen BR, Sorensen AG, Adalsteinsson E. QUantitative Imaging of eXtraction of Oxygen and TIssue Consumption (QUIXOTIC) Using Venular-Targeted Velocity-Selective Spin Labeling. Magn Reson Med 2011;66(6):1550-1562.

62. Davies NP, Jezzard P. Selective arterial spin Labeling (SASL): Perfusion territory mapping of selected feeding arteries tagged using two-dimensional radiofrequency pulses. Magn Reson Med 2003;49(6):1133-1142.

63. Werner R, Norris DG, Alfke K, Mehdorn HM, Jansen O. Continuous artery-selective spin labeling (CASSL). Magn Reson Med 2005;53(5):1006-1012.

64. Helle M, Norris DG, Rufer S, Alfke K, Jansen O, van Osch MJP. Superselective Pseudocontinuous Arterial Spin Labeling. Magn Reson Med 2010;64(3):777-786.

65. Zimine I, Petersen ET, Golay X. Dual vessel arterial spin labeling scheme for regional perfusion imaging. Magn Reson Med 2006;56(5):1140-1144.

66. Gunther M. Efficient visualization of vascular territories in the human brain by cycled arterial spin labeling MRI. Magn Reson Med 2006;56(3):671-675.

67. Wong EC. Vessel-encoded arterial spin-labeling using pseudocontinuous tagging. Magn Reson Med 2007;58(6):1086-1091.

68. Okell TW, Chappell MA, Kelly ME, Jezzard P. Cerebral blood flow quantification using vessel-encoded arterial spin labeling. J Cereb Blood Flow Metab 2013;33(11):1716-1724.

69. Guo J, Wong EC. Optimization of the encoding scheme for improved SNR efficiency in Vessel Encoded Pseudo-Continuous ASL. In Proceedings of the th Annual Meeting of ISMRM; Honolulu, Hawai'i, USA. 17. 2009. p. 1522.

70. Wu B, Wang X, Guo J, Xie S, Wong EC, Zhang J, Jiang X, Fang J. Collateral Circulation Imaging: MR Perfusion Territory Arterial Spin-Labeling at 3T. Am J Neuroradiol 2008;29(10):1855-1860.

71. Guo J, Wong EC. From optimized Vessel Encoded PCASL (opt-VEPCASL) to randomly-encoded VEPCASL (re-VEPCASL). In Proceedings of the 18 th Annual Meeting of ISMRM; Stockholm, Sweden. 2010. p. 4069.

72. Wong EC, Guo J. Blind detection of vascular sources and territories using random vessel encoded arterial spin labeling. Magn Reson Mater Phy 2012;25(2):95-101.

CHAPTER 1 : An Optimized Design to Reduce Eddy Current Sensitivity in Velocity-Selective Arterial Spin Labeling Using Symmetric BIR-8 Pulses

Jia Guo,[1]* James A. Meakin,[2†] Peter Jezzard,[2] and Eric C. Wong[3,4]

Purpose: Velocity-selective arterial spin labeling (VSASL) tags arterial blood on a velocity-selective (VS) basis and eliminates the tagging/imaging gap and associated transit delay sensitivity observed in other ASL tagging methods. However, the flow-weighting gradient pulses in VS tag preparation can generate eddy currents (ECs), which may erroneously tag the static tissue and create artificial perfusion signal, compromising the accuracy of perfusion quantification.

Methods: A novel VS preparation design is presented using an eight-segment B_1 insensitive rotation with symmetric radio frequency and gradient layouts (sym-BIR-8), combined with delays after gradient pulses to optimally reduce ECs of a wide range of time constants while maintaining B_0 and B_1 insensitivity. Bloch simulation, phantom, and in vivo experiments were carried out to determine robustness of the new and existing pulse designs to ECs, B_0, and B_1 inhomogeneity.

Results: VSASL with reduced EC sensitivity across a wide range of EC time constants was achieved with the proposed sym-BIR-8 design, and the accuracy of cerebral blood flow measurement was improved.

Conclusion: The sym-BIR-8 design performed the most robustly among the existing VS tagging designs, and should benefit studies using VS preparation with improved accuracy and reliability. **Magn Reson Med 000:000–000, 2014. © 2014 Wiley Periodicals, Inc.**

Key words: arterial spin labeling; BIR-8; eddy current; perfusion; velocity-selective ASL

INTRODUCTION

Arterial spin labeling (ASL) uses magnetically tagged arterial blood water as an endogenous contrast agent to measure local tissue perfusion. In conventional ASL (1–6), a gap between the tagging and imaging regions is required to minimize any undesired perturbation of the tissue magnetization. This gap can result in inhomogeneous transit delays, confounding the quantification with incomplete inflow if an insufficient postlabeling delay (PLD) is used or reduced signal-to-noise-ration (SNR) if an unnecessarily long PLD is used. Methods (7–9) proposed to reduce the transit delay sensitivity may not always be effective in cases where slow or collateral flow conditions exist (10–13). To overcome these difficulties, velocity-selective ASL (VSASL) (14) labels spins on the basis of flow velocity rather than spatial position. With a proper choice of cutoff velocity (V_c), the gap as well as the associated inhomogeneous transit delays in conventional ASL can be eliminated.

In VSASL, flow-weighting gradient pulses in the preparation module are applied only under the tag condition. However, these pulses may generate eddy currents (ECs) and result in artificial perfusion signal from erroneously tagged static tissue (14,15). To minimize this artifact, gradient pulses can be arranged to largely cancel out the ECs (14,16). Recently a VSASL tagging module based on an eight-segment B_1 insensitive rotation (BIR-8) was introduced (15) to reduce the EC effects while also achieving B_0 and B_1 insensitivity. Due to its asymmetric layout, it is referred to as asym-BIR-8 here. In this study, we introduce a novel design using BIR-8 RF pulses with symmetric RF and gradient layouts (referred to as sym-BIR-8) that further improves EC compensation while preserving the B_0 and B_1 insensitivity of the original asym-BIR-8. In addition, we explored the effect of inserting delays after gradient pulses on EC sensitivity reduction.

THEORY

The ECs generated by a gradient waveform can be modeled as a few components, each with different initial EC amplitude and following exponential decays of different time constants (17). The ECs of short time constants usually decay away quickly, so delays can be placed after gradient pulses to minimize their interaction with following radio frequency (RF) pulses. For the ECs of long time constants, because it may not be practical to use sufficiently long delays, an EC-compensating gradient layout is needed. Below we compare two EC compensating layouts: asym-BIR-8 and sym-BIR-8.

In the following derivations, a single exponential decay with a time constant T is considered. The ECs generated by a trapezoidal waveform can be modeled as (15,17):

[1]Department of Bioengineering, University of California, San Diego, La Jolla, California, USA.

[2]Centre for Functional Magnetic Resonance Imaging of the Brain, Nuffield Department of Clinical Neurosciences, University of Oxford, Oxford, United Kingdom.

[3]Department of Radiology, University of California, San Diego, La Jolla, California, USA.

[4]Department of Psychiatry, University of California, San Diego, La Jolla, California, USA

Grant sponsor: NIH; Grant number: R01 EB002096; Grant sponsor: Cancer Research UK; Grant sponsor: Engineering and Physical Sciences Research Council.

*Correspondence to: Jia Guo, MS, UCSD Center for Functional MRI, 9500 Gilman Drive, MC 0677, La Jolla, CA 92093-0677. E-mail: jguo@ucsd.edu

†Now at: Philips Medical Systems, Best, The Netherlands.

Received 15 November 2013; revised 21 February 2014; accepted 27 February 2014

DOI 10.1002/mrm.25227

Published online 00 Month 2014 in Wiley Online Library (wileyonlinelibrary.com).

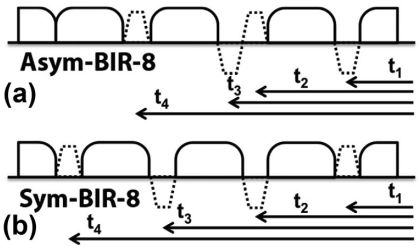

FIG. 1. Diagrams of VS preparation pulses using asym-BIR-8 module **(a)** and sym-BIR-8 module **(b)**. The solid and dashed shapes represent RF and gradient pulses, respectively. The times t_1–t_4 are counted from an arbitrary reference time point after the gradient pulses to the center of gradient lobes.

$$g = g_0\left(e^{-\frac{t-t_a}{T}} - e^{-\frac{t-t_d}{T}}\right) = g_o c e^{-\frac{t}{T}}, \quad [1]$$

where $c = (e^{\frac{t_a}{T}} - e^{\frac{t_d}{T}}), t_a$ and t_d, are the times of the rise and fall portions of the trapezoid, t is the time from the initial start of the sequence, and g_o is the initial amplitude of the gradient generated by EC at the end of the ramp for each transition. Assuming that the gradient pulses have the same shape and size (Fig. 1), therefore having the same g_o and c:

$$g_{asym} = g_o c\left(-e^{-\frac{t_1}{T}} + e^{-\frac{t_2}{T}} - e^{-\frac{t_3}{T}} + e^{-\frac{t_4}{T}}\right) \text{ for asym-BIR-8 module}, \quad [2]$$

$$\text{and } g_{sym} = g_o c\left(e^{-\frac{t_1}{T}} - e^{-\frac{t_2}{T}} - e^{-\frac{t_3}{T}} + e^{-\frac{t_4}{T}}\right) \text{ for sym-BIR-8 module}, \quad [3]$$

where $t_{1–4}$ are counted from an arbitrary reference time point after the gradient pulses.

Given a relatively long time constant, $T \gg t_1, t_2, t_3, t_4$, the expressions can be simplified by first-order Taylor expansion to:

$$g_{asym} = \frac{g_o c(t_1 - t_2 + t_3 - t_4)}{T}, \quad [4]$$

$$\text{and } g_{sym} = \frac{g_o c(-t_1 + t_2 + t_3 - t_4)}{T}. \quad [5]$$

For asym-BIR-8, $t_2 \approx t_3$, so $g_{asym} \approx \frac{g_o c(t_1 - t_4)}{T}$. For sym-BIR-8, because of the symmetric layout of the gradient pulses, $t_1 + t_4 = t_2 + t_3$, so $g_{sym} = 0$, the EC cancellation is optimal. If there are delays before and/or after the gradient pulses, the cancellation remains optimal as long as the condition of symmetry is satisfied. Note that this optimal EC cancellation is only valid for long time constants and at any time points after all the gradient pulses are applied.

METHODS

In this study, double refocused hyperbolic secant (DRHS) (14), four-segment B_1 insensitive rotation (BIR–4) (18), asym-BIR-8 (15), and two modifications denoted as asym-BIR-8 M. 1 and M. 2, and sym-BIR-8 (Fig. 2) were compared. Asym-BIR-8 M.2 had one delay between the first two RF subpulses and one delay after each of the first, the third, and the fourth gradient pulses. The total durations in the odd and even sections of BIR-8 subpulses were matched (15,19). For DRHS, BIR-4, asym-BIR-8 M. 1, and sym-BIR-8, the delays of equal length were placed after each of the gradient pulses. Note that in BIR-4 there were only two delays instead of four.

Bloch Simulations

The performance of these velocity-selective (VS) tagging modules with and without delays was compared using Bloch simulation implemented in MATLAB 2012a (The Mathworks, Nantick, USA). The RF subpulses used in BIR-4 and BIR-8 are tanh/tan-modulated with a length of 1.5 ms each, ω_{max} of 42.52 kHz, ξ of 43.58 and tan(κ) of 69.65 as defined in (20). The tip-down and tip-up pulses in DRHS module were hard 90° pulses. The hyperbolic secant (HS) pulses were 5.08 ms each with β of 700 Hz and μ of 6, and were transformed into the form $\cos^n(t)$ with $n = 0.2$ (14). The V_c was set to 2 cm/s.

First, the sensitivity of the VS modules to B_1, off-resonance (B_0) and EC effects were simulated without any delay times. For the B_1 sensitivity simulation, a B_1 range of 11 μT to 26 μT was used, with 23 μT treated as a nominal maximum B_1 (100%). The B_1 required to maintain 95% M_z after a 360° rotation were 10.5 μT for the HS pulses, 11.9 μT for BIR-4, and 13.0 μT for asym-BIR-8 and sym-BIR-8. For the B_0 sensitivity simulation, resonance offset ranging from −500 Hz to +500 Hz was used, with B_1 set to 23 μT. In DRHS, the delay between the pair of HS pulses was adjusted to minimize its off-resonance sensitivity. To examine the perturbation of static spins, the longitudinal magnetization after applying VS modules was simulated [as described in (15), with a time step of 2 μs]. EC amplitude of 0.25% and time constants of 0.1 ms to 1,000 ms were used. Gradient pulses with a ramp time of 0.5 ms and a maximum amplitude (G_{max}) of 50 mT/m were used. Relaxation effects were ignored.

The EC sensitivity was simulated with different delays (2.54 ms for DRHS; 10 ms for BIR-4; 3 ms for asym-BIR-8 M. 1 and M. 2 and sym-BIR-8) such that the total duration of each VS module was kept the same; thus, the EC sensitivity can be compared under similar T_2 decay and SNR conditions.

Phantom Experiments

DRHS, BIR-4, asym-BIR-8 M. 1 and 2, and sym-BIR-8 were implemented on a 3-Tesla GE scanner (Discovery MR750; GE Healthcare, Waukesha, WI)—referred to as scanner A—with an 8-channel receive-only coil and a 3-Tesla Siemens scanner (Verio; Siemens Healthcare, Erlangen, Germany)—referred to as scanner B—with a 12-channel receive-only coil. Empirically, we found that the ECs were substantially different on these two scanners; thus, the EC sensitivity and the robustness of the VS preparations could be tested under different EC conditions. A delay of 0.1 ms was placed before each gradient pulse. Spherical silicone oil phantoms were used because silicone's diffusion coefficient is very low (21); thus, the signal difference between tag and control conditions should solely reflect the artifacts generated by EC

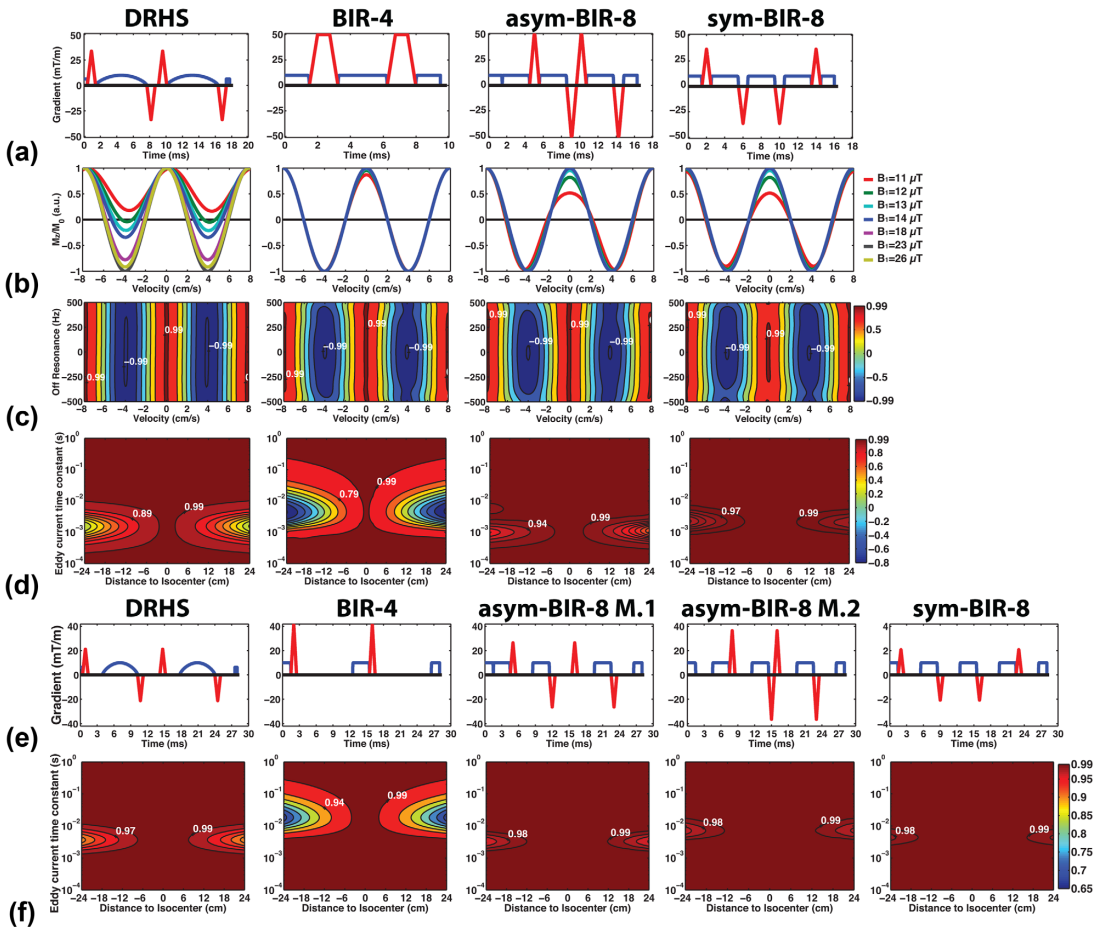

FIG. 2. Diagrams and simulation results of the VS preparation modules without **(a–d)** and with **(e–f)** delays inserted between RF and gradient pulses. (a) Diagrams of DRHS, BIR–4, asym-BIR-8, and sym-BIR-8 pulses, where the red shapes represent the RF pulses and the blue shapes represent the gradient pulses; with the gradient amplitude labeled, the ramp time and G_{max} were fixed to 0.5 ms and 50 mT/m, accordingly, with $V_c = 2$ cm/s. (b) Simulated magnetization at different B_1 levels and velocities after applying corresponding VS tagging pulses in (a). (c) The off-resonance responses of the tagging pulses at a nominal B_1 of 23 μT. (d) Simulated magnetization of static spins under EC effects after applying VS tagging modules in (a), showing sensitivity of the pulses to ECs of different time constants at various distances away from the isocenter. (e) Diagrams of the VS preparation modules with 3-ms delays inserted after gradient pulses (asym-BIR-8 M. 1 and asym-BIR-8 M. 2 are two modifications of the original asym-BIR-8 design with delays inserted). (f) Simulated magnetization of static spins under EC effects after applying VS tagging modules in (e).

effects. The phantoms were placed at the isocenter of the magnets. Images were collected 10 ms after the VS preparation modules with tag and control conditions alternating across repetitions. The VS gradient pulses were applied in the VS preparation modules with a ramp time of 0.5 ms, $V_c = 1$ cm/s and 2 cm/s, and on each of the three principal axes: A/P and L/R acquired in axial scans and S/I in sagittal scans. There was no VS gradient pulse in the image acquisition portion.

To test the effects of inserting delays, experiments were carried out with the length of the delays to be [0.5, 1, 1.5, 2, 3, 4] ms in sym-BIR-8 and [0.5, 1, 2, 4, 6, 8] ms in BIR-4. The G_{max} was set to 20 mT/m. 15 pairs of tag, and control images were collected after four dummy repetitions. Other imaging parameters included: on scanner A, single-shot gradient echo with sinc excitation pulse and spiral-out readout, single slice with field of view (FOV) 200 × 200 × 8 mm, matrix size 64 × 64, and repetition time (TR)/echo time (TE) = 3 s/3 ms; on scanner B, single-shot gradient echo with sinc excitation and EPI readout, single slice with FOV 200 × 200 × 8 mm, matrix size 64 × 64, and TR/TE = 3 s/20 ms.

The performance of each VS module was investigated with combinations of V_c, G_{max}, and gradient directions. At $V_c = 1$ cm/s, the G_{max} were [15, 25, 35, 45] mT/m on scanner A and [15, 25, 35, 43] mT/m on scanner B due to its hardware limitation; and at $V_c = 2$ cm/s, the G_{max} were [15, 20, 25] mT/m. The rise time of the VS

Table 1
Delays, Total Duration (unit ms), and b-Values (in the In Vivo Experiments, Unit s/mm^2) Used in the Phantom and In Vivo Experiments

	V_c (cm/s)	G_{max} (mT/m)	DRHS	BIR-4	Asym-BIR-8 M. 1	Asym-BIR-8 M. 2	Sym-BIR-8	Total
Phantom	2	15	2.00	7.50	1.70	1.50	1.94	25.3
		20	1.94	7.34	1.66	1.50	1.86	24.3
		25	1.90	7.24	1.66	1.50	1.82	23.7
	1	15	2.20	7.90	1.78	1.50	2.14	28.5
		25	2.06	7.58	1.72	1.50	2.00	26.0
		35	1.98	7.42	1.70	1.50	1.92	24.8
		45	1.92	7.30	1.66	1.50	1.84	24.0
Human	2	20 Delay	1.94	7.34	1.66	1.50	1.86	24.3
		b-value	0.30	0.49	0.44	0.47	0.38	
	1	Delay	2.12	7.72	1.74	1.50	2.06	27.0
		b-value	1.10	1.73	1.54	1.63	1.34	

To keep the total duration the same, the length of delays varied for each VS module.

gradients was set constant at 0.5 ms, and the duration of the gradient flat tops was adjusted to maintain the desired V_c .The length of delays and the total duration of each VS module are listed in Table 1. Other imaging parameters were the same as in the previous experiments.

The signal difference between the tag and control images was averaged across repetitions, then normalized to the averaged control images and expressed as ratio maps. After normalization, T_2 decay during the tagging process and the receive-B_1 inhomogeneity was automatically removed; thus, the results can be directly compared. Regions of interest (ROIs) were generated from the control images to exclude the noisy pixels outside the phantom. The absolute values of the ratios were averaged across the ROIs to give the average error levels and then were averaged across G_{max} to give overall estimates of the error levels in different gradient directions. The standard deviations (STDs) were calculated across different G_{max}.

In Vivo Experiments

Five young, healthy volunteers (3M, 2F, age 31.0 ± 5.4 y/o) were scanned on scanner A under an institutional review board-approved protocol. VS gradients were applied in each of L/R, A/P and S/I directions for both VS preparation modules and with an image acquisition using a G_{max} of 20 mT/m and a ramp time of 0.5 ms. The delays and total duration are listed in Table 1. The order of scans was randomized. Experiments with $V_c = 2$ cm/s and 1 cm/s were done in two sessions separated by several hours. Other parameters included: five 8 mm-thick slices with 8-mm gaps, FOV = 220 × 220 mm, spatial-spectral excitation, spin echo, TR = 4 s, TE = 17.9 ms ($V_c = 2$ cm/s) and 19.6 ms ($V_c = 1$ cm/s), PLD = 1.5 s, two global background suppression (BGS) pulses (22) played at 1,480 ms and 420 ms prior to image acquisition, global saturation pulses applied at the end of imaging acquisition to reset the magnetization (14), 18 pairs of tag, and control following two dummy repetitions.

As a reference, cerebral blood flow (CBF) maps using pulsed ASL (PICORE QUIPSS II (5,23)) were also collected throughout each VSASL session (one PICORE scan per VS gradient direction). The tagging parameters were: hyperbolic secant inversion pulse, inversion slab thickness = 200 mm, 10-mm gap between tagging and imaging slabs, $TI/TI_1 = 2.4$ s/0.8 s and BGS pulses played at 1,580 ms, and 500 ms prior to image acquisition, TR/TE matched to corresponding VSASL scans. The TIs used here were chosen to emphasize minimizing transit delay effects and achieving an accurate quantification of CBF. The resulting low SNR was compensated by spatial smoothing (see below). Pulsed ASL (PICORE) was chosen as the reference ASL preparation because the labeling efficiency is very consistent, and we were interested in accurate measurement of absolute CBF. Although Pseudo-Continuous ASL (PCASL) (6) has higher SNR, the uncertainty in the tagging efficiency can compromise the accuracy of the measurement (24).

For CBF quantification, four reference images were collected to estimate the receive-coil sensitivity map and the conversion factor between MR signal and the amount of arterial blood from fully relaxed cerebrospinal fluid (CSF) signal. Double inversion recovery (DIR) images (TIs = 3580/400 ms) were collected to generate gray matter (GM) masks.

The ASL signal was calculated and then averaged across repetitions. The signal attenuation from BGS was corrected with an inversion efficiency of 0.97 for each inversion pulse used. The b-values of the VS preparations were non-zero (Table 1) in the tag condition, and zero in the control condition. To avoid CBF overestimation from diffusion attenuation, the amount of attenuation difference, $Me(-b * D_{GM})$, was estimated and removed, where $\boldsymbol{M}$ is the magnetization of GM at the time of tagging with T_1 relaxation corrected, $\mathbf{b}$ is the b-value of the corresponding VS module, and $\boldsymbol{D}_{GM}$ is the diffusion coefficient of GM [6.3×10^{-4} mm^2/s (25)]. The GM CBF values were then calculated using a modified dynamic ASL model (8). The acquisition time for each slice was accounted in the calculation of the actual TI for each individual slice. Note that for VSASL, the effective *TE*s of the VS tagging modules were estimated from Bloch simulation to correct for the T_2 relaxation during VS tagging (the effect of the T_1 relaxation was negligible according to the simulation).

The CBF maps were masked by GM ROIs, and the averaged GM CBF values were calculated for each subject at different V_c. The temporal STDs (tSTDs) in the GM ROIs were also calculated to estimate the effects of the ASL preparations on the stability of the ASL signal.

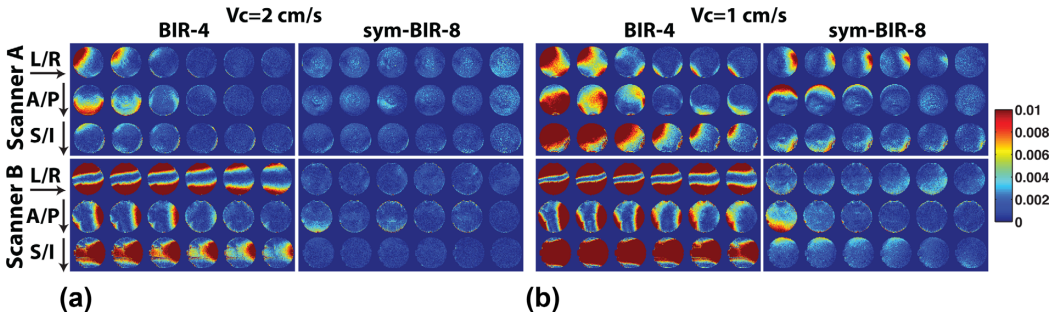

FIG. 3. Control-tag subtraction error from EC effects with various delays inserted after gradient pulses in BIR–4 and sym-BIR-8 modules on scanners A and B, normalized to the signal intensity under the control condition. Panel **(a)** was collected with $V_c = 2$ cm/s; panel **(b)** was collected with $V_c = 1$ cm/s. The five columns in each subplot were collected with corresponding delays listed in the Methods section. [Color figure can be viewed in the online issue, which is available at wileyonlinelibrary.com.]

To demonstrate the spatial distribution of the EC effects, which were assumed to be slowly varying in space and independent of local perfusion, the masked CBF maps were spatially smoothed by a large boxcar kernel (17 × 17 pixels) to remove the local spatial variation due to tissue difference, small motion, misalignment, etc. The smoothed GM CBF maps from VSASL were divided by that from PICORE to generate ratio maps and then masked by a common brain ROI. Any partial volume effects generated by this large smoothing kernel were cancelled in the division because the smoothing was applied on both the data acquired with VSASL and that with PICORE. The CBF maps from PICORE were used as the reference because: 1) there should be no EC effects; and 2) average GM CBF should be constant at different slice locations. However, averaged GM CBF from PICORE showed a decreasing trend as the slice location moved higher (data not shown), likely due to underestimation of CBF from the transit delay effects (see Discussion for rationale). To compensate for the underestimation, the PICORE CBF maps in different slices were scaled so that the averaged GM CBF in each slice was the same as that in the lowest slice. The scaling was not applied in the calculation of averaged PICORE GM CBF values reported. Note that this compensation was not applied in the VSASL data analysis because it would affect the spatial distribution of the EC effects in S/I (slice) direction.

RESULTS

The simulation results are shown in Figure 2 (a)–(d) without delays; (e)–(f) with delays). The BIR-4, asym-BIR-8, and sym-BIR-8 were insensitive to B_1 variations once their adiabatic conditions were satisfied (Fig. 2b); that is, the profiles of M_z with respect to velocity were the same for $B_1 = 14 - 26$ μT. On the other hand, DRHS was sensitive to B_1 variations due to the B_1-sensitive hard 90° RF pulses, resulting in compromised tagging efficiency when the B_1 deviated from the nominal B_1. Note that in VSASL using saturation preparation, the saturation of the spins moving above V_c in the tag condition is realized by integrating the longitudinal magnetization of spins at different velocities (14). For the off-resonance (B_0) sensitivity (Fig. 2c), DRHS showed the lowest sensitivity to a wide range of resonance offset once the delay between the HS pulses was correctly adjusted; while BIR-4, asym-BIR-8, and sym-BIR-8 showed a similar but slightly higher sensitivity to off-resonance effects.

The EC sensitivity of the VS modules without delays is shown in Figure 2d. BIR-4 module showed the highest sensitivity to ECs, especially to those of relatively long time constants, likely due to the non-EC–compensating gradient layout. DRHS and asym-BIR-8 showed reduced EC sensitivity, with the asym-BIR-8 performing the better of the two. Sym-BIR-8 showed the lowest EC sensitivity across a wide range of time constants among these modules. Note that a smaller G_{max} or a shorter plateau duration of the gradient pulse were required to provide the same V_c in DRHS and sym-BIR-8 due to larger separation between the gradient pulses (Figs. 2a and 2e), potentially reducing EC effects. With delays inserted, the EC sensitivity was significantly reduced in all the modules (Fig. 2f), especially the sensitivity to ECs of short time constants (10^{-4}–10^{-3} s). Sym-BIR-8 showed the highest robustness against EC effects among these modules.

The results of the phantom experiments with various delays are shown in Figure 3. Significant improvement of EC reduction with delays inserted was observed in BIR-4 as the length of the delay increased: The normalized average subtraction errors (averaged across gradient directions and scanners) reduced from $0.76 \pm 0.62\%$ (mean ± SEM, standard error of the mean) to $0.17 \pm 0.14\%$ at $V_c = 2$ cm/s ($P = 0.03$) and from $2.42 \pm 1.98\%$ to $0.48 \pm 0.41\%$ at $V_c = 1$ cm/s ($P = 0.03$), where inserting delays was the only mechanism to reduce EC effects. On the other hand, not much further improvement was observed in sym-BIR-8 at $V_c = 2$ cm/s (from $0.13 \pm 0.04\%$ to $0.12 \pm 0.07\%$; $P = 0.83$), where the EC reduction was already sufficient with very short delays; however, at $V_c = 1$ cm/s, lengthening the delays continued improving its performance (from $0.30 \pm 0.12\%$ to $0.12 \pm 0.02\%$; $P = 0.02$).

The results of the phantom experiments with combinations of testing conditions are shown in Figure 4 and Figure 5, with the results in Figure 4 summarized in Figure 5. The normalized subtraction errors (mean ± STD, a.u.) across G_{max}, gradient directions, V_c and scanners

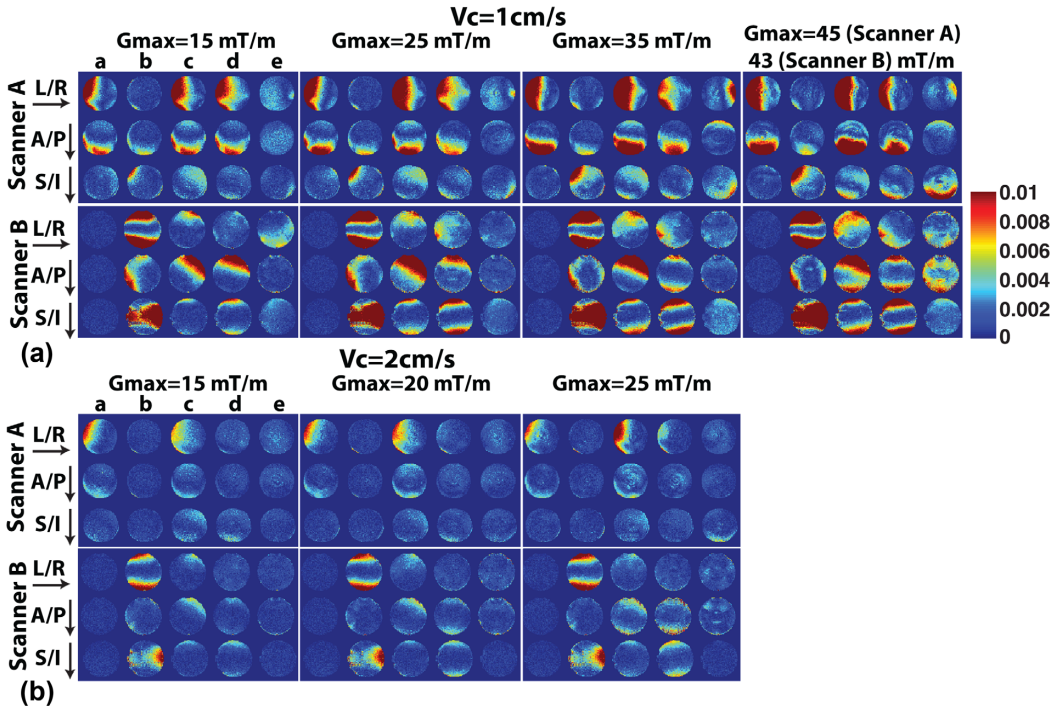

FIG. 4. Control-tag subtraction error from EC effects under various testing conditions from scanner A and B, normalized to the signal intensity collected under the control condition. Panel **(a)** was collected with cutoff velocity ($V_{c)}=2$ cm/s; panel **(b)** was collected with $V_c=1$ cm/s. Each subbrick shows the results with G_{max} set to the value on the top. The five columns in each subplot were collected with DRHS (a), BIR–4 (b), asym-BIR-8 M. 1 (c), asym-BIR-8 M. 2 (d), and sym-BIR-8 (e) VS preparations. The three rows in each plot were collected with the VS gradient pulses applied in L/R (axial slice), A/P (axial slice), and S/I (sagittal slice) directions, with arrows indicating the directions. [Color figure can be viewed in the online issue, which is available at wileyonlinelibrary.com.]

were 0.0018 ± 0.0023, 0.0040 ± 0.0046, 0.0036 ± 0.0029, 0.0025 ± 0.0015 and 0.0016 ± 0.0009 for DRHS, BIR-4, asym-BIR-8 M.1, asym-BIR-8 M.2 and sym-BIR-8 accordingly. Pair-wise *t*-tests were performed and the *P*-values were tabulated in Table 2. Note that the significance detection level was set at 0.005 for these multiple comparisons, with Bonferroni correction applied. On both scanners and on all the three principal axes, the subtraction errors increased as G_{max} increased. At the same G_{max}, higher subtraction error was observed at lower V_c. This may be due to a less efficient cancellation of the ECs generated from the rising and decaying portions of the gradient pulses as their separation increased at lower V_c. DRHS, BIR-4, and asym-BIR-8 M. 1 performed better on one scanner than the other, which may be due to the different EC spectra (EC amplitude and time constants) of the two scanners. Asym-BIR-8 M.2 performed better than asym-BIR-8 M. 1 ($P=9.8 \times 10^{-4}$) and better than BIR-4 but not significantly so ($P=0.032$) on both scanners. Overall, sym-BIR-8 showed significantly lower subtraction error level than BIR-4 ($P=1.1 \times 10^{-3}$), asym-BIR-8 M.1 ($P=9.8 \times 10^{-6}$), and asym-BIR-8 M.2 ($P=9.5 \times 10^{-5}$). Although sym-BIR-8 had an error level comparable ($P=0.54$) to that of DRHS, sym-BIR-8 was more robust—with a much lower STD in the subtraction errors than DRHS (0.0009 vs. 0.0023). Therefore, sym-BIR-8

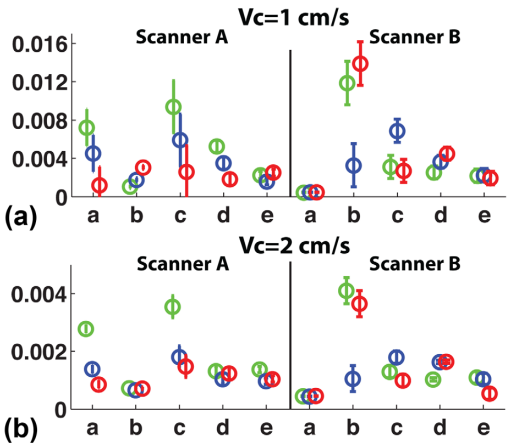

FIG. 5. The means and standard deviations of the averaged subtraction error across different maximum VS gradient amplitude from Fig. 4, where the green, blue, and red error bars represent the results from L/R, A/P, and S/I directions collected with DRHS (a), BIR–4 (b), asym-BIR-8 M. 1 (c), asym-BIR-8 M. 2 (d), and sym-BIR-8 (e) VS preparations, respectively. [Color figure can be viewed in the online issue, which is available at wileyonlinelibrary.com.]

Table 2
The *P*-Values of the Pair-Wise *t*-Tests on Normalized Average Residual Errors in the Phantom Experiments (Averaged Across G_{max}, Gradient Directions, V_c, and Scanners) and the *P*-Values of the Pair-Wise *t*-Tests on Averaged GM CBF Values (Averaged Across VS Gradient Directions, Subjects, and V_c)

		DRHS	BIR-4	Asym-BIR-8 M. 1	Asym-BIR-8 M. 2	Sym-BIR-8
Phantom	DRHS		0.019	7.5×10^{-8} *	0.026	0.54
	BIR-4			0.69	0.032	1.1×10^{-3} *
	Asym-BIR-8 M. 1				9.8×10^{-4} *	9.8×10^{-6} *
	Asym-BIR-8 M. 2					9.5×10^{-5} *
Human	PICORE	0.38	1.5×10^{-3} *	5.3×10^{-4} *	3.5×10^{-4} *	0.018
	DRHS		3.6×10^{-5} *	1.8×10^{-4} *	5.5×10^{-4} *	0.28
	BIR-4			1.3×10^{-6} *	3.6×10^{-7} *	7.4×10^{-6} *
	Asym-BIR-8 M. 1				0.041	4.0×10^{-4} *
	Asym-BIR-8 M. 2					1.5×10^{-3} *

The *P*-values reached significance are labeled by * ($P < 0.005$ for the phantom results and $P < 0.0033$ for the human results; with Bonferroni correction applied).

was the most robust among the tested VS modules overall (Fig. 5).

Examples of quantitative CBF maps (with the VS gradients applied in L/R direction) are shown in Figure 6. Compared with PICORE, some asymmetric regional CBF overestimations were observed along the L/R direction with the DRHS, asym-BIR-8 M.1, and asym-BIR-8 M.2 preparations, but not with the BIR-4 and sym-BIR-8 preparations. However, a globally CBF underestimation can be observed with the BIR-4 preparation.

The averaged CBF ratio maps are shown in Figure 7. The CBF overestimation due to EC effects showed a low-spatial-frequency dependence. For example, in L/R direction, an asymmetry can be observed in DRHS, asym-BIR-8 M. 1, and asym-BIR-8 M. 2; the BIR-4 preparation showed less asymmetry; whereas the sym-BIR-8 module showed the least. Similar patterns were seen in A/P and S/I directions. The EC effects and their spatial distribution were more noticeable at lower V_c. There was also a noticeable global CBF underestimation with BIR-4 (see Discussion section). Overall, sym-BIR-8 (Fig. 7, col. e) showed the least spatial asymmetry, and was the most robust in cancelling ECs among these VS modules. A similarity of the spatial distribution patterns of EC effects was observed between the in vivo (Fig. 7) and the phantom (Fig. 4) results. Note that the image orientation with the VS gradients applied in S/I direction was different between Figure 4 and Figure 7 (only axial images were collected in vivo); thus, the EC spatial distribution appears different in these images. Note that the scales in Figures 4 and 7 are different. Absolute subtraction errors are shown in Figure 4; and CBF differences are shown in Figure 7.

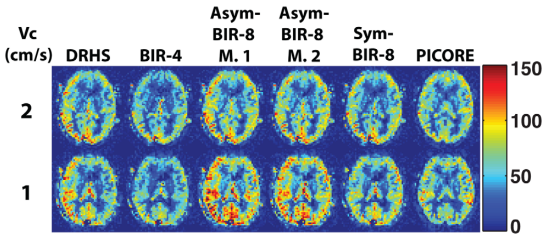

FIG. 6. The CBF maps of slice 2 in subject 1 measured by VSASL at $V_c = 2$ cm/s (top row) and 1 cm/s (bottom row) with VS gradient pulses applied in L/R direction and corresponding PICORE scans in the same sessions (unit ml/min/100 g). [Color figure can be viewed in the online issue, which is available at wileyonlinelibrary.com.]

For the CBF quantification, the averaged (across gradient directions, V_c and subjects) GM CBF values (mean ± SEM) were 65.1 ± 3.4, 57.9 ± 3.3, 73.7 ± 4.3, 71.7 ± 4.2, 66.9 ± 4.0, and 63.7 ± 4.1 ml/min/100 g with DRHS, BIR-4, asym-BIR-8 M.1, asym-BIR-8 M.2, sym-BIR-8 and PICORE, respectively. They were all in the expected physiological range, and more detailed GM CBF values are tabulated in Table 3. A one-way repeated measures ANOVA was performed on the GM CBF values averaged across gradient directions and V_c, and a significant dependence of the CBF on the preparations used was found ($P = 2.6 \times 10^{-9}$). Post hoc pair-wise *t*-tests were performed on the preparations, and the results and corresponding *P*-values are tabulated in Table 2, with Bonferroni correction applied. Asym-BIR-8 M. 1 and asym-BIR-8 M. 2 gave significantly higher GM CBF estimates than PICORE ($P = 4.0 \times 10^{-4}$ and $P = 1.5 \times 10^{-3}$, accordingly); and DRHS and sym-BIR-8 gave comparable (slightly higher) GM CBF estimates to PICORE ($P = 0.38$ and $P = 0.018$, accordingly), whereas BIR-4 gave significantly lower GM CBF estimates than DRHS ($P = 1.5 \times 10^{-3}$). Asym-BIR-8 M. 1 and M. 2 measured the highest CBF values at both $V_c = 1$ cm/s and 2 cm/s, likely due to strong EC effects. Both DRHS and sym-BIR-8 had closer CBF estimates to that of PICORE. However, in some regions, the CBF was underestimated with DRHS preparation with a gradient-direction–dependent pattern (Figs. 6 and 7). This is likely because the tagging efficiency of DRHS was compromised due to its B_1 sensitivity. This might have compensated some of the CBF overestimation from EC effects, resulting in plausible average CBF values but an inaccurate spatial distribution. Though sym-BIR-8 could still have overestimated GM CBF due to any residual EC effects and/or diffusion attenuation, it should be the least biased and the most robust among these VS preparations.

Pair-wise *t*-tests were also performed on V_c for each preparation. Although average GM CBF values were measured higher at $V_c = 1$ cm/s than at $V_c = 2$ cm/s with

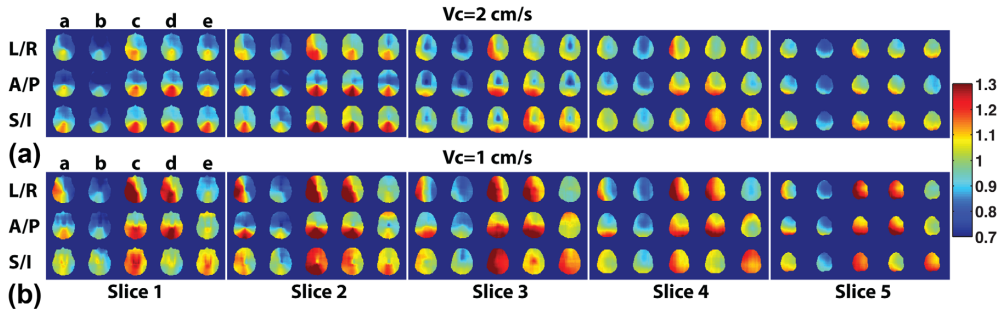

FIG. 7. The subject-averaged ratio maps of CBF measured by VSASL at $V_c = 2$ cm/s **(a)** and 1 cm/s **(b)** and corresponding PICORE scans in the same sessions. The five subplots show the ratio maps in the five slices collected. The five columns in each subplot were collected with DRHS (a), BIR–4 (b), asym-BIR-8 M. 1 (c), asym-BIR-8 M. 2 (d), and sym-BIR-8 (e) VS preparations, respectively. The three rows in each plot were collected with the VS gradient pulses applied in L/R, A/P and S/I directions. [Color figure can be viewed in the online issue, which is available at wileyonlinelibrary.com.]

the VS preparations, the differences were not significant ($P = 0.44$, 0.68, 0.093, 0.30, and 0.59 for DRHS, BIR-4, asym-BIR-8 M.1, asym-BIR-8 M.2, sym-BIR-8, and PICORE, respectively).

The averaged tSTDs (mean ± STD, a.u.) were 13.5 ± 2.6, 13.2 ± 2.5, 13.7 ± 2.6, 13.6 ± 2.4, 13.7 ± 2.8 and 13.7 ± 2.7 for DRHS, BIR-4, asym-BIR-8 M.1, asym-BIR-8 M.2, sym-BIR-8, and PICORE, respectively. There was no significant difference between any pair of the preparations.

DISCUSSION

By both simulation and experiment, the sym-BIR-8 design appears to achieve the best performance of the velocity-selective modules tested. This may be at least partially explained by the cancellation of EC effects in the symmetrical design, as discussed previously in this paper in the Theory Section. The symmetric gradient layout may also be useful for other applications that require EC effects to be minimized after the preparation, such as diffusion-weighted imaging and flow-prepared angiography.

In simulation, DRHS showed a lower sensitivity to off-resonance effects in the inversion bands than other VS preparation modules (Fig. 2). This is probably because the adiabatic full passage in DRHS can induce inversion with $M_z \leq -0.95$ within a bandwidth of ± 1115 Hz, compared to a narrower bandwidth of ± 805 Hz in other BIR-based modules, according to the Bloch simulation.

In the phantom experiments with BIR-4, strong EC effects across the L/R and A/P axes were observed on scanner B [also noticed in (15)] but not on scanner A (Fig. 3 and Fig. 4) due to their different EC spectra. The fact that the EC effects from cross terms were significantly reduced in other VS modules suggested that these cross terms had relatively long time constants and can be effectively suppressed by the proposed pulse layout.

For the in vivo PICORE results, the trend of CBF decreasing as the slice location moved higher was not expected because a conservative PLD (1.6 s) was used on these young and healthy subjects. This unexpected trend is likely due to the transit delay effect: The distance between the bottom and the top slices was relatively large (56 mm) with the circle of Willis in between, and the top slice was acquired only about 200 ms later than the bottom slice. The transit delay effect should be more profound in distal regions because the gap is larger. In addition, as arterial blood flows to more distal slices, it

Table 3
Mean GM CBF (Mean ± SEM, Unit ml/min/100 g) in Each Subject

Subject	V_c (cm/s)	DRHS	BIR-4	Asym-BIR-8 Mod. 1	Asym-BIR-8 Mod. 2	Sym-BIR-8	PICORE
1	2	70.6 ± 1.8	60.7 ± 1.8	73.4 ± 2.0	74.1 ± 1.8	68.1 ± 2.2	69.0 ± 1.3
	1	73.0 ± 2.8	59.5 ± 1.7	79.5 ± 5.2	75.8 ± 4.6	66.6 ± 3.4	62.6 ± 5.3
2	2	82.5 ± 3.3	76.4 ± 1.1	93.6 ± 3.6	94.6 ± 4.1	88.0 ± 3.3	87.6 ± 2.2
	1	73.4 ± 1.1	67.5 ± 2.5	88.4 ± 3.9	86.0 ± 6.4	81.2 ± 4.7	74.1 ± 1.6
3	2	64.3 ± 0.5	59.1 ± 0.9	72.6 ± 2.8	68.6 ± 3.2	71.9 ± 4.6	64.9 ± 0.7
	1	69.6 ± 2.2	65.6 ± 2.4	84.5 ± 1.8	81.3 ± 0.8	74.6 ± 4.4	70.6 ± 2.2
4	2	56.4 ± 1.1	48.5 ± 4.5	59.8 ± 1.8	59.1 ± 1.0	56.7 ± 1.8	59.2 ± 1.2
	1	60.5 ± 1.2	50.9 ± 2.3	70.9 ± 1.8	65.4 ± 1.6	61.2 ± 5.2	58.1 ± 2.5
5	2	44.8 ± 1.0	41.3 ± 0.9	48.9 ± 1.6	51.0 ± 2.2	46.0 ± 1.6	44.0 ± 0.7
	1	56.3 ± 2.1	49.4 ± 2.2	65.3 ± 2.0	61.5 ± 1.9	54.4 ± 1.7	46.9 ± 0.6
Average	2	63.7 ± 6.4	57.2 ± 6.0	69.7 ± 7.5	69.5 ± 7.4	66.1 ± 7.1	64.9 ± 7.1
	1	66.6 ± 3.5	58.6 ± 3.7	77.7 ± 4.3	74.0 ± 4.6	67.6 ± 4.8	62.5 ± 4.8
	2 & 1	65.1 ± 3.4	57.9 ± 3.3	73.7 ± 4.3	71.7 ± 4.2	66.9 ± 4.0	63.7 ± 4.1

For VS preparation, averaged over scans with VS gradients applied on three principal axes. For PICORE, averaged over scans within the same session. Averaged GM CBF values (mean ± SEM, unit ml/min/100 g) reported were calculated across subjects for $V_c = 2$ cm/s and 1 cm/s, accordingly, and across both subjects and $V_c = 2$ and 1 cm/s.

is generally moving slower and the vascular structure it travels through is likely to be more complicated, further increasing the magnitude and heterogeneity of the transit delays. If it is assumed that GM CBF should be relatively constant across the whole brain, then the trend of decreasing calculated CBF indicated that the averaged GM CBF values from PICORE were underestimated due to the transit delay effect in higher slices.

An interesting observation was that all the VS modules, regardless of the directions in which the VS gradient pulses were applied, measured higher CBF values in the posterior (occipital) regions of the brain (higher ratios in the bottom two slices in Fig. 7) than PICORE. This is likely because the transit delays in occipital regions are longer (about 0.52 s) than those in inferior frontal regions (26). PICORE with an insufficient PLD would result in CBF underestimation in occipital regions; in contrast, VSASL should be intrinsically transit delay insensitive, thus having less biased CBF estimates in these regions. A recent study on Moyamoya patients (27) also confirmed that VSASL is less sensitive to long transit delays.

BIR-4 preparation underestimated CBF globally in each subject (Fig. 6, Fig. 7; Table 3). This underestimation is likely due to additional T_2 relaxation during VS preparation (T_2 relaxation during image acquisition was canceled out in the CBF calibration process). In VS preparation, the tip-down RF pulse (the first hard pulse in DRHS or the first BIR subpulse in BIR-4 and BIR-8) leaves the spins in the transvers plane for applying VS encoding. The T_2 relaxation while the spins are in the transvers plane is not negligible and was accounted for in CBF quantification using an effective TE of the VS preparations calculated through Bloch simulation. However, according to the Luz-Meiboom model (28–30), spins undergoing exchange and/or bounded diffusion move through gradient fields in and around red blood cells; thus, the apparent T_2 of the arterial blood decreases as the repetition rate of refocusing pulses (the echo spacing) increases. In the BIR-4 module, the long spacing (> 9 ms) between the RF subpulses might have caused a faster T_2 decay due to this T_2-shortening effect. This additional T_2 decay was not taken into account in the CBF quantification and may have resulted in the CBF underestimation with BIR-4 preparation.

CBF values measured with VSASL at $V_c = 1$ cm/s were higher (although not significantly) compared to that at $V_c = 2$ cm/s (Table 3). This may be due to larger EC effects, larger diffusion effects, and higher motion sensitivity at lower V_c. However, for most applications, low V_c is desirable because it localizes the ASL signal closer to the tissue, and the balance between localization and potential artifacts is a fundamental tradeoff in the application of VSASL.

There were several limitations of this study. First, the PICORE QUIPSS II was chosen as the reference; however, its own transit delay sensitivity might affect the accuracy of the comparison of VS modules. Second, the diffusion attenuation correction was not perfect; thus, any residual artifact could confound the spatial distribution of EC effects as well as CBF quantification. Third, the in vivo measurements were done without strict control over subjects' physiological status such as awareness, attention, and whether the subject's eyes were open or closed. Although the scan order was randomized to reduce the interscan variations, any residual fluctuation could affect the comparison of the VS preparations across scans. Finally, due to logistical limitations in this study, we did not collect in vivo data from scanner B, which may have improved our understanding of the connection between the EC reduction effectiveness in the phantom and that in vivo.

CONCLUSION

We have shown through theoretical analysis, simulation, and phantom and in vivo experiments that the sym-BIR-8 VS module is the optimal and most robust against EC effects among the VS preparations tested. Based on demonstrated EC, B_1, and B_0 insensitivity, the sym-BIR-8 module should benefit studies using VS preparation with improved accuracy and reliability.

REFERENCES

1. Kwong KK, Belliveau JW, Chesler DA, et al. Dynamic magnetic resonance imaging of human brain activity during primary sensory stimulation. Proc Natl Acad Sci USA 1992;89:5675–5679.
2. Williams DS, Detre JA, Leigh JS, Koretsky AP. Magnetic resonance imaging of perfusion using spin inversion of arterial water. Proc Natl Acad Sci USA 1992;89:212–216.
3. Edelman RR, Siewert B, Darby DG, et al. Qualitative mapping of cerebral blood flow and functional localization with echo-planar MR imaging and signal targeting with alternating radio frequency (STAR) sequences: applications to MR angiography. Radiology 1994;192:513–520.
4. Kim SG. Quantification of relative cerebral blood flow change by flow-sensitive alternating inversion recovery (FAIR) technique: application to functional mapping. Magn Reson Med 1995;34:293–301.
5. Wong EC, Buxton RB, Frank LR. Implementation of quantitative perfusion imaging techniques for functional brain mapping using pulsed arterial spin labeling. NMR Biomed 1997;10:237–249.
6. Dai WY, Garcia D, de Bazelaire C, Alsop DC. Continuous flow-driven inversion for arterial spin labeling using pulsed radio frequency and gradient fields. Magn Reson Med 2008;60:1488–1497.
7. Alsop DC, Detre JA. Reduced transit-time sensitivity in noninvasive magnetic resonance imaging of human cerebral blood flow. J Cereb Blood Flow Metab 1996;16:1236–1249.
8. Buxton RB, Frank LR, Wong EC, Siewert B, Warach S, Edelman RR. A general kinetic model for quantitative perfusion imaging with arterial spin labeling. Magn Reson Med 1998;40:383–396.
9. Petersen ET, Lim T, Golay X. Model-free arterial spin labeling quantification approach for perfusion MRI. Magn Reson Med 2006;55:219–232.
10. Wu WC, Wang J, Detre JA, Ratcliffe SJ, Floyd TF. Transit delay and flow quantification in muscle with continuous arterial spin labeling perfusion-MRI. J Magn Reson Imaging 2008;28:445–452.
11. van Osch MJP, Teeuwisse WM, van Walderveen MAA, Hendrikse J, Kies DA, van Buchem MA. Can arterial spin labeling detect white matter perfusion signal? Magn Reson Med 2009;62:165–173.
12. Bokkers RPH, Bremmer JP, van Berckel BNM, et al. Arterial spin labeling perfusion MRI at multiple delay times: a correlative study with (H2O)-O-15 positron emission tomography in patients with symptomatic carotid artery occlusion. J Cereb Blood Flow Metab 2010;30:222–229.
13. Yun TJ, Sohn CH, Han MH, et al. Effect of delayed transit time on arterial spin labeling: correlation with dynamic susceptibility contrast perfusion magnetic resonance in moyamoya disease. Invest Radiol 2013;48:795–802.
14. Wong EC, Cronin M, Wu W-C, Inglis B, Frank LR, Liu TT. Velocity-selective arterial spin labeling. Magn Reson Med 2006;55:1334–1341.
15. Meakin JA, Jezzard P. An optimized velocity selective arterial spin labeling module with reduced eddy current sensitivity for improved perfusion quantification. Magn Reson Med 2013;69:832–838.

16. Reese TG, Heid O, Weisskoff RM, Wedeen VJ. Reduction of eddy-current-induced distortion in diffusion MRI using a twice-refocused spin echo. Magn Reson Med 2003;49:177–182.
17. Alexander AL, Tsuruda JS, Parker DL. Elimination of eddy current artifacts in diffusion-weighted echo-planar images: the use of bipolar gradients. Magn Reson Med 1997;38:1016–1021.
18. Wong EC, Guo J. BIR-4 based B1 and B0 insensitive velocity selective pulse trains. In Proceedings of the 18th Annual Meeting of ISMRM; Stockholm, Sweden. 2010. p. 2853.
19. Nezafat R, Ouwerkerk R, Derbyshire AJ, Stuber M, McVeigh ER. Spectrally selective B1-insensitive T2 magnetization preparation sequence. Magn Reson Med 2009;61:1326–1335.
20. Garwood M. The return of the frequency sweep: designing adiabatic pulses for contemporary NMR. J Magn Reson 2001;153:155–177.
21. Huang J, Zhu DC. Simultaneous magnetic resonance imaging of diffusion anisotropy and diffusion gradient. Magn Reson Imaging 2008;26: 337–346.
22. Ye FQ, Frank JA, Weinberger DR, McLaughlin AC. Noise reduction in 3D perfusion imaging by attenuating the static signal in arterial spin tagging (ASSIST). Magn Reson Med 2000;44:92–100.
23. Wong EC, Buxton RB, Frank LR. Quantitative imaging of perfusion using a single subtraction (QUIPSS and QUIPSS II). Magn Reson Med 1998;39:702–708.
24. Aslan S, Xu F, Wang PL, Uh J, Yezhuvath US, van Osch M, Lu H. Estimation of labeling efficiency in pseudocontinuous arterial spin labeling. Magn Reson Med 2010;63:765–771.
25. Kuroiwa T, Nagaoka T, Ueki M, Yamada I, Miyasaka N, Akimoto H. Different apparent diffusion coefficient: water content correlations of gray and white matter during early ischemia. Stroke 1998;29:859–865.
26. Dai WY, Robson PM, Shankaranarayanan A, Alsop DC. Reduced resolution transit delay prescan for quantitative continuous arterial spin labeling perfusion imaging. Magn Reson Med 2012;67:1252–1265.
27. Qiu DQ, Straka M, Zun ZH, Bammer R, Moseley ME, Zaharchuk G. CBF measurements using multidelay pseudocontinuous and velocity-selective arterial spin labeling in patients with long arterial transit delays: Comparison with xenon CT CBF. J Magn Reson Imaging 2012; 36:110–119.
28. Luz Z, Meiboom S. Nuclear magnetic resonance study of protolysis of trimethylammonium ion in aqueous solution - order of reaction with respect to solvent. J Chem Phys 1963;39:366–370.
29. Wright GA, Hu BS, Macovski A. Estimating oxygen saturation of blood in vivo with MR imaging at 1.5T. J Magn Reson Im 1991;1: 275–283.
30. Lu HZ, Xu F, Grgac K, Liu PY, Qin Q, van Zijl P. Calibration and validation of TRUST MRI for the estimation of cerebral blood oxygenation. Magn Reson Med 2012;67:42–49.

Acknowledgements

Chapter 1, in full, is a reprint of the material as it appears in Magnetic Resonance in Medicine 2014. Guo J, Meakin JA, Jezzard P, Wong EC. An optimized design to reduce eddy current sensitivity in velocity-selective arterial spin labeling using symmetric BIR-8 pulses. Magn Reson Med 2014. doi: 10.1002/mrm.25227. The dissertation author was the primary investigator and author of this paper.

CHAPTER 2 : Increased SNR Efficiency in Velocity Selective Arterial Spin Labeling using Multiple Velocity Selective Saturation Modules (mm-VSASL)

Abstract

Purpose: Velocity-selective arterial spin labeling (VSASL) is theoretically insensitive to transit delay (TD) effects. However, it uses saturation instead of inversion, resulting in compromised signal to noise ratio (SNR). In this study we explore the use of multiple velocity-selective saturation (VSS) modules in VSASL (mm-VSASL) to improve SNR.

Methods: Theoretical SNR efficiency improvement and optimized parameters were calculated from simulations for mm-VSASL. VSASL with two VSS modules (VSASL-2VSS) was implemented to measure cerebral blood flow *in vivo*, compared with conventional VSASL (VSASL-1VSS), Pulsed ASL and Pseudo-Continuous ASL. TDs and bolus durations (BDs) were measured to validate the simulations and to examine the TD sensitivity of these preparations.

Results: Compared with VSASL-1VSS, VSASL-2VSS achieved a significant improvement of SNR (22.1 ± 1.9%, P = 1.7 × 10-6) *in vivo*, consistent with a 22.7% improvement predicted from simulations. The SNR was comparable to or higher (in GM, P = 4.3 × 10-3) than that using PCASL. VSASL was experimentally verified to have minimal TD effects.

Conclusion: Utilizing multiple VSS modules can improve the SNR efficiency of VSASL. Mm-VSASL may result in an SNR that is comparable to or even higher than that of PCASL in applications where long PLDs are required.

Introduction

In arterial spin labeling (ASL), magnetically labeled water in arterial blood is employed as an endogenous contrast agent to measure local tissue perfusion. In conventional ASL (1-6), it is required to have a spatial gap between the labeling and imaging regions to avoid any undesired perturbation of the tissue magnetization. This gap results in a transit delay (TD) for the labeled blood to reach the destination tissue and a necessary wait time before perfusion-weighted images can be acquired. Due to the complex vasculature and the distribution of arterial blood velocities, the TDs are heterogeneous and are the main source of error in local cerebral blood flow (CBF) quantification (7-9), especially in cases where slow or collateral flow conditions exist (10-13). To tackle these problems, Velocity-Selective ASL (VSASL) (14-16) globally labels spins on the basis of flow velocity, eliminating the gap as well as the associated heterogeneous TDs in conventional ASL.

Eliminating the heterogeneous TDs in ASL guarantees that a single optimal post-labeling delay (PLD) is always available to measure perfusion with both accuracy and maximized SNR efficiency (see Methods). This is because: 1) the condition of PLD ≥ TD can be always satisfied, so potential inaccuracy of perfusion quantification due to violation of this condition can be avoided; and 2) TD no longer limits the choice of PLD, so an optimal PLD can be used to maximize the ASL signal, considering both the amount of labeled blood delivered and the signal loss due to longitudinal relaxation. However, due to the saturation-based labeling in VSASL, the labeling efficiency is compromised, resulting in compromised signal to noise ratio (SNR) compared to inversion based labeling methods such as Pseudo-Continuous ASL (PCASL) (6). In this study, we introduce a novel strategy of utilizing multiple Velocity-Selective Saturation (VSS) modules in VSASL (mm-VSASL) to improve SNR efficiency.

Theory

VSASL acquires images under two preparation conditions: label and control. Under the label condition, the arterial blood is labeled by VSS modules consisted of radio frequency (RF) pulses and flow-weighting gradients, and the spins moving above a chosen cutoff velocity (Vc) are saturated. Under the control condition, the VSS modules are applied without the flow-weighting gradients, leaving the spins unperturbed. The difference between the two conditions is a bolus of labeled spins that is moving above the Vc at the time of labeling. After a delay, perfusion-weighted images are acquired with flow-weighting gradients of the same Vc, generating a VSASL signal that consists of blood that has decelerated through Vc. Note that it is essential to match the Vc in the image acquisition and that in the preparation, so that the VSASL signal is directly proportional to the PLD, or equivalently, so that the TD is effectively eliminated (16).

In conventional VSASL (Figs. 1a and 1c), at the time of imaging, the ASL signal is given by (following (16)):

$$S_{1VSS} = e^{-eTE/T_{2a}} \cdot CBF \cdot M_0 \cdot (1 - e^{-\frac{TR-TI}{T_{1a}}}) \cdot e^{-\frac{TI}{T_{1a}}} \cdot TI, \quad [1]$$

where eTE is the effective echo time (TE) of the VSS module, T_{2a} the transverse relaxation time (T_2) of arterial blood, CBF the cerebral blood flow under investigation, M_0 the fully relaxed magnetization, TR the repetition time, TI the interval between the VSS module and the image acquisition, and T_{1a} the longitudinal relaxation time (T_1) of arterial blood. The term TI is used here for consistency with previous VSASL literature, but is equivalent to PLD. Note that the arterial blood signal recovers from zero due to a global saturation applied immediately after image acquisition, whose purpose is to reset the magnetization (16).

Let α represent the saturation efficiency of VSS module (16):

$$\alpha = e^{-eTE/T_{2a}}, \quad [2]$$

and ΔM_z the longitudinal magnetization difference between the label and the control conditions (see Fig. 1c):

$$\Delta M_z = M_0 \cdot (1 - e^{-\frac{TR-TI}{T_{1a}}}) \cdot e^{-\frac{TI}{T_{1a}}} \quad [3]$$

Eq. 1 then becomes:

$$S_{1VSS} = \alpha \cdot CBF \cdot \Delta M_z \cdot TI. \quad [4]$$

In this study, a novel labeling strategy using multiple VSS modules is proposed to improve the SNR of VSASL, based on two effects: 1) additional VSS modules create larger magnetization difference between the label and the control conditions; 2) additional VSS modules can label the arterial spins that were outside of the scope of RF coil at the application of the first VSS module as they move in later, so the available bolus duration (BD) is effectively increased.

For simplicity, the case of using two VSS modules (Figs. 1b and 1d) is analyzed to demonstrate the SNR gain. Based on the magnetization states at the time of imaging, the spins that contribute to the ASL signal can be categorized into two groups: 1) one that is labeled only by the first VSS module (lab.1 in Fig. 1d), and 2) one that is labeled at least by the second VSS module (lab.2 in Fig. 1d).

For the first group of spins, at the application of the second VSS module, it has decelerated below Vc, and is therefore not labeled by the second VSS module. The magnetization under the label condition follows the dashed lines in Figure 1d. The magnetization difference between the label and the control conditions, ΔM_{z1}, is given by:

$$\Delta M_{z1} = M_0 \cdot (1 - e^{-\frac{TR-TI_1-TI_2}{T_{1a}}}) \cdot e^{-\frac{TI_1+TI_2}{T_{1a}}}, \quad [5]$$

and the corresponding ASL signal is:

$$S_{2VSS,tag1} = \alpha^2 \cdot CBF \cdot M_0 \cdot \left(1 - e^{-\frac{TR-TI_1-TI_2}{T_{1a}}}\right) \cdot e^{-\frac{TI_1+TI_2}{T_{1a}}} \cdot TI_1 = \alpha^2 \cdot CBF \cdot \Delta M_{z1} \cdot TI_1, \quad [6]$$

where TI_1 is the interval between the application of the first and the second VSS modules, and TI_2 the interval between the second VSS module and the imaging (Fig. 1b). Note that though the magnetization of the first group is not labeled by the second VSS module, it is still affected by the T2 relaxation during the second VSS module, resulting in the α^2 term.

The second group of spins consists of two subgroups: 1) one that is created only by the second VSS module, i.e., the spins entering the scope of the RF coil after the first VSS module (dot-dashed lines in Fig. 1d); and 2) one that is labeled by both the first and the second VSS modules, i.e., the spins that are labeled by the first VSS module and remain above Vc at the application of the second VSS module, but eventually decelerate below Vc at the time of imaging, whose magnetization follows dashed lines before and dot-dashed lines after the application of the second VSS module in Figure 1d. Let the relative proportions of the two subgroups' boluses be P_1 and P_2 respectively ($P_1 + P_2 = 1$). P_1 can then be estimated using:

$$P_1 = 1 - P_2 \approx \begin{cases} 0 & TI_1 + TI_2 \le BD \\ 1 - \frac{BD - TI_1}{TI_2} & TI_1 \le BD < TI_1 + TI_2 \\ 1 & BD < TI_1 \end{cases}, \quad [7]$$

where BD is the maximal BD created by one VSS module.

The first subgroup is not affected by the global saturation, so the magnetization under the control condition is fully relaxed (not shown in Fig. 1d), and the ASL signal of subgroup 1 is:

$$S_{2VSS,tag2,sub1} = \alpha \cdot CBF \cdot M_0 \cdot e^{-\frac{TI_2}{T_{1a}}} \cdot TI_2 \cdot P_1. \quad [8]$$

The ASL signal of subgroup 2 is:

$$S_{2VSS,tag2,sub2} = \alpha^2 \cdot CBF \cdot M_0 \cdot \left(1 - e^{-\frac{TR - TI_2}{T_{1a}}}\right) \cdot e^{-\frac{TI_2}{T_{1a}}} \cdot TI_2 \cdot P_2. \quad [9]$$

Combining Eqs. [7] and [8], and the fact that $P_1 + P_2 = 1$, the ASL signal of the second group is:

$$S_{2VSS,tag2} = S_{2VSS,tag2,sub1} + S_{2VSS,tag2,sub2} = \alpha^2 \cdot CBF \cdot M_0 \cdot e^{-\frac{TI_2}{T_{1a}}} \cdot TI_2 \cdot [\frac{P_1}{\alpha} + P_2 \cdot \left(1 - e^{-\frac{TR-TI_2}{T_{1a}}}\right)] = \alpha^2 \cdot CBF \cdot M_0 \cdot \left(1 - e^{-\frac{TR-TI_2}{T_{1a}}}\right) \cdot e^{-\frac{TI_2}{T_{1a}}} \cdot TI_2 \cdot \left\{1 + P_1 \cdot \left[\frac{1}{\alpha \cdot \left(1 - e^{-\frac{TR-TI_2}{T_{1a}}}\right)} - 1\right]\right\} = \alpha^2 \cdot CBF \cdot \Delta M_{z2} \cdot TI_2 \cdot (1 + P_1'), \quad [10]$$

where ΔM_{z2} is the magnetization difference of the subgroup 2 of the second group:

$$\Delta M_{z2} = M_0 \cdot \left(1 - e^{-\frac{TR-TI_2}{T_{1a}}}\right) \cdot e^{-\frac{TI_2}{T_{1a}}}, \quad [11]$$

and

$$P_1' = P_1 \cdot \left[\frac{1}{\alpha \cdot \left(1 - e^{-\frac{TR-TI_2}{T_{1a}}}\right)} - 1\right]. \quad [12]$$

With properly chosen imaging parameters $TI_{1/2}$ such that $TI_1 + TI_2 \leq BD$, $P_1 = 0$ and $P_1' = 0$. The total ASL signal generated by two VSS modules then simplifies to:

$$S_{2VSS} = S_{2VSS,tag1} + S_{2VSS,tag2} = \alpha^2 \cdot CBF \cdot (\Delta M_{z1} \cdot TI_1 + \Delta M_{z2} \cdot TI_2). \quad [13]$$

The contribution of groups 1 and 2 to the total bolus of labeled blood is weighted (and can be adjusted) by TI_1 and TI_2 respectively.

However, as shown in Eqs. 7 and 12, if the condition $TI_1 + TI_2 \leq BD$ is not satisfied, then $P_1' > 0$, using Eq. 13 may underestimate the SNR gain or overestimate the CBF. In this case, Eq. 13 is recommended to quantify CBF with the imaging parameters and the P_1 value calculated with Eq. 7, given an empirical or measured value of BD. In case of unknown BDs, the potential range of CBF overestimation can be estimated by comparing the values obtained by Eqs. 10 and 13, given an assumed range of P_1 values.

The labeling process utilizing three or more VSS modules follows the derivation above. However, for N VSS modules, the labeling efficiency term is α^N, and more modules are beneficial only when the SNR gain by application of additional VSS modules is larger than the additional T2 relaxation during labeling.

Methods

Simulations

To examine the SNR gains by applying multiple VSS modules, the SNR efficiencies of VSASL with 1, 2 or 3 VSS modules (VSASL-1VSS, VSASL-2VSS and VSASL-3VSS respectively) were simulated in MATLAB 2012a (The Mathworks, Nantick, USA). The SNR efficiency is defined as $S_{ASL}/\sqrt{2TR}$, where S_{ASL} is the ASL signal measured in 2 TRs (a pair of label/control acquisitions). For comparison, the SNR efficiencies of PASL and PCASL were also simulated. For all the labeling methods, the maximal SNR efficiency was calculated at each TR (from 1 to 8 s, with a step size of 0.05 s), and then normalized to that of the VSASL-1VSS at TR of 1 s. A T1 of 1.66 s and a T2 of 0.15 s were assumed for arterial blood. An imaging time of 0.3 s was assumed.

In VSASL simulations, an eTE of 20 ms ($\alpha \approx 0.88$) and a maximal BD of 2.0 s (compared with an unlimited BD) were used for each VSS module. At each TR, the maximal ASL signal and the SNR efficiency were calculated using Eq. 13 by searching through the available range of TIs. At the optimized point, the potential effect of CBF overestimation using Eq. 13 was simulated with P_1 ranging from 0 to 0.5.

In simulations using PASL and PCASL, scenarios of TDs being 1.5 and 2 s were considered, so the corresponding PLDs of 1.5 and 2 s were used to obtain the maximal SNR efficiency. For PCASL, a TD of 2.5 s was also considered, as this scenario may be relevant in

practice (see Discussion). For PASL, a labeling efficiency of 0.97 (9) was used. In PASL and VSASL, the maximal BD is limited by the spatial extent of the transmit RF coil. We have measured a value of 1.3 s for PASL, and a value of 2.0 s for VSASL, and used these for our simulations. For PCASL, a labeling efficiency of 0.80 (6,17) was used, and the BD was assumed to be TR minus the imaging time and the TD.

In vivo Experiments

All the *in vivo* scans were carried out on a 3-Tesla GE scanner (Discovery MR750, GE Healthcare, Waukesha, WI, USA) with a commercial 8-channel receive-only head coil under an IRB-approved protocol.

CBF measurements

Seven young, healthy volunteers (6M, 1F, age 33.4 ± 3.8 y/o) were scanned to measure CBF in gray matter (GM) and white matter (WM).

VSASL: VSASL-1VSS and VSASL-2VSS were tested. To minimize erroneous labeling of static tissue from eddy current effects, the symmetric BIR-8 (sym-BIR-8) design (18) was used as the VSS module, where the RF sub-pulses of BIR-8 are evenly spaced with flow-weighting gradient pulses with a ramp time of 0.5 ms and a maximum amplitude of 20 mT/m. A delay of 0.1 ms before and a delay of 2 ms after each gradient pulse were also inserted to further reduce eddy current effects (18). The Vc was 2 cm/s in the S/I direction in both labeling and imaging. The eTE of each VSS module was determined to be 21.4 ms through Bloch simulations with assumed T1 of 1.66 s and T2 of 0.15 s for arterial blood.

From the simulations to maximize the SNR efficiencies at the TR of 4.5 s, optimized TIs were determined to be 1.3 s for the VSASL-1VSS scans and TI1/TI2 of 1.15/0.82 s for the VSASL-2VSS scans. Given a measured BD value of 2.0 s (see below), the TIs used in the VSASL-2VSS scans satisfied that $TI_1 + TI_2 \leq BD$, so CBF could be quantified using Eq. 13

without bias. To improve the SNR, two global background suppression (BGS) pulses (19) were applied at 1290 ms and 320 ms prior to image acquisition in VSASL-1VSS scans, and 790 ms and 190 ms prior to image acquisition in VSASL-2VSS scans. Another set of VSASL-2VSS data was collected with a modified second VSS module and one BGS pulse at 190 ms prior to image acquisition (VSASL-2VSS-1BGS). This modified VSS module had an additional phase of π on the last BIR sub-pulse to tip down instead of up spins at the end of the module, effectively serving as a combined VSS and BGS module with reduced specific absorption rate (SAR) and SNR loss due to imperfection of the BGS pulse, without compromising the overall BGS efficiency. Alternative implementations include: 1) addition of phase of $\pi/4$ to the 2nd, 3rd, 6th and 7th segments of the BIR-8 pulses; or 2) addition of phase of $3\pi/2$ to the 2nd and 3rd segments; or 3) addition of phase of $3\pi/2$ to the 6th and 7th segments. All these modifications can achieve the same performance with regards to the velocity sensitivity and off-resonance effects, according to Bloch simulation.

Other parameters included: seven 6 mm-thick slices with 6 mm gaps, field of view (FOV) = 220 × 220 mm, spin echo with matched-phase RF pulses (20), TR/TE = 4.5 s/ 17.9 ms, fat saturation before excitation, spiral readout with a matrix of 64 × 64, 30 pairs of label and control following 2 dummy repetitions, global saturation pulses at the end of image acquisition.

PASL: CBF maps using PASL (PICORE QUIPSS II (5,9)) were collected with the same imaging parameters as in VSASL. Other parameters were: hyperbolic secant inversion pulse, inversion slab thickness = 200 mm, 20 mm gap between labeling and imaging slabs, TI/TI1 = 2.4 s/0.8 s (PLD = 1.6 s) and two BGS pulses applied at 1190 ms and 310 ms prior to image acquisition, TR/TE and flow crushing gradients matched to that of the VSASL scans to minimize any potential contamination from intravascular signals. Note that the TI was longer

than that typically used to ensure a complete delivery of labeled blood and an accurate quantification of CBF.

PCASL: PCASL scans used the following labeling parameters: 375 μs Hamming shaped pulses with a maximal B1 of 10 μT (a nominal flip angle of 31.1°) and 1 ms spacing, labeling gradients with 16 mT/m amplitude and 0.9 mT/m mean value, 2 s label duration, 2 s PLD, 46.7 ± 2.8 mm (mean ± standard deviation (STD)) gaps between labeling (on a relatively straight part of the internal carotid arteries and vertebral arteries) and imaging slabs, two BGS pulses applied at 1190 ms and 310 ms prior to image acquisition, and TR/TE and flow crushing gradients matched that in the VSASL scans.

For CBF quantification, four reference images were collected to estimate the receive-coil sensitivity map and the conversion factor between MR signal and the amount of arterial blood from fully relaxed cerebrospinal fluid (CSF) signal. High-resolution anatomical images were collected to generate partial volume ratio maps (Fig. 2a) of GM, WM and CSF using AFNI (21), and then were down-sampled (Fig. 2b) to generate GM and WM regions of interest (ROIs, Fig. 2c).

ASL signals were calculated and averaged across repetitions. The signal attenuation from BGS was compensated with an inversion efficiency of 0.97 for each inversion pulse used. Note that because the b-values of the VSS preparations were non-zero in the label condition but zero in the control condition, a diffusion attenuation difference between these two conditions was expected. To avoid CBF overestimation from this cause, the amount of attenuation difference, $p_t M e^{(-\mathrm{b}*\mathrm{D}_t)}$, was estimated and removed, where p_t is the partial volume fraction of tissue t (GM, WM or CSF), M is the magnetization of the voxel at the time of application of the VSS module, b is the b-value of the VSS module and D_t is the diffusion coefficient of tissue t (8.9 × 10-4 mm2/s, 7.0 × 10-4 mm2/s and 2.9 × 10-3 mm2/s for GM, WM (22) and CSF (23),

respectively). Note that the diffusion attenuation correction was applied on each VSS module used. The acquisition time for each slice was accounted in the calculation of the actual TI for each slice and the CBF values were then calculated using a modified dynamic ASL model (24).

Averaged ASL signals and CBF values were calculated across the GM and WM ROIs for each subject. The ASL signal was treated as direct indicator of SNR, as the noise levels were comparable with similar BGS levels. The temporal STDs (tSTDs) of CBF were also reported. Note that the tSTDs of ASL signal were not reported because they are simply the tSTDs of CBF scaled by an ASL-CBF conversion constant in each subject.

Multi-TI ASL experiments

In order to validate the timing parameters used in mm-VSASL and to verify the TD insensitivity of VSASL, the BDs and TDs using VSASL were measured by collecting ASL data at multiple TIs. For comparison, TDs and BDs using PASL and PCASL were also measured. Five young, healthy volunteers (4M, 1F, age 30.2 ± 1.9 y/o) were included in these experiments. The imaging parameters were the same as in the previous CBF measurements, except that: TR/TE = 5 s/ 14.7 ms, the readout matrix = 48 × 48, 16 pairs of label and control following 2 dummy repetitions, no BGS. Note that the flow-crushing gradients with Vc = 2 cm/s along the S/I direction were necessary to remove intravascular signals, especially in the acquisitions with short TIs. The labeling parameters are listed below.

VSASL: VSASL-1VSS with Vc = 2 cm/s along the S/I direction, and TIs = [0.6, 1.2, 1.8, 2.4, 3.0, 3.6, 4.2] s.

PASL: PICORE without QUIPSS II, inversion slab thickness = 200 mm, a 20 mm gap between labeling and imaging slabs, and TIs = [0.6, 1.2, 1.8, 2.4, 3.0, 3.6, 4.2] s.

PCASL: The gaps between the labeling and imaging slabs were 47.2 ± 5.4 (mean ± STD) mm, label durations = [0.55, 1.15, 1.75, 1.75, 1.75, 1.75, 1.75] s at corresponding TIs = [0.6, 1.2, 1.8, 2.4, 3.0, 3.6, 4.2] s, with PLDs = [0.05, 0.05, 0.05, 0.65, 1.25, 1.85, 2.45] s. Note

that instead of using one fixed (and small) value in all the scans, the label durations were adjusted at different TIs. This should improve the SNRs in the scans with long TIs while retaining the capability of detecting short TDs with ASL signals measured at short TIs.

High-resolution anatomical images were also collected to generate partial volume ratio maps of GM, WM and CSF, and GM ROIs.

The VSASL signals measured in multi-TI experiments were corrected for diffusion attenuation effects as done previously. The ASL signals collected with PASL, PCASL and VSASL were spatially smoothed by a 3x3 Gaussian kernel with a σ of 0.65, and then fitted to a kinetic ASL signal model (24) for the TDs and BDs per voxel. For the data collected with PCASL, only TD maps were calculated from the model with assumed BDs equal to the labeling durations used in the experiments. Note that in the process of fitting the VSASL data, the TDs were allowed to be negative, so the effects of noise and/or artifact that may shift the TDs to below zero can be observed. Fitted BDs associated with negative TDs were modified by $BD_{output} = BD_{fit} + TD_{negative}$, so the BDs in these voxels were correctly estimated. To minimize potential bias from noisy pixels, only the middle 95% (i.e., from 2.5% to 97.5%) of fitted TDs and BDs were analyzed. To demonstrate the goodness of the fits, R2 maps were also calculated for each preparation method.

Results

Simulations

Normalized SNR efficiencies of PASL and PCASL and VSASL are shown in Figure 3. The TI and TI1/TI2 used to reach the maximal SNR efficiencies in VSASL-1VSS and VSASL-2VSS at each TR are shown in Figure 3b and c respectively. The SNR efficiencies of VSASL using an unlimited BD and a BD of 2.0 s were identical. As shown in Figures 3b and 3c, a BD

of 2.0 s is more than sufficient to achieve optimal SNR efficiencies at TR ∈ [1, 8] s. Compared with VSASL-1VSS at the same TR, using 2 VSS modules improved the SNR efficiency by a minimal value of 18.1% at TR of 1 s and a maximal value of 26.0% at TR of 8 s. The maximal SNR efficiency of VSASL-1VSS was reached at TR = 4.9 s and TI = 1.4 s. The maximal SNR efficiency of VSASL-2VSS was reached at TR = 5.1 s and TI1/TI2 = 1.3 s/0.9 s, with an improvement of 24.4% compared to VSASL-1VSS. Potential CBF overestimation was estimated to be less than 7.6% with these imaging parameters and the P_1 values ranging from 0 to 0.5. However, adding the third VSS module only improved the SNR efficiency marginally, with an improvement of 26.9% compared to VSASL-1VSS (the dotted red line in Fig. 3a). This is because the ASL signal gain introduced by the third VSS module was mostly canceled by the additional attenuation from T2 relaxation.

For PASL, the maximal SNR efficiency was reached when the TR was just long enough to include the designated BD, PLD and the imaging time. This is because the maximal ASL signal available is determined once the BD is fixed, so the maximal SNR efficiency will be achieved when the minimal TR (with minimal T1 relaxation) is used: TR = 3.1 s with PLD = 1.5 s and TR = 3.6 s with PLD = 2 s. For PCASL, long TRs allow long labeling durations to be used, which increase ASL signals; however, the signal attenuation from T1 relaxation is also increase as the image acquisition is delayed. So its maximal SNR efficiencies will be achieved when these two competing factors reach balance – in the simulation, they were achieved at TR = 5, 5.7 and 6.4 s with PLD = 1.5, 2 and 2.5 s accordingly.

VSASL was capable of acquiring ASL signal at very short TRs (< 2 s, Fig. 3a), where PASL and PCASL were typically not, due to the TD effect, unless the timing of labeling and acquisition is arranged so that the ASL signal acquired is from previous instead of current TR, e.g., as in (25). With a short TD/PLD (1.5 s), PCASL gave the highest SNR efficiency and VSASL-2VSS had higher SNR efficiency than PASL at TR > 4 s. For both PASL and PCASL,

the SNR efficiencies were compromised when the PLD increased, due to increased T1 relaxation. At PLD = 2 s, the SNR efficiency of PASL was the lowest among the three; while the SNR efficiency of VSASL-2VSS was higher than that of PCASL at TR < 4 s, but lower at TR > 4 s. At TD/PLD = 2.5 s, VSASL-1VSS gave comparable maximal SNR efficiency with PCASL, while VSASL-2VSS provided significantly higher SNR efficiency than PCASL.

CBF Measurements

The ASL signal and quantitative CBF maps of one representative slice calculated from PASL, PCASL, VSASL-1VSS, VSASL-2VSS and VSASL-2VSS-1BGS data are shown in Figure 4 for all the seven subjects. Averaged ASL and CBF values within the GM and WM ROIs are reported in Table 1. GM/WM CBF ratios were also calculated. Pair-wise t-tests were performed on the ASL, CBF values and the GM/WM CBF ratios, and the P-values are tabulated in Table 2. Note that the significance detection level was set at 0.005 for the multiple comparisons with Bonferroni correction applied.

PASL had the lowest SNRs in both GM ($P \leq 6.6 \times 10\text{-}6$) and WM ($P \leq 1.6 \times 10\text{-}4$) ROIs among all the preparations. Compared with PCASL, VSASL-1VSS data had slightly lower (not significantly in GM with P = 0.013, but significantly in WM with $P = 5.1 \times 10\text{-}4$). There was no significant difference between the SNR of the ASL signal measured by VSASL-2VSS and VSASL-2VSS-1BGS (P = 0.38 and 0.68 in GM and WM, respectively), so they were averaged together. Overall, VSASL-2VSS provided higher SNRs than PCASL, significantly so in GM ($P = 4.3 \times 10\text{-}3$), though not significantly so in WM (P = 0.46). Compared with VSASL-1VSS, using two VSS modules significantly improved the SNRs in both GM (19.0 ± 2.2%, mean ± stand error of the mean (SEM), $P = 2.3 \times 10\text{-}4$) and WM (25.2 ± 2.9%, $P = 7.1 \times 10\text{-}5$). The averaged SNR gain over GM and WM was 22.1 ± 1.9% ($P = 1.7 \times 10\text{-}6$), matched well with that of 22.7% predicted by simulation using the same preparation and imaging parameters.

This validated our ASL signal model of using two VSS modules. In addition, the raw tissue signal levels were identical between VSASL-2VSS and VSASL-2VSS-1BGS scans (data not shown), indicating that the modified VSS module successfully served as a BGS pulse, with reduced overall SAR.

Averaged CBF values are listed in Table 1. Averaged GM/WM CBF ratio across subjects and the preparations was 2.37 ± 0.04 (mean ± SEM). All the GM and WM CBF values and GM/WM CBF ratios were in expected physiological range, and were consistent with the values reported in literatures (11,26,27). There was no significant difference between the GM/WM CBF ratios measured by different preparations, except between PCASL and VSASL-1VSS (Table 2), which could likely be caused by residual artifact from diffusion attenuation. The lowest CBF values in both GM and WM ROIs were reported by PASL, likely due to the compromised SNRs. However, only GM CBF values measured by PASL were significantly lower than that by VSASL-1VSS and VSASL-2VSS (Table 2). There was no other significant difference between the CBF values measured by different preparations tested, in GM or WM ROIs.

Multi-TI Experiments

Exemplary ASL signal maps acquired from the middle three slices in subject 5 using PASL, PCASL and VSASL at different TIs are shown in Figure 5a, with the averaged ASL signals in GM ROIs shown in Figure 5b. Corresponding TD, BD and R2 maps are shown in Figure 5c (see supplementary material for results from the other 4 subjects). Note that due to relatively low SNRs and therefore compromised goodness of the fits in WM ROIs (see R2 maps in Fig. 5c), only the TDs and BDs within the GM ROIs were analyzed, and their distributions are shown in Figure 5d. For both PCASL and PASL, the ASL signals in most GM regions were not detected at TI = 0.6 s, and delayed delivery of arterial blood in the posterior and territory

boundary regions compared to other regions can be observed at later TIs, demonstrating the existence of TDs associated with these two labeling methods. The spatial distributions of TDs fitted from the PCASL and PASL data were consistent with each other as expected, suggesting the validity of the fitting process. In contrast, VSASL did not show strong TD effects in the ASL images, and the fitted TDs in most of the GM were distributed around zero, as predicted by theory. However, the distribution was skewed towards negative values (Fig. 5d), likely due to contamination from residual diffusion attenuation and/or eddy current effects. The voxels with relatively large negative TDs were found mostly close to vessels or ventricles, suggesting possible presence of double-tagging effect (28). Both effects may artificially increase the ASL signal measured at short TIs, resulting in negative-biased TDs. The BDs measured by VSASL in this study were less likely to be affected by these contaminations, because 1) the two effects should have less impact on data collected at later TIs, especially that from the double-tagging effect (28); and 2) the increased portion in BDs due to negative TDs was removed (see Methods). The BDs measured in GM from the PASL and VSASL data were in a reasonable range, and those from the PASL data were consistent with values reported by others (29,30).

Means, medians and STDs of TDs and BDs in each slice are shown in Figure 6a and b for each subject. Note that due to the skewed distribution of TDs, the median instead of mean values should reflect the true values more accurately, therefore they are reported. For both PCASL and PASL, the TDs increased as the slice moved higher, because it takes more time for arterial blood to be delivered to more distal locations. On the other hand, the TDs using VSASL remained relatively constant and close to zero in all the slices, demonstrating the TD insensitivity of VSASL. PCASL showed longer TDs than PASL ($P = 4.4 \times 10\text{-}15$), likely because the gaps between the labeling and imaging regions were bigger in PCASL than that in PASL (47.2 ± 5.4 mm vs. 20 mm). A Bland-Altman plot of the TDs measured using PCASL and PASL from different slices and subjects is shown in Figure 6c, with a mean difference of

0.23 s and a 95% confidence interval (CI) of [0.03, 0.43] s. The findings with regards to the TDs using PASL and PCASL were consistent with results reported in (31). The BDs measured using VSASL were significantly longer than that using PASL (P = 5.2 × 10-10). The BD difference was larger in higher slices, indicating the labeling of arterial blood within the imaging slab using VSASL, as expected. The Bland-Altman plot of the BDs measured using PASL and VSASL is shown in Figure 6d, with the mean difference and 95% CI being 0.64 s and [-0.23, 1.52] s, respectively.

The TDs and BDs averaged across slices are summarized in Table 3. Across the five subjects, the averaged TDs were (mean ± SEM): 1.16 ± 0.07 s, 0.93 ± 0.08 s and -0.09 ± 0.07 s for PCASL, PASL and VSASL respectively, and the averaged BDs were (mean ± SEM): 1.38 ± 0.09 s, 2.03 ± 0.08 s for PASL and VSASL respectively. Compared to PASL and PCASL, VSASL was indeed insensitive to TD effects as expected.

Discussion

The SNR improvement using two VSS modules was demonstrated through simulations and verified in *in vivo* experiments. The improvement can be explained by combination of bigger label/control difference created by re-saturation at later times, and lengthened effective BD. The former was demonstrated to be the dominant source of the SNR gain in this study. However, in practice, the latter may contribute significantly if the condition $TI_1 + TI_2 \leq BD$ is not met, e.g., if the BD is small due to limited coverage of a local RF coil and/or fast bulk blood flow. The consistency of SNR improvements through simulations and *in vivo* experiments supports the validity of the mm-VSASL model.

As discussed in the Theory, the T2 relaxation of VSS module affects the overall achievable SNR improvement using mm-VSASL: the less T2 relaxation, the higher SNR improvement. In this study, sym-BIR-8 VSS modules were used to trade off some of the SNR

gain for more accurate perfusion quantification with minimized eddy current effects; however, with the technical development in pulse design and/or hardware to further reduce eddy current effects, it may allow more efficient (less T2 relaxation) and/or more number of VSS modules to be used to maximize the SNR efficiency gain. For instance, if the eTE is reduced to 10 ms for each VSS module, then the SNR efficiency improvement will be 33.5% and 45.5% for VSASL-2VSS and VSASL-3VSS respectively.

As demonstrated in both the simulations and the *in vivo* experiments, mm-VSASL was able to achieve SNR efficiencies that were significantly higher than PASL and comparable to PCASL with reasonable PLDs (~2 s, see Figs. 3 and 4, Table 1). In practice, slightly long/conservative PLDs (e.g., 2.5 s) may be considered using PCASL, even in healthy subjects, to accurately measure GM CBF without underestimation in some brain regions, as demonstrated in (26), where underestimation of GM CBF at border regions was observed in some subjects with PLD = 1.5 s compared to that with PLD = 2.5 s using PCASL. In cases of long TDs (e.g., ≥ 2.5 s), VSASL should be the best option among the three ASL categories with highest SNR efficiency and insensitivity to TD effects, or perhaps in the worst cases the only option if the TDs are so long that ASL signals are not practically detectable using PASL or PCASL.

Compared to PCASL, VSASL yielded slightly higher CBFs values, though not significantly so (Table 2). This may be explained by: 1) possible overestimation of CBF using VSASL caused by the residual artifact from the diffusion attenuation correction and/or eddy current effects, or unaccounted ASL signal from labeling of replenished arterial blood; or 2) possibly some regional perfusion underestimation using PCASL from compromised labeling efficiency due to off-resonance effects at the labeling planes, and/or TD sensitivity even with the relatively conservative PLDs used.

The data and fitted results of multi-TI experiments provided direct experimental evidence to demonstrate the TD insensitivity of VSASL. However, the artifact from eddy current and double-tagging effects might have contaminated the data, especially at early TI, resulting in slightly shifted TDs. Unreliable fitting results were seen in the WM regions in analysis of PCASL, PASL and VSASL data, where the SNR was relatively low. To accurately measure the TDs in the WM regions, high SNR data, e.g. with more repetitions or lower spatial resolution, are required.

Measured BDs validated that used in the PASL and VSASL simulations. For VSASL, a finite BD of 2 s, as measured in this study, is more than sufficient to achieve maximal SNR efficiency. There was no evidence that conventional VSASL had inaccurately quantified CBF due to the actual BD being shorter than the assumed value. On the other hand, mm-VSASL allows shorter BDs to be used for each VSS module to achieve the maximal SNR efficiency at a given TR, so it should be even less likely to inaccurately quantify CBF if there is discrepancy between the actual and the assumed BD values.

Finally, there are also some potential concerns using mm-VSASL. First, as the VSS modules are applied more than once, it is possible that the artifacts from eddy current effects may be more profound, so caution must be taken, e.g., using VSS modules that are insensitive to eddy current effects. Second, as the diffusion attenuation correction is applied on each VSS module used, the more VSS modules used the less accurate the correction may be. Third, though there was no issue concerning SAR at 3 Tesla as in this study, there could be potential concerns at higher fields using multiple VSS modules.

Conclusions

It has been demonstrated through simulations and *in vivo* experiments that utilizing multiple VSS modules can increase the SNR efficiency of VSASL to levels comparable to or

even higher than that of PCASL with reasonable PLDs. The TD insensitivity of VSASL, as experimentally verified in this study, also helps mm-VSASL provide perfusion quantification with improved accuracy. With these two advantages, mm-VSASL should be suitable in applications where long/heterogeneous TDs are of concern due to physiological or pathological reasons.

Table 2.1. Averaged ASL signals (a.u.), CBF values (mean ± tSTD, unit ml/min/100 g) across GM and WM ROIs and GM/WM (G/W) ratios for each subject and across subjects (mean ± SEM).

	Seq.	PASL		PCASL		VSASL-1VSS		VSASL-2VSS		VSASL-2VSS-1BGS	
Sub.	ROI	GM	WM	GM	WM	GM	WM	GM	WM	GM	WM
1	ASL	15.6	7.6	23.9	12.0	21.5	8.7	25.7	10.9	26.6	11.6
	CBF	45.7 ± 3.5	21.6 ± 2.1	46.1 ± 5.1	22.5 ± 2.3	50.3 ± 4.1	20.4 ± 2.6	49.1 ± 7.2	21.0 ± 4.2	49.3 ± 5.0	21.6 ± 3.4
	G/W Ratio	2.11		2.04		2.47		2.34		2.29	
2	ASL	11.3	5.1	19.6	9.0	18.7	7.8	23.2	10.5	24.3	10.9
	CBF	42.9 ± 14.4	19.0 ± 6.0	49.2 ± 8.6	22.0 ± 4.1	56.9 ± 8.4	23.7 ± 4.1	57.5 ± 12.9	26.1 ± 6.2	58.5 ± 8.5	26.2 ± 4.1
	G/W Ratio	2.26		2.23		2.40		2.20		2.24	
3	ASL	13.6	5.1	24.5	9.6	21.0	7.3	25.3	9.6	25.8	9.8
	CBF	40.0 ± 1.9	14.8 ± 1.5	47.4 ± 5.6	18.3 ± 2.7	49.6 ± 6.3	17.3 ± 3.3	48.8 ± 6.8	18.4 ± 3.8	48.2 ± 5.1	18.3 ± 2.8
	G/W Ratio	2.69		2.59		2.86		2.65		2.64	
4	ASL	15.8	7.4	24.4	12.6	25.1	11.1	26.6	12.5	26.3	12.0
	CBF	48.9 ± 4.4	22.2 ± 2.1	49.6 ± 7.0	24.7 ± 3.4	61.7 ± 9.7	27.4 ± 5.4	53.4 ± 9.7	25.2 ± 6.8	51.2 ± 9.1	23.4 ± 5.8
	G/W Ratio	2.20		2.01		2.25		2.12		2.19	
5	ASL	17.3	7.9	27.9	12.5	25.8	10.6	30.1	13.8	27.8	12.1
	CBF	50.4 ± 3.8	22.5 ± 2.1	53.2 ± 6.4	23.4 ± 4.7	59.9 ± 4.9	24.7 ± 3.5	57.2 ± 5.2	26.2 ± 5.3	51.2 ± 3.3	22.3 ± 4.1
	G/W Ratio	2.24		2.27		2.42		2.18		2.29	
6	ASL	16.9	6.9	28.3	10.5	26.4	9.3	31.3	10.8	32.4	11.0
	CBF	53.4 ± 6.0	21.4 ± 2.1	58.7 ± 9.7	21.4 ± 5.9	66.6 ± 10.4	23.5 ± 4.7	64.5 ± 6.0	22.3 ± 4.3	64.7 ± 9.4	22.1 ± 8.1
	G/W Ratio	2.49		2.74		2.84		2.89		2.93	
7	ASL	12.2	5.8	22.2	10.5	18.6	8.4	21.5	9.7	24.7	11.8
	CBF	36.0 ± 2.7	16.6 ± 1.5	42.8 ± 7.5	20.0 ± 4.6	43.8 ± 7.2	19.9 ± 4.5	41.2 ± 5.1	18.7 ± 3.0	46.0 ± 7.0	22.0 ± 4.4
	G/W Ratio	2.16		2.14		2.20		2.20		2.09	
Mean	ASL	14.7 ± 0.9	6.5 ± 0.5	24.4 ± 1.1	11.0 ± 0.5	22.4 ± 1.2	9.0 ± 0.5	26.3 ± 1.3	11.1 ± 0.6	26.9 ± 1.0	11.3 ± 0.3
	CBF	45.3 ± 2.3	19.8 ± 1.1	49.6 ± 1.9	21.8 ± 0.8	55.5 ± 3.0	22.4 ± 1.3	53.1 ± 2.9	22.6 ± 1.3	52.7 ± 2.5	22.3 ± 0.9
	G/W Ratio	2.31 ± 0.08		2.29 ± 0.10		2.49 ± 0.10		2.37 ± 0.11		2.38 ± 0.11	

Table 2.2. The P-values of the pair-wise t-tests on ASL signal, CBF values within the GM and WM ROIs and corresponding G/W ratios using PASL, PCASL, VSASL-1VSS, VSASL-2VSS and VSASL-2VSS-1BGS.

The P-values reached significance are labeled by "*" ($P < 0.005$, with Bonferroni correction applied).

			PCASL	VSASL-1VSS	VSASL-2VSS	VSASL-2VSS-1BGS
ASL	GM	PASL	1.1×10^{-6} *	6.6×10^{-6} *	2.2×10^{-6} *	1.8×10^{-6} *
		PCASL		0.013	0.014	7.0×10^{-3}
		VSASL-1VSS			1.5×10^{-4} *	1.0×10^{-3} *
		VSASL-2VSS				0.38
	WM	PASL	5.3×10^{-7} *	1.6×10^{-4} *	1.2×10^{-5} *	5.1×10^{-6} *
		PCASL		5.1×10^{-4} *	0.71	0.39
		VSASL-1VSS			2.3×10^{-4} *	6.3×10^{-4} *
		VSASL-2VSS				0.68
CBF	GM	PASL	8.8×10^{-3}	2.0×10^{-4} *	2.1×10^{-3} *	0.011
		PCASL		6.0×10^{-3}	0.024	0.062
		VSASL-1VSS			0.060	0.18
		VSASL-2VSS				0.79
	WM	PASL	9.4×10^{-3}	0.016	0.02	0.063
		PCASL		0.37	0.34	0.54
		VSASL-1VSS			0.82	0.88
		VSASL-2VSS				0.72
G/W Ratio		PASL	0.73	0.0079	0.42	0.33
		PCASL		0.0047 *	0.15	0.075
		VSASL-1VSS			0.026	0.031
		VSASL-2VSS				0.68

Table 2.3. Averaged TDs and BDs using PCASL, PASL and VSASL across GM ROIs in each subject (mean ± SEM, unit s).

Sequence	PCASL	PASL		VSASL	
Subject	TD	TD	BD	TD	BD
1	1.35 ± 0.11	1.11 ± 0.11	1.34 ± 0.04	0.11 ± 0.04	1.94 ± 0.13
2	1.31 ± 0.10	1.13 ± 0.08	1.62 ± 0.09	-0.15 ± 0.05	2.03 ± 0.08
3	1.08 ± 0.08	0.77 ± 0.08	1.06 ± 0.05	-0.28 ± 0.03	2.25 ± 0.11
4	1.03 ± 0.07	0.79 ± 0.09	1.44 ± 0.06	-0.12 ± 0.04	2.13 ± 0.07
5	1.03 ± 0.09	0.84 ± 0.11	1.44 ± 0.12	-0.03 ± 0.03	1.78 ± 0.05
Average	1.16 ± 0.07	0.93 ± 0.08	1.38 ± 0.09	-0.09 ± 0.07	2.03 ± 0.08

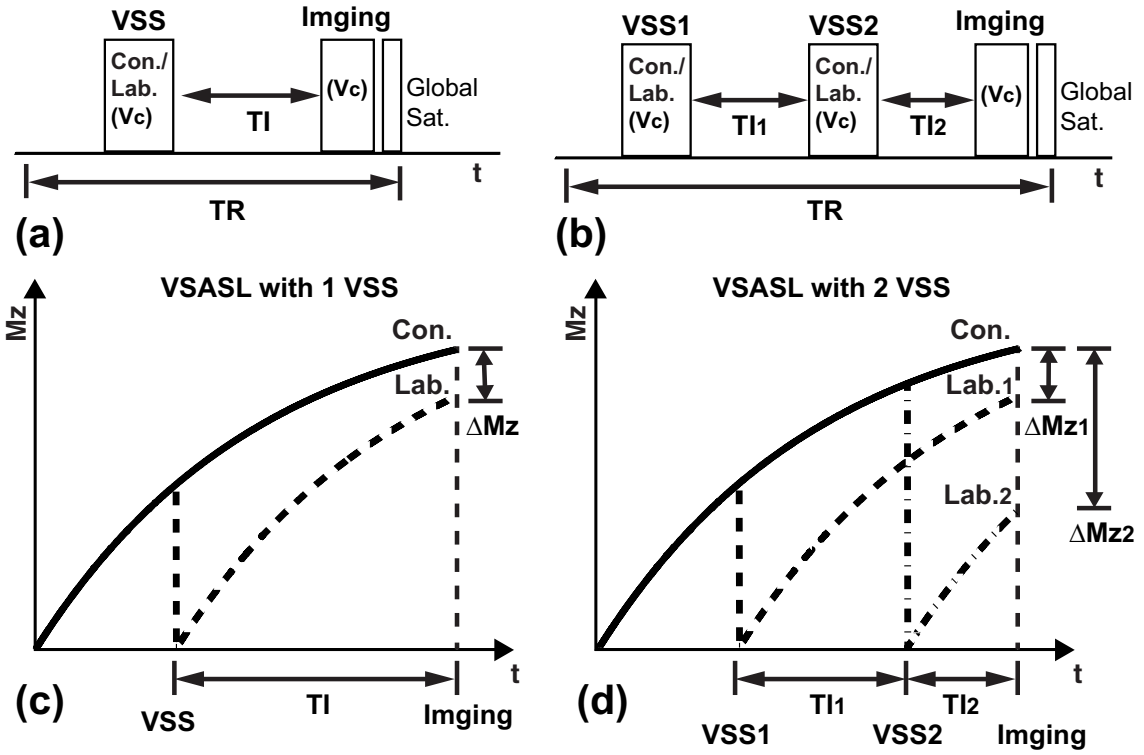

Figure 2.1. Sequence diagrams and Schematic description of conventional VSASL (a, c), and VSASL using two VSS modules (b, d).

In c and d, the solid curves represent the magnetization of arterial blood under control condition. The dashed curve in (c) represents the magnetization of arterial blood under label condition. The dashed curve in (d) represents the magnetization of arterial blood that is labeled only by the first VSS module. The dot-dashed curve in (d) represents the magnetization of arterial blood that is labeled only by the second VSS module. The magnetization of arterial blood that is labeled by both VSS modules follows the dashed curve before and the dot-dashed curve after the application of the second VSS module.

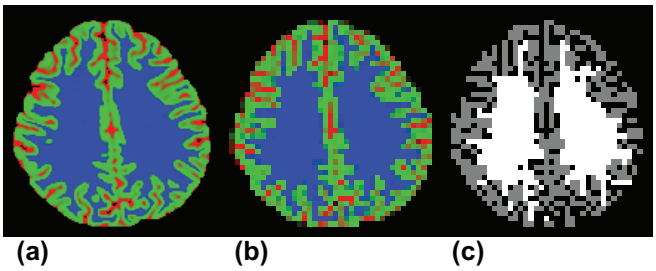

Figure 2.2. Examples of partial volume maps (GM in green, WM in blue and CSF in red) at high (a) and low (b) resolutions, and generated GM and WM ROIs (c) (GM in gray, WM in white).

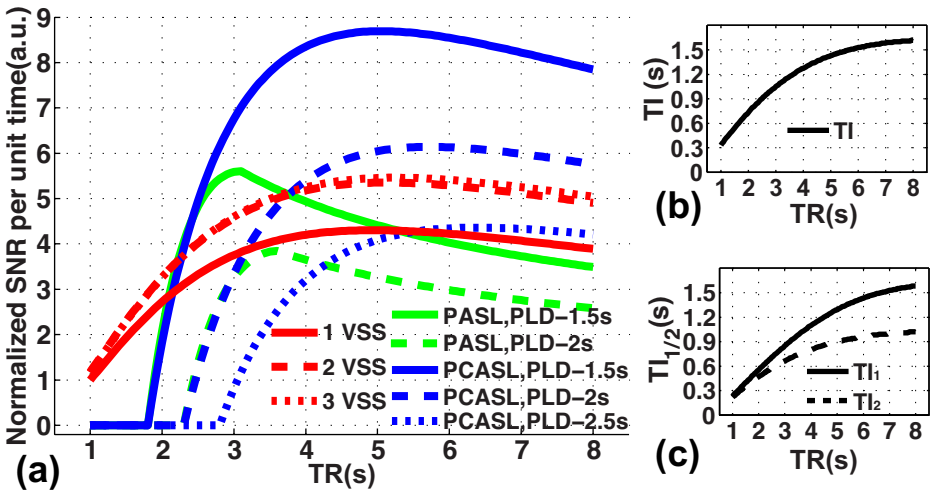

Figure 2.3. Simulation results showing the maximal SNR efficiencies using different ASL preparations at given TRs (a) and the TIs to achieve the maximal SNR efficiencies using VSASL with one (b) or two (c) VSS modules.

SNR efficiencies of VSASL with one, two or three VSS modules are depicted with solid, dashed and dotted red curves respectively. SNR efficiencies of PASL with PLDs of 1.5 s and 2 s are depicted with solid and dashed green curves respectively. SNR efficiencies of PCASL with PLDs of 1.5 s, 2 s and 2.5 s are depicted with solid, dashed and dotted blue curves respectively.

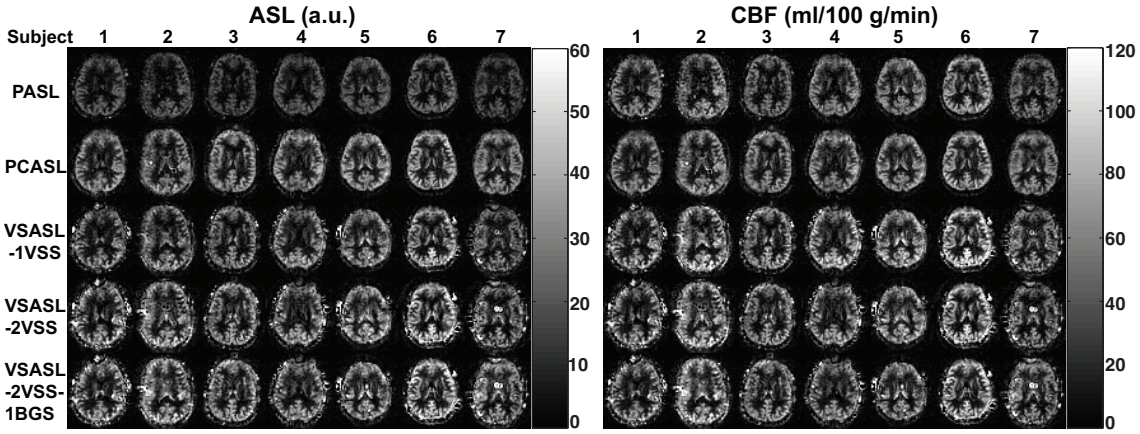

Figure 2.4. Examples of ASL (left panel) and quantitative CBF (right panel) maps measured with different preparations for all the seven subjects (only one slice is shown).

The rows of maps from top to bottom were acquired with PASL, PCASL, VSASL-1VSS, VSASL-2VSS and VSASL-2VSS-1BGS respectively.

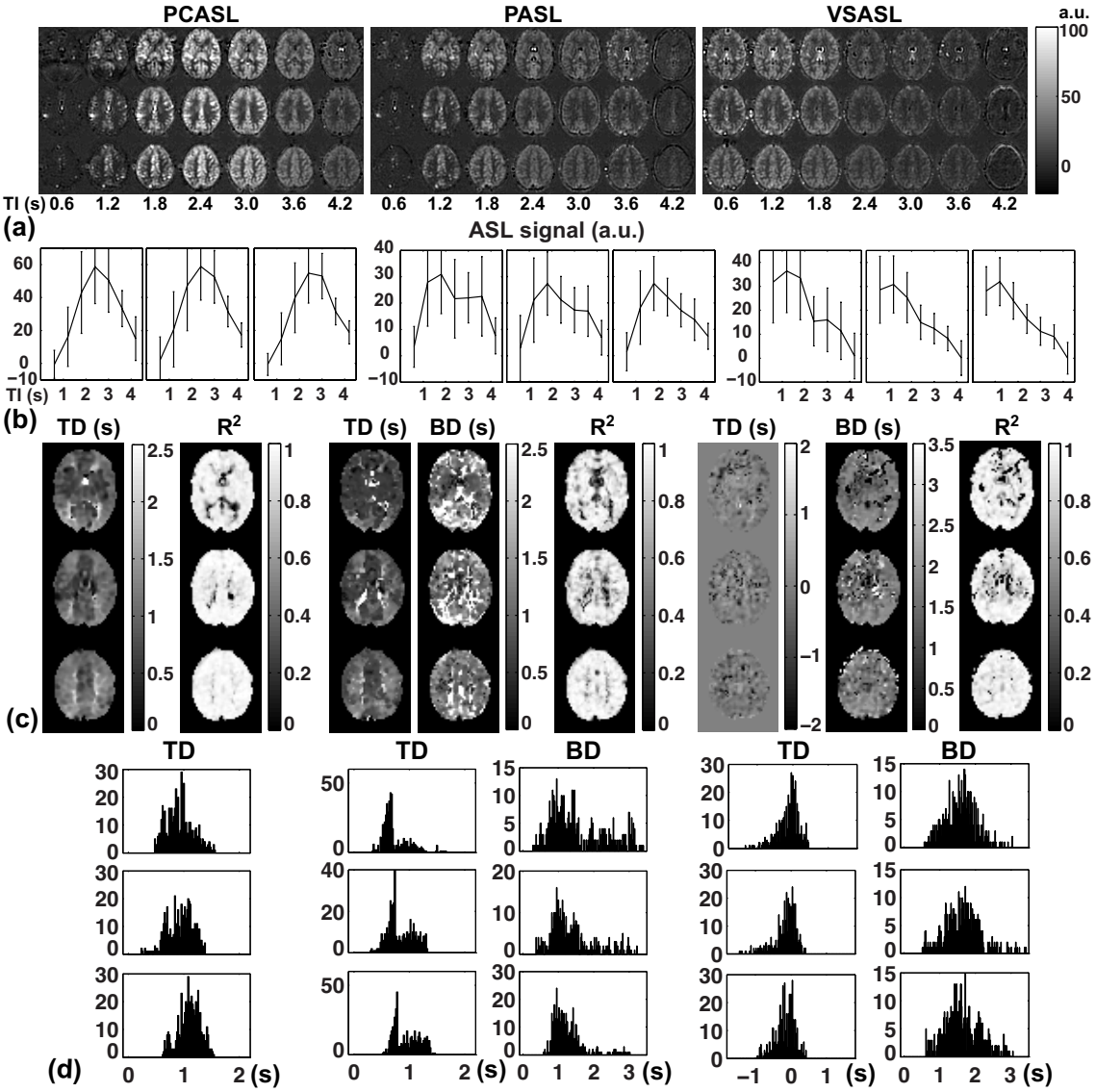

Figure 2.5. Examples of the data and fitted results from the multi-TI experiments on subject 5.

(a) ASL images acquired at different TIs using PCASL (left), PASL (middle) and VSASL (right), three slices shown at different rows; (b) averaged ASL signals in GM ROIs at different TIs; (c) fitted TD, BD and R^2 maps from (a), note the similar patterns between the TD maps using PCASL and PASL, and the nearly-zero TDs in most regions using VSASL; (d) the histograms of TDs and BDs within the GM ROIs.

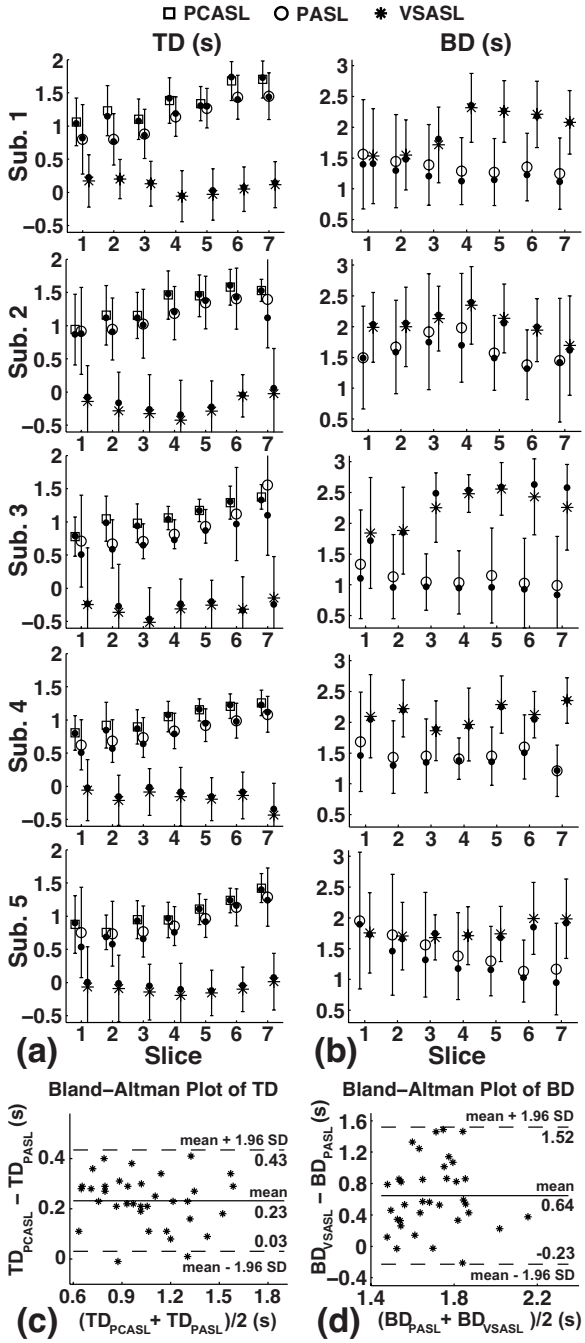

Figure 2.6. Means and STDs of TDs (a) and BDs (b) in each slice measured using PCASL, PASL and VSASL for each subject, and the Bland-Altman plots of TDs (c) and BDs (d).

Means and STDs of TDs (a) and BDs (b) in each slice measured using PCASL (square), PASL (circle) and VSASL (star) for each subject, where the dots on the error bars represent the median values; (c) the Bland-Altman plot of TDs measured with PCASL and PASL, showing the TD difference between the two; (d) the Bland-Altman plot of BDs measured with PASL and VSASL, showing BD difference between the two.

Acknowledgements

Chapter 2, in full, has been accepted for publication as it may appear in Magnetic Resonance in Medicine 2014. Guo J, Wong EC. Increased SNR Efficiency in Velocity Selective Arterial Spin Labeling using Multiple Velocity Selective Saturation Modules (mm-VSASL). Magn Reson Med 2014. doi: 10.1002/mrm.25462. The dissertation author is the primary investigator and author of this material.

References

1. Kwong KK, Belliveau JW, Chesler DA, Goldberg IE, Weisskoff RM, Poncelet BP, Kennedy DN, Hoppel BE, Cohen MS, Turner R, Cheng H-M, Brady TJ, Rosen BR. Dynamic magnetic resonance imaging of human brain activity during primary sensory stimulation. Proc Natl Acad Sci USA 1992;89: 5675-5679.

2. Williams DS, Detre JA, Leigh JS, Koretsky AP. Magnetic resonance imaging of perfusion using spin inversion of arterial water. Proc Natl Acad Sci USA 1992;89:212-216.

3. Edelman RR, Siewert B, Darby DG, Thangaraj V, Nobre AC, Mesulam MM, Warach S. Qualitative mapping of cerebral blood flow and functional localization with echo-planar MR imaging and signal targeting with alternating radio frequency (STAR) sequences: applications to MR angiography. Radiology 1994;192:513-520.

4. Kim SG. Quantification of relative cerebral blood flow change by flow-sensitive alternating inversion recovery (FAIR) technique: application to functional mapping. Magn Reson Med 1995;34(3):293-301.

5. Wong EC, Buxton RB, Frank LR. Implementation of quantitative perfusion imaging techniques for functional brain mapping using pulsed arterial spin labeling. NMR in Biomed 1997;10:237-249.

6. Dai WY, Garcia D, de Bazelaire C, Alsop DC. Continuous Flow-Driven Inversion for Arterial Spin Labeling Using Pulsed Radio Frequency and Gradient Fields. Magn Reson Med 2008;60(6):1488-1497.

7. Alsop DC, Detre JA. Reduced transit-time sensitivity in noninvasive magnetic resonance imaging of human cerebral blood flow. J Cereb Blood Flow and Metab 1996;16:1236-1249.

8. Ye FQ, Mattay VS, Jezzard P, Frank JA, Weinberger DR, McLaughlin AC. Correction for vascular artifcats in cerebral blood flow values measured by using arterial spin tagging techniques. Magn Res Med 1997;37:226-235.

9. Wong EC, Buxton RB, Frank LR. Quantitative imaging of perfusion using a single subtraction (QUIPSS and QUIPSS II). Magn Reson Med 1998;39(5):702-708.

10. Wu WC, Wang J, Detre JA, Ratcliffe SJ, Floyd TF. Transit delay and flow quantification in muscle with continuous arterial spin labeling perfusion-MRI. J Magn Reson Imaging 2008;28(2):445-452.

11. van Osch MJP, Teeuwisse WM, van Walderveen MAA, Hendrikse J, Kies DA, van Buchem MA. Can arterial spin labeling detect white matter perfusion signal? Magn Reson Med 2009;62(1):165-173.

12. Bokkers RPH, Bremmer JP, van Berckel BNM, Lammertsma AA, Hendrikse J, Pluim JPW, Kappelle LJ, Boellaard R, Klijn CJM. Arterial spin labeling perfusion MRI at multiple delay times: a correlative study with (H2O)-O-15 positron emission

tomography in patients with symptomatic carotid artery occlusion. J Cereb Blood Flow Metab 2010;30(1):222-229.

13. Yun TJ, Sohn CH, Han MH, Kang HS, Kim JE, Yoon BW, Paeng JC, Choi SH, Kim JH, Song IC, Chang KH. Effect of delayed transit time on arterial spin labeling: correlation with dynamic susceptibility contrast perfusion magnetic resonance in moyamoya disease. Invest Radiol 2013;48(11):795-802.

14. Wong EC, Liu T, Sidaros K, Frank LR, Buxton RB. Velocity selective arterial spin labeling. In Proceedings of the 10 th Annual Meeting of ISMRM; Honolulu, Hawai'i, USA. 2002. p. 621.

15. Duhamel G, de Bazelaire C, Alsop DC. Evaluation of systematic quantification errors in velocity-selective arterial spin labeling of the brain. Magn Reson Med 2003;50(1):145-153.

16. Wong EC, Cronin M, Wu W-C, Inglis B, Frank LR, Liu TT. Velocity-selective arterial spin labeling. Magn Reson Med 2006;55(6):1334-1341.

17. Wu W-C, Fernández-Seara M, Detre JA, Wehrli FW, Wang J. A theoretical and experimental investigation of the tagging efficiency of pseudocontinuous arterial spin labeling. Magn Reson Med 2007;58(5):1020-1027.

18. Guo J, Meakin JA, Jezzard P, Wong EC. An optimized design to reduce eddy current sensitivity in velocity-selective arterial spin labeling using symmetric BIR-8 pulses. Magn Reson Med 2014. DOI: 10.1002/mrm.25227.

19. Ye FQ, Frank JA, Weinberger DR, McLaughlin AC. Noise reduction in 3D perfusion imaging by attenuating the static signal in arterial spin tagging (ASSIST). Magn Reson Med 2000;44(1):92-100.

20. Zun Z, Hargreaves BA, Pauly J, Zaharchuk G. Near-contiguous spin echo imaging using matched-phase RF and its application in velocity-selective arterial spin labeling. Magn Reson Med 2014;71(6):2043-2050.

21. Cox RW. AFNI: software for analysis and visualization of functional magnetic resonance neuroimages. Comput Biomed Res 1996;29(3):162-173.

22. Kuroiwa T, Nagaoka T, Ueki M, Yamada I, Miyasaka N, Akimoto H. Different apparent diffusion coefficient: water content correlations of gray and white matter during early ischemia. Stroke 1998;29(4):859-865.

23. Le Bihan D, Turner R, Douek P, Patronas N. Diffusion MR imaging: clinical applications. AJR Am J Roentgenol 1992;159(3):591-599.

24. Buxton RB, Frank LR, Wong EC, Siewert B, Warach S, Edelman RR. A general kinetic model for quantitative perfusion imaging with arterial spin labeling. Magn Reson Med 1998;40:383-396.

25. Wong EC, Luh WM, Liu TT. Turbo ASL: Arterial Spin Labeling with Higher SNR and Temporal Resolution. Magn Reson Med 2000;44(4):511-515.

26. Wu B, Lou X, Wu X, Ma L. Intra- and interscanner reliability and reproducibility of 3D whole-brain pseudo-continuous arterial spin-labeling MR perfusion at 3T. J Magn Reson Imaging 2014;39(2):402-409.

27. Wang J, Alsop DC, Li L, Listerud J, Gonzalez-At JB, Schnall MD, Detre JA. Comparison of quantitative perfusion imaging using arterial spin labeling at 1.5 and 4.0 Tesla. Magn Reson Med 2002;48(2):242-254.

28. Gallichan D, Jezzard P. Simulating the tagging process in velocity-selective ASL. In Proceedings of the 15 th Annual Meeting of ISMRM; Berlin, Germany. 2007. p. 3488.

29. Villien M, Chipon E, Tropres I, Bouvier J, Cantin S, Chechin D, Le Bas JF, Krainik A, Warnking JM. Per-subject characterization of bolus width in pulsed arterial spin labeling using bolus turbo sampling. Magn Reson Med 2013;69(6):1677-1682.

30. Hales PW, Kawadler JM, Aylett SE, Kirkham FJ, Clark CA. Arterial spin labeling characterization of cerebral perfusion during normal maturation from late childhood into adulthood: normal 'reference range' values and their use in clinical studies. J Cereb Blood Flow Metab 2014;34(5):776-784.

31. Cavusoglu M, Pohmann R, Burger HC, Uludag K. Regional effects of magnetization dispersion on quantitative perfusion imaging for pulsed and continuous arterial spin labeling. Magn Reson Med 2013;69(2):524-530.

Supplemental Section

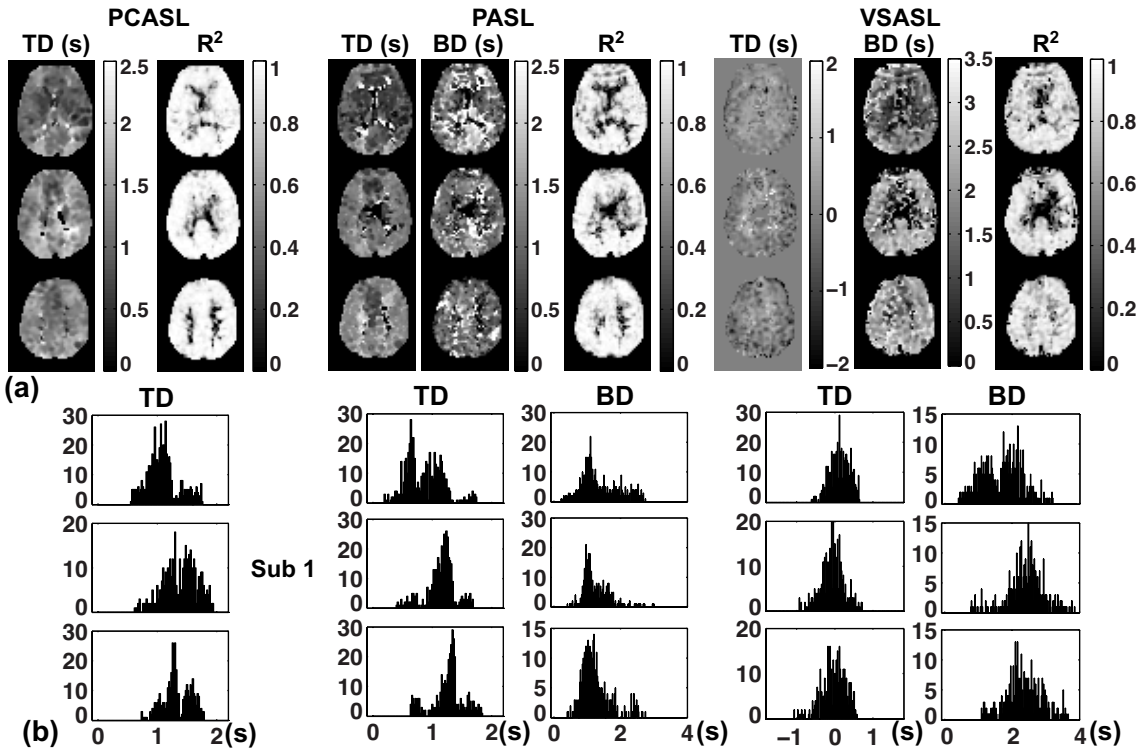

Supplementary Figure S2.7. Fitted results from the multi-TI experiments on subject 1: (a) fitted TD, BD and R^2 maps; (b) the histograms of TDs and BDs within the GM ROIs.

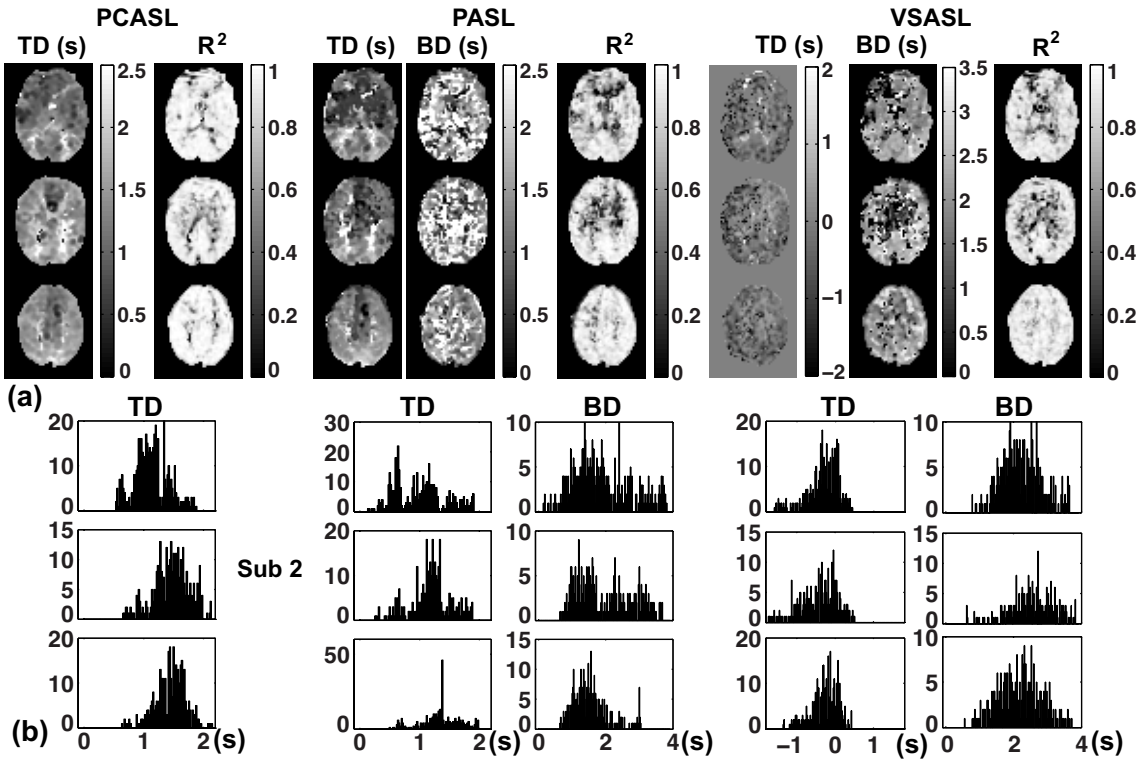

Supplementary Figure S2.8. Fitted results from the multi-TI experiments on subject 2: (a) fitted TD, BD and R^2 maps; (b) the histograms of TDs and BDs within the GM ROIs.

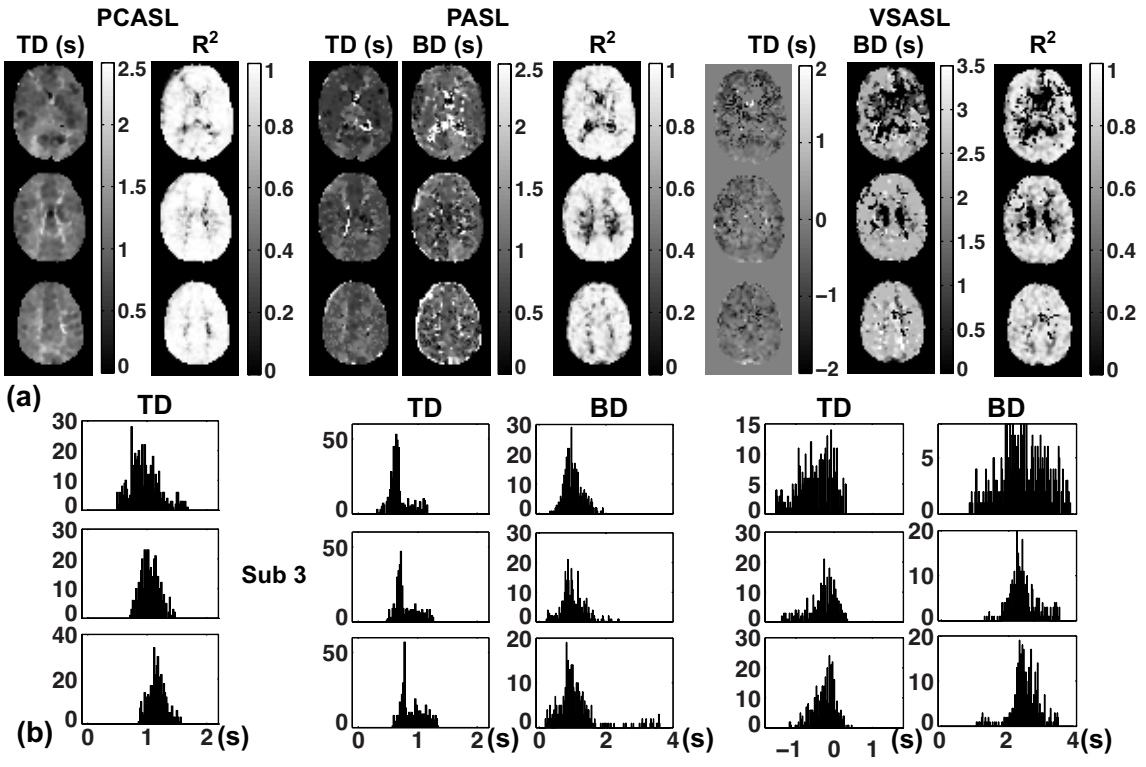

Supplementary Figure S2.9. Fitted results from the multi-TI experiments on subject 3: (a) fitted TD, BD and R^2 maps; (b) the histograms of TDs and BDs within the GM ROIs.

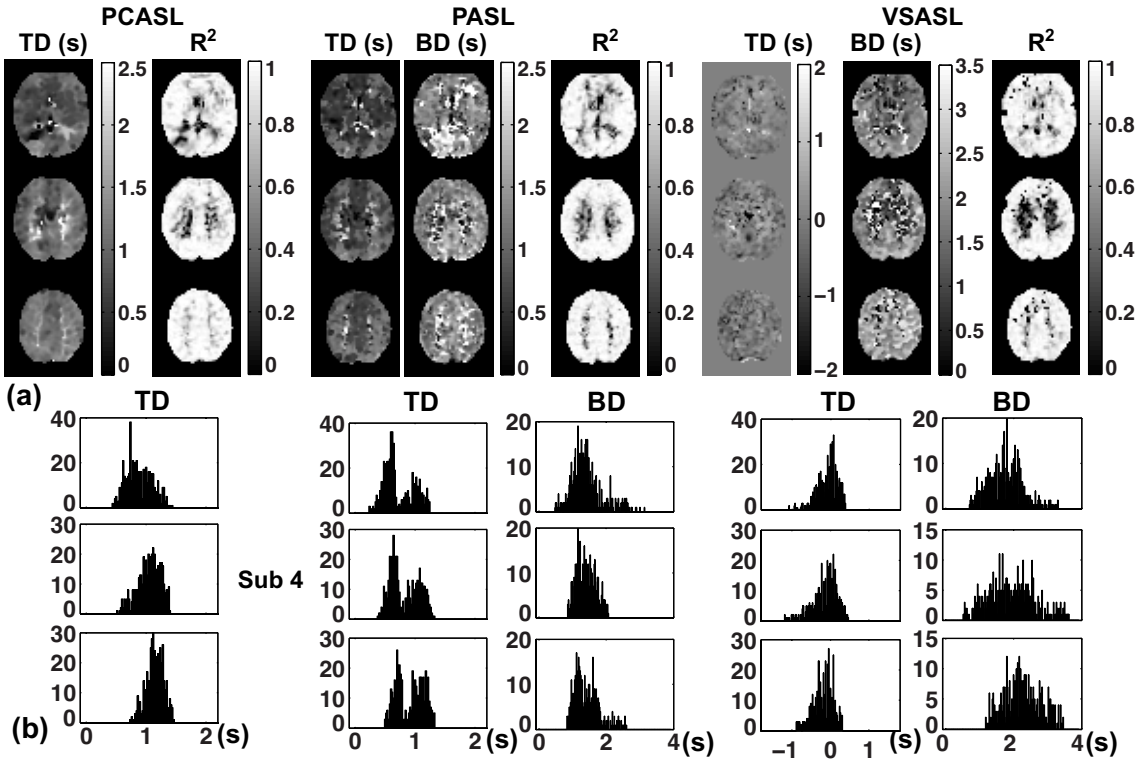

Supplementary Figure S2.10. Fitted results from the multi-TI experiments on subject 4: (a) fitted TD, BD and R^2 maps; (b) the histograms of TDs and BDs within the GM ROIs.

CHAPTER 3 : Venous Oxygenation Mapping using Velocity-Selective Excitation and Arterial Nulling (VSEAN)

Jia Guo[1]* and Eric C. Wong[2,3]

A new MRI technique to map the oxygenation of venous blood is presented. The method uses velocity-selective excitation and arterial nulling pulses, combined with phase sensitive signal detection to isolate the venous blood signal. T_2 of this signal along with a T_2–Y calibration curve yields estimates of venous oxygenation in situ. Results from phantoms and healthy human subjects under normoxic and hypoxic conditions are shown, and venous saturation levels estimated from both sagittal sinus and gray matter–based regions of interest are compared with the related techniques TRUST and QUIXOTIC. In addition, combined with an additional scan without arterial nulling pulses, the oxygen saturation level on arterial side can also be estimated. Magn Reson Med 68:1458–1471, 2012. © 2012 Wiley Periodicals, Inc.

Key words: venous oxygen saturation; arterial oxygen saturation; velocity selective excitation; T_2; VSEAN; TRUST; QUIXOTIC; magnetic resonance imaging

INTRODUCTION

After stroke, in hypoperfused but potentially salvable regions referred as the ischemic penumbra, the brain tissue is perfused at a level where its function is impaired but morphological integrity remains (1). This hemodynamic state is characterized by reduced cerebral blood flow with increased oxygen extraction fraction (OEF) to maintain vital oxygen metabolism (2). The penumbra was originally identified and defined as high OEF regions by positron emission tomography imaging in 1979 (3).

The mismatched regions from diffusion-weighted imaging and perfusion-weighted imaging are widely used as a practical surrogate to identify the penumbra that may be amenable to therapies in acute and ischemic stroke due to its relatively easy accessibility compared with positron emission tomography. However, recent studies comparing diffusion-weighted imaging/perfusion-weighted imaging with positron emission tomography (4–7) suggest that the MRI diffusion-weighted imaging-perfusion-weighted imaging mismatched regions cannot clearly differentiate true penumbra from oligemia, and the amount of tissue at risk is often overestimated from diffusion-weighted imaging-perfusion-weighted imaging mismatch. This provides motivation for returning to OEF as a better means of identifying the true penumbra.

In studies of brain function, the uncoupling of flow and oxygen metabolism gives rise to blood oxygenation level-dependent (BOLD) effect (8). However, due to the complex dynamics of blood flow, blood volume, oxygen metabolism changes, etc., researchers are looking into more direct ways of measuring cerebral metabolic rate of O_2 noninvasively, such as calibrated (9) or quantitative BOLD (qBOLD) (10–12).

Cerebral metabolic rate of O_2 can be calculated from OEF, cerebral blood flow, and arterial oxygen content (CaO_2): cerebral metabolic rate of O_2 = CaO_2 × cerebral blood flow × OEF, where OEF can be estimated from arterial and venous blood oxygenation difference. Research focusing on measurement of blood oxygenation with MRI includes: measuring the susceptibility caused by deoxygenated hemoglobin and converting it into venous oxygenation (13–15); measuring R_2' (10,11) or $\Delta R_2'$ (12) and estimating venous oxygenation through the qBOLD model (16,17); and measuring blood T_2/T_2* and converting it into oxygenation level through a model or calibration curve (18–23). These methods have their own challenges and limitations: methods based on susceptibility are limited to relatively large and straight vessels that are fully resolved by the imaging process; the qBOLD method is suitable for in situ measurement, but the model is complicated with a large number of parameters to fit (10,11), and high signal-to-noise ratio (SNR) is necessary to produce good fitting results (24), or it requires injection of intravascular contrast agent (12); methods based on T_2 measurement can be applied both in situ or in large vessels, but a good separation of blood from surrounding tissues is critical to avoid partial volume effects.

Among the T_2-based methods, experiments were successfully carried out in large vessels (18,21) and the partial volume effect was further reduced by using magnetization preparation and subtraction methods such as in TRUST (25). However, spatial information is largely lost in measurements from big vessels; and measurements from local draining veins, or in situ are desired (19,20) where the partial volume effect is most challenging.

Recently, the QUIXOTIC method introduced by Bolar et al. (26,27) provides insight into separating the blood and the tissue signal. It uses a velocity-selective (VS) spin labeling technique to separate accelerating venous

[1]Department of Bioengineering, University of California, San Diego, La Jolla, California, USA.
[2]Department of Radiology, University of California, San Diego, La Jolla, California, USA.
[3]Department of Psychiatry, University of California, San Diego, La Jolla, California, USA.

Grant sponsor: NIH; Grant number: R01 EB002096.

*Correspondence to: Jia Guo, M.S., UCSD Center for Functional MRI, 9500 Gilman Drive, MC 0677, La Jolla, CA 92093-0677. E-mail: jguo@ucsd.edu

Received 6 July 2011; revised 6 December 2011; accepted 12 December 2011.
DOI 10.1002/mrm.24145
Published online 31 January 2012 in Wiley Online Library (wileyonlinelibrary.com).

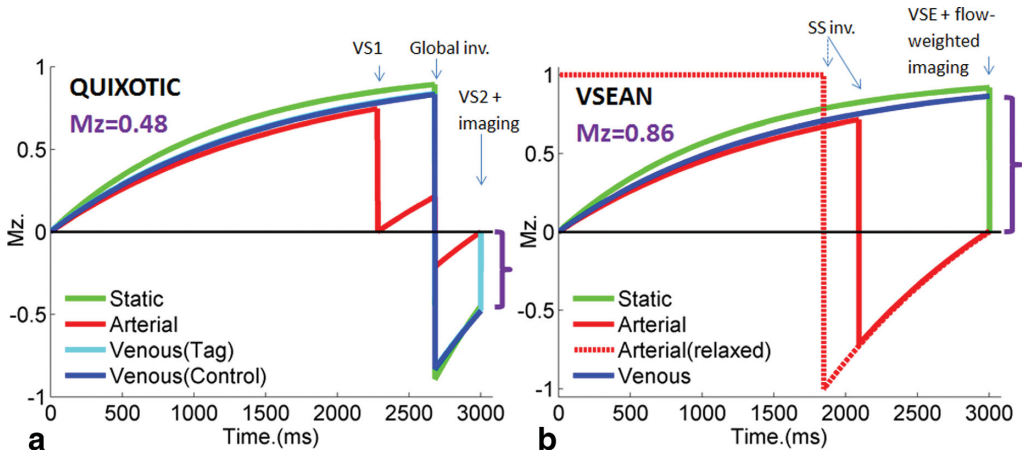

FIG. 1. Simulated magnetization evolution of venous signal using **A**) QUIXOTIC, **B**) VSEAN with $T_{1arterial} = 1664$ ms, $T_{1venous} = 1500$ ms, $T_{1tissue} = 1200$ ms, and TR = 3 s. Magnetizations indicated by purple brackets show the magnitude of the QUIXOTIC and VSEAN signals, respectively.

blood from decelerating arterial blood and static tissue. However, as the flow-sensitive gradients are turned on in the tag condition but not in the control condition, the signal difference from diffusion attenuation, especially that from cerebrospinal fluid (CSF), may contaminate the venous signal of interest (27), and there may be interference from eddy current effects. In addition, to suppress the arterial signal, a global inversion pulse is applied, which also attenuates the signal of venous blood and brain tissue, from which the venous signal originates and the subtraction scheme has relatively low temporal efficiency.

In this study, a new technique referred as VS excitation with arterial nulling (VSEAN) (28) is demonstrated to help address these issues with a focus on isolating the venous blood signal and conducting T_2 measurements. The modeling and calibration involved in converting T_2 values to blood oxygen saturation have been investigating by others (23,29–31) and are outside of the scope of this study.

THEORY

Nulling of Arterial Blood

To accurately estimate the venous oxygenation using T_2 based methods, the venous blood signal has to be separated clearly from other signal sources such as the brain tissue, CSF, and arterial blood. To remove the arterial blood signal, a slab-selective inversion pulse is applied below the imaging plane, and a delay time TI, which is set to coincide with the null point of blood longitudinal magnetization (M_z), allows for the inverted bolus of arterial blood to travel to the imaging plane. At the null point, a portion of the bolus occupies the arterial side of the vasculature and thus does not contribute to the observed signal. Another portion may enter capillaries or exchange with tissue water but would not be excited by the VS excitation (VSE, see below). A third portion may enter the venous circulation, but this portion is likely to be negligible due to fast exchange between blood and tissue water pools (32,33), and the arterial and capillary transit times. As the inversion pulse is slab-selective, the spins of tissue and venous blood in the imaging slice is unperturbed by the inversion, providing stronger venous signal relative to that of QUIXOTIC (Fig. 1).

VS Excitation

At the null point of arterial blood, a VSE pulse module is applied to excite the moving spins, without generating signal from static and slow flowing spins, including brain tissue, CSF, and the blood in capillaries. As the static tissue signal is usually much stronger than the blood signal of interest, an efficient suppression of the static tissue is critical for in situ measurements. With conventional VS pulses, the moving spins that accumulate $n\pi$ phase are tipped back to the longitudinal axis, generating a cosine-shaped M_z response with respect to velocity: $M_z = M_0\cos(\beta v)$, referred as "cos" modulation (Fig. 2), where β is the flow moment controlled by flow-weighting gradients. With an extra $\pm\pi/2$ phase added to the last tip-up portion in VS module (34), the moving spins that accumulate $2n\pi \pm \pi/2$ phase are tipped back to the longitudinal axis instead, leaving the spins that accumulate $n\pi$ phase, including the static tissue, on the transverse plane to be destroyed by a strong gradient spoiler; therefore, a sine-shaped M_z profile is generated: $M_z = M_0\sin(\beta v)$, referred as "sin" modulation. This modification can be made on VS pulses using BIR4-based (34), dual-sech (35), or hard pulses (36), and in this study, we chose BIR4-based pulses for both B_0 and B_1 insensitivity (37). The VSE pulse train and spin evolution process are illustrated in Fig. 2. We define the lowest velocity that generates $\pi/2$ phase shift as v_e for convenience.

Note that spins moving in opposite directions will accumulate phases of $2n\pi \pm \pi/2$ and will be tipped onto $+Z$ or $-Z$ axis accordingly, and their signals tend to

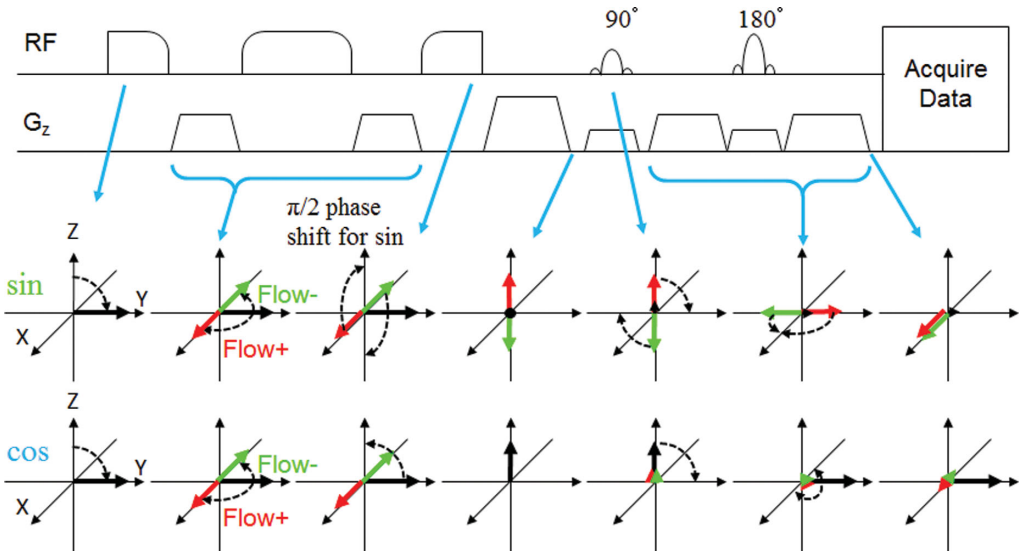

FIG. 2. Illustration of the sequence (only VSE and imaging parts) and spin evolution diagram in VSEAN. Red and green arrows depict spins that undergo $\pm\pi/2$ phase shift due to flow through velocity encoding gradients. Black arrows depict static spins. Note that for "sin" modulation, flowing spins in both directions finish aligned along +X, while under "cos" modulation, static spins are aligned along +Y. [Color figure can be viewed in the online issue, which is available at wileyonlinelibrary.com.]

cancel if they are in the same voxel. In addition, the steep velocity dependency around zero velocity makes it sensitive to slow motion. To avoid these problems, another VSE module can be applied to generate a sine-squared profile: $M_z = M_0\sin^2(\beta v)$, which has a flat response around zero velocity and should therefore be robust against slow motion. In addition, the phases of spins that are moving in opposite directions will have the same sign and thus avoid signal cancellation. However, the "$\sin^2$"excitation signal is attenuated, given a uniform velocity distribution, it generates $\pi/4 = 0.785$ of the signal with "sin" excitation.

Flow Signal Separation by Projection

Instead of applying the same "sin" modulated VSE pulse module twice, the second module is incorporated into image acquisition by adding flow-weighting gradients with the same flow moment as in the VSE preparation pulses. This reduces signal loss due to T_2 decay as well as RF power. More importantly, the $\pi/2$ phase difference between the static and moving signals with desired velocity is preserved (shown in Fig. 2), thereby allowing the separation of the moving signal from residual static signal. First, a reference phase for static tissue was estimated from a "cos" modulated signal where the static tissue signal is dominant. The "sin" modulated signal is then projected onto this phase reference axis, and separated into two components: the residual static tissue signal aligned with the reference axis, a "real" component; and the flow signal of interest with a $\pi/2$ phase shift, the "imaginary" component, which has a net $\sin^2$ dependence on velocity as described above. In principle, the reference phase images can be acquired with no VSE preparation at all; however, by using the "cos" modulated VSE pulse train, the gradients are exactly the same as in the "sin" modulated VSE pulse train, and the method should be robust against eddy current effects.

T_2 Measurement and Oxygenation Estimation

The T_2 measurement of venous blood and translation to oxygen saturation is independent of the venous signal separation process. There are several methods available: (1) T_2 preparation; (2) multiple single-echo spin-echo (SE) acquisitions; and (3) multiecho SE acquisition. The T_2 preparation method is in principle insensitive to flow effect, but the temporal efficiency and resolution is relatively low, and signal fluctuations across TR periods may introduce errors. The multiple single-echo SE method has the same issues, and it could be affected by flow effects. The multiecho SE acquisition method provides better temporal efficiency and robustness against fluctuations across TRs, but it may be affected by flow effects and stimulated echoes. In this study, we used T_2 preparation method due to its simplicity and robustness in presence of flow but continue to explore multiecho SE methods for their high temporal efficiency. The measured T_2 values were then translated to blood oxygen saturation via a T_2–Y calibration curve acquired from bovine blood sample in vitro at 3 T (29), where Y is the blood oxygen saturation.

Pulse Sequence

The layout of the VSEAN sequence is shown in Fig. 3.

Arterial Nulling

A slab-selective hyperbolic secant pulse (38) is used to invert a bolus of arterial blood below the imaging plane,

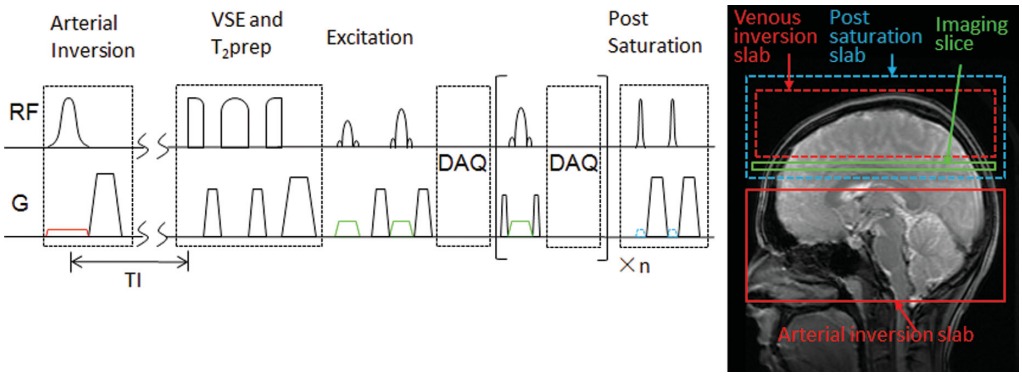

FIG. 3. VSEAN sequence diagram and tagging scheme. [Color figure can be viewed in the online issue, which is available at wileyonlinelibrary.com.]

followed by a gradient spoiler to destroy residual transverse magnetization and a delay time TI. In this study, we used PICORE-type (39) preparation: a slab selective pulse is referred to as an arterial-nulling (AN) experiment; and a nonselective off-resonance pulse (the PICORE control) is referred to as a non-AN (non-AN) experiment. The latter compensates for magnetization transfer and slice profile effects and allows for separation of arterial and venous components. If one wants to reduce the contribution from the venous blood above the imaging slice, preparations such as EPISTAR (40) or FAIR (41,42) can be used.

VS Excitation

A BIR4-based VSE pulse module (34) is applied at the null point of arterial blood, with flow-weighting gradients between the RF pulses. The parameters (37) of the BIR-4 pulse are: pulse length 6ms; $\omega_{max} = 42.52$ KHz; zeta = 43.58; $\tan(\kappa) = 69.65$; and two gaps of 1–8 ms follow the gradients to reduce possible interference between eddy currents and RF pulses. The last BIR1 subpulse has 0 or $\pm\ \pi/2$ phase shift in addition to the original phase to generate "cos" or "sin" modulation accordingly. In principle, either $+\pi/2$ or $-\pi/2$ phase shift should work. However, in our implementation, $-\pi/2$ phase shift gave better static spin suppression and was used in this study.

T_2 Preparation (T_2prep)

We modified the original BIR4-based T_2 preparation pulses (43) by merging it into the VSE module: two controllable gaps were inserted between the first and last BIR1 subpulses and the flow-weighting gradient to generate desired T_2-weightings without perturbing the flow-weighting gradients. The excitation pulses are applied immediately after the spoilers at the end of this VSE/T_2prep module to minimize the T_1 recovery of the static tissue signal. This VSE/T_2prep combined design also reduces RF power. The scan repetition time was fixed in this study, so the spins experienced different T_1 recovery times at different effective echo times (eTEs). The error from neglecting this effect was found by simulation to be less than 0.6%.

Image Acquisition

A slice-selective excitation pulse is followed by refocusing pulses to generate spin echoes. In this study, we used sinc and dual-sech refocusing pulses in different experiments, the former for its short echo time and the latter for its B_1 insensitivity and better slice profile (44). The flow-weighting gradients are around the first refocusing pulse.

Postsaturation Pulses

After the image acquisition, a set of saturation pulses are applied to reset the spins for the next TR, either locally or "globally." In principle, a global nonselective saturation pulse could reset the magnetization of all spins, thus ensuring a well-characterized spin history, independent of inflow into the inversion slab. However, in a typical whole body scanner, the transmit RF coil extends only to the upper part of the torso, and our measurements indicate that after nonselective saturation, unperturbed blood reaches the brain in ~1 s. Thus, given the timing of our pulse sequence, the use of nonselective saturation would confound the magnetization history of arterial blood due to mixing of saturated and fully relaxed blood, leaving the null point poorly defined. In this study, the saturation pulses were applied locally, above the arterial inversion slab, including the imaging slice and the brain tissue above. By applying the saturation pulses locally, fully relaxed arterial blood flows into the inversion slab. If the inversion slab is refreshed with relaxed blood prior to inversion, this provides a well-defined null point and also allows for the use of a longer TI, in turn allowing more time for arterial filling by the inverted blood. This condition is met if the inversion slab is refreshed in a time (TR-TI), which in our experiment is greater than 1.5 s, and we believe that this condition is well met in our experiments. Figure 1b shows the arterial magnetization for blood that is saturated (solid red) and relaxes (dashed red) prior to inversion. Our experiment follows the dashed red curve, while for

Table 1
T_2 Values Measured in Flow Phantom Experiments

T_2 (ms)	ROI	1	2	3	4	5
Stationary	Average and fit	245.2	243.9	234.7	166.4	239.5
	ROI mean ± SD	245.5 ± 5.2	243.5 ± 4.0	233.3 ± 3.7	166.1 ± 3.1	239.2 ± 3.8
Circulating	Average and fit	239.5	244.7	219.5	156.8	241.1
	ROI mean ± SD	238.6 ± 5.1	242.5 ± 4.9	218.3 ± 8.5	156.8 ± 3.5	241.0 ± 3.9
Circulating w/VSE	Average and fit	233.4	226.3	215.5	N/A	N/A
	ROI mean ± SD	233.4 ± 9.4	226.4 ± 10.0	216.2 ± 10.6	N/A	N/A

nonselective saturation the net magnetization is somewhere between the red solid and dashed curves.

Experimental Setup, Data Collection, and Processing

All experiments were performed on a GE Discovery MR750 3-T system, using a commercial 8-channel RF coil. Images were complex-reconstructed offline with homemade software and processed in Matlab (Mathworks, Inc.). For VSEAN data, the signal projection procedure was applied individually for each channel after complex-reconstruction and then combined together: the phase associated with the coil itself is the same for "cos" and "sin" modulated data and is cancelled after the projection process, so the extracted signals from different coils are in phase with signs, allowing directly summing up together weighted by the coil sensitivities estimated from the "cos" modulated data, which has high SNR. The noise is kept zero-mean since the sign of signal is preserved in combination, in contrast with the sum of square method. Sum of square reconstruction was used in QUIXOTIC and TRUST data analysis, where the nonzero means of the noise were removed after subtraction.

When analyzing regions of interest (ROIs), the T_2 values were calculated pixel-wise. Noisy pixels yielding $T_2 < 0$, or $T_2 > 300$ ms in the flow phantom experiments, and $T_2 < 0$ or $T_2 > 150$ ms in human experiments were discarded. The mean and standard deviation were then calculated from all the T_2 values. This was referred as "ROI mean ± standard deviation" in Table 1 and used to calculate the mean ROI T_2 values in Table 2. The oxygen saturation after T_2-Y conversion was also reported. In the flow phantom experiments, a single T_2 value was also fitted after averaging the signal intensities first in each ROI, for the sample should have identical T_2 value in each ROI. This is referred as "average and fit" in Table 1.

Experiments Using a Stationary Phantom

The VSE pulse modules were first tested on a stationary gel phantom. The imaging parameters were: FOV = 200 × 200 mm^2, slice thickness = 8 mm, resolution 64 × 64, single-slice single SE with spatial-spectral excitation and a sinc 180° refocusing pulse, single-shot spiral readout, v_e set to 2 cm/s in the slice-select direction, TE/TR= 18 ms/1 s, two dummy scans followed by 10 acquisitions, the first 4 were "cos" modulated and the rest "sin" modulated, scan time 12 s. For comparison, QUIXOTIC data were also collected: the imaging and preparation pulse parameters were the same, no global inversion pulse, only the VS2 module (26) right before the imaging was applied.

The images were averaged across TRs first. For VSEAN data, the residual "static" and the "moving" signals were extracted as "real" and "imaginary" components accordingly; for QUIXOTIC data, the "moving" signal was calculated from subtraction between the "control" and "tag" images.

Experiments Using a Rotating Phantom

A spherical gel phantom was fixed in a cylindrical plastic case connected by a long rod to a stepper motor in the console room, which can induce controlled rotation about the scanner axis. After a localizer scan, the diameter (D) of the phantom was measured, and the maximum velocity on the edge of the phantom to be $v_{max} = 8$ cm/s, giving an in-plane rotating velocity at radius r of $v(r) = 2 \times v_{max} \times r/D$.

The VSE pulse train was tested with global postsaturation and imaging parameters: axial scan, FOV = 200 × 200 mm^2, 8-mm slice thickness, single-slice single SE with sinc 90° and 180° pulses, TE/TR = 12 ms/3 s, 64 × 64 resolution, single-shot spiral readout, flow-weighting gradients along the A/P direction with $v_e = 2$ cm/s, 12 repetitions, and 36 s for each experiments. For the following six experiments, the phantom was stationary in experiments 1 and 2, and rotating through experiments 3–6: (1) no VSE, no flow-weighting gradients in imaging; (2) VSE with "cos" modulation, with flow-weighting gradients in imaging; (3) no VSE, with flow-weighting gradients in imaging; (4) VSE with "cos" modulation, no flow-weighting gradients in imaging; (5) VSE with "sin" modulation, no flow-weighting gradients in imaging; (6) VSE with "sin" modulation, with flow-weighting gradients in imaging.

The images in experiment 1 were used as a phase reference for experiment 3, and those in experiment 2 for experiments 4–6. The magnitude of the images was normalized to their reference scans, and the "static" and "moving" signals were extracted as "real" and "imaginary" components. The data along a horizontal line passing through the center of the phantom gave the VSE profile.

Experiments Using a Flow Phantom

In this experiment, copper sulfate doped water was circulated through a set of plastic hoses connected to a dialyzer (Optiflux F160NR, Fresenius Medical Care), with the flow rate adjusted by a valve. A "U"-loop section of the hose was fixed on top of the dialyzer and a

Table 2
T_2 Values and Oxygenation Levels Measured Under Normoxia

			VSEAN					QUIXOTIC				TRUST	
			GM/WB		SS		GM/WB		SS		SS	
Sub.	Sex	ROI	Sig. (%)	T_2 (ms)	O_2 (%)	T_2 (ms)	O_2 (%)	T_2 (ms)	O_2 (%)	T_2 (ms)	O_2 (%)	T_2 (ms)	O_2 (%)
1	M	A	0.29 ± 0.15	60.4 ± 25.0	78.3 ± 15.1								
		A&V	0.77 ± 0.57	39.1 ± 14.8	65.9 ± 13.2	43.4 ± 6.8	71.9 ± 5.0						
		V	0.48 ± 0.53	33.1 ± 18.3	57.1 ± 19.1	41.5 ± 8.0	70.3 ± 5.9	66.2 ± 29.3	80.9 ± 14.3	40.5 ± 13.6	68.4 ± 8.6		
2	M	A	0.23 ± 0.24	61.6 ± 31.3	77.2 ± 18.2								
		A&V	1.43 ± 1.14	42.4 ± 13.5	69.0 ± 12.9	41.2 ± 5.7	70.4 ± 4.7						
		V	1.20 ± 0.99	36.5 ± 14.0	62.6 ± 16.4	37.5 ± 3.8	67.5 ± 3.4	57.2 ± 27.1	76.4 ± 15.0	43.4 ± 13.2	71.3 ± 6.1		
3	F	A	0.27 ± 0.16	41.4 ± 21.9	64.5 ± 19.9								
		A&V	1.06 ± 0.61	37.1 ± 13.3	64.4 ± 12.6	42.6 ± 13.5	70.0 ± 8.9						
		V	0.79 ± 0.56	36.6 ± 16.4	62.2 ± 17.1	38.8 ± 12.6	66.5 ± 10.8	56.3 ± 28.4	74.9 ± 17.1	35.6 ± 9.7	64.6 ± 7.7	34.4 ± 9.6	63.2 ± 8.8
4	M	A	0.17 ± 0.20	59.2 ± 32.7	74.4 ± 21.4								
		A&V	1.06 ± 0.78	41.1 ± 17.4	66.6 ± 15.4	38.4 ± 7.8	67.6 ± 6.3						
		V	0.89 ± 0.81	35.0 ± 16.1	60.0 ± 18.0	34.9 ± 6.4	64.4 ± 6.5	58.1 ± 29.6	75.3 ± 18.7	34.3 ± 9.9	62.6 ± 11.0	36.8 ± 9.7	64.8 ± 12.3
Mean		A		55.7 ± 9.6									
T_2 (ms)		V		35.3 ± 1.6		37.6 ± 2.8		59.4 ± 4.6*		38.5 ± 4.2		35.6 ± 1.7	

VSEAN signal intensities in GM are also listed. All numbers are expressed as mean ± SD.
*T_2 values measured from GM by QUIXOTIC are significantly higher than that by VSEAN ($P = 0.004$).

syringe filled with the same solution without flow was also in the FOV. A cross-section image is shown in Fig. 6a, with ROIs shown in Fig. 6g: ROIs 1 and 2 the big hose, ROI 3 the small hose, ROI 4 the dialyzer, and ROI 5 the syringe. T_2 maps of the phantom were acquired using a BIR4 T_2 preparation pulse under both stationary and circulating conditions; and two sets of VSEAN data were also collected: (1) no flow with "cos" modulated VSE/T_2prep pulse as a reference scan, six repetitions, and 12 s each; and (2) flowing water with "sin" modulated VSE/T_2prep pulse, 18 repetitions, and 36 s each. The imaging parameters were: FOV = 100 mm × 100 mm, slice thickness = 8 mm, single-slice single echo SE with spatial-spectral excitation and a sinc 180° refocusing pulse, spiral readout with resolution 64 × 64, TE/TR = 18 ms/2 s, three eTEs 10/30/70 ms in BIR4 T_2prep experiments, 30/50/90 ms in VSE/T_2prep experiments, v_e = 2 cm/s in the slice-select direction. A velocity map in the same plane was collected using a conventional phase contrast sequence with VENC = 8 cm/s.

The velocity map of the phantom was calculated from the phase difference map and then masked by the magnitude image. We noticed that the measured average velocity in the static syringe was slightly nonzero, presumably due to gradient imperfections, and this value was subtracted from the entire velocity map. Predicted maps of the real and imaginary components of "sin" modulated signal were calculated as follows. The magnitude image of the "cos" modulated signal (stationary) was oversampled and registered to the velocity map, then multiplied with the theoretical velocity excitation profile to give the "real" $(\sin(\pi^* v/4)\cos(\pi^* v/4))$ and "imaginary" $(\sin^2(\pi^* v/4))$ components. T_2 maps of the flow phantom were calculated by exponential fitting, and average T_2 values were calculated for the ROIs.

Healthy Human Volunteer Experiments Under Normoxia

Five healthy human volunteers (four males, one female, age 25–47) were scanned under an IRB-approved protocol. The imaging parameters were: FOV = 200 mm × 200 mm, slice thickness = 8 mm, single-slice SE with spatial-spectral excitation and two slice-selective hyperbolic secant refocusing pulses, single-shot spiral readout with original resolution 32 × 32, regridded to 64 × 64, TR/TE = 3 s/28 ms, VSE/T_2prep with eTEs 20/40/80 ms, v_e = 2 cm/s in the slice-select direction, arterial inversion slab thickness 200 mm, 25 mm below the imaging plane, TI = 1150 ms assuming T_{1b} = 1664 ms (45), slice-selective postsaturation pulses, two dummy scans followed by 126 acquisitions including six "cos" modulated reference scans at the beginning, scan time 6 min 18 s. VSEAN data with AN and non-AN were collected on each subject. Gray matter (GM) masks were acquired using double-inversion prepared sequence with the same resolution except for subject 1, for whom this image was not acquired, and a GM mask was calculated from non-AN VSEAN images.

Arterial components were extracted by subtracting the AN data from the non-AN data, and T_2 maps from arterial-only, arterial-and-venous, and venous-only data were calculated. Two ROIs were chosen to analyze: (1) GM

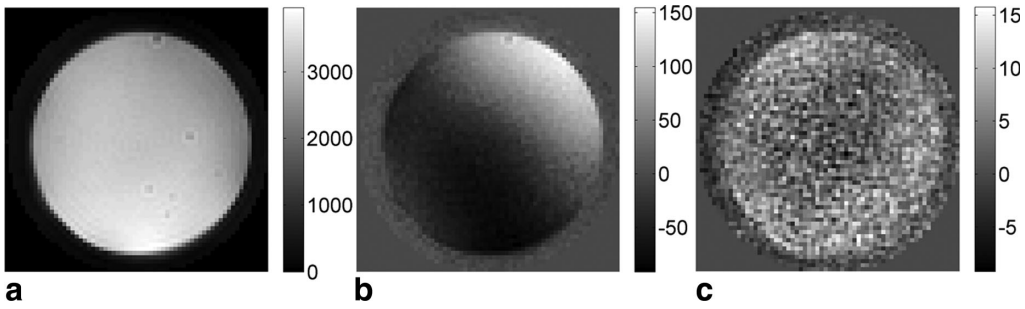

FIG. 4. VSE data collected on a stationary gel phantom (a.u.). **a**: "cos" modulated, magnitude image; **b**: "sin" modulated, "real" component; **c**: "sin" modulated, "imaginary" component. The root mean square (RMS) signal in the "sin" modulated imaginary component is 0.2% of the fully relaxed signal.

and (2) sagittal sinus (SS), shown in Fig. 8c. T_2 values in the ROIs were converted into blood oxygenation levels via a T_2-Y calibration model at 3 T provided in Ref. 29: T_2^{-1} (s^{-1}) = 8.3 + 33.6 × (1 − Y) + 71.9 × (1 − Y)^2, where a similar T_2 measurement was performed by varying the echo times without changing the number of RF pulses and a hematocrit (Hct) of 0.44 was assumed for all subjects.

For comparison, QUIXOTIC data were collected on subjects 1, 2, 3, and 4, and TRUST data on subjects 3 and 4. The imaging parameters were the same as in VSEAN unless noted otherwise. The QUIXOTIC data acquired on subject 1 had initial resolution 48 × 48 instead of 32 × 32. Other tagging parameters are listed below.

QUIXOTIC

Two VS preparation modules were used, with v_{cut} = 2 cm/s in the slice-select direction. The first one was 722 ms before image acquisition, followed by a global inversion pulse 400 ms later, and the second VS module was immediately before the imaging excitation pulse (26,27). The second VS module was a VSE/T_2prep module, the flow-weighting gradients were turned on and off under tag and control conditions accordingly, the same eTEs were used as in VSEAN experiments, 120 acquisitions after two dummy scans, scan time 6 min 6 s.

TRUST

The thickness of inversion slab was set to 50 mm, 25 mm above the imaging plane, with TI = 1200 ms (25). A BIR4-based T_2 preparation module was used with the same eTEs, TR/TE = 8 s /26 ms, and 36 repetitions were acquired without dummy acquisitions, scan time 4 min 48 s.

QUIXOTIC and TRUST images were obtained by subtracting the "tag" and "control" images after averaging. T_2 values were then calculated the same way as in VSEAN. GM and SS ROI analyses were performed on QUIXOTIC data, and SS on TRUST.

Venous T_2 Measurements Under Hypoxia

Subjects 2 and 5 were scanned using VSEAN during normoxia and during a hypoxia challenge. Arterial O_2 saturation levels were monitored by a pulse oximeter on subject's finger (MRI 3150 Physiological Monitor, Invivo Research) throughout the experiments. During the normoxia scans, normal air (20.9% O_2, rest N_2) was delivered to subjects through a mask. The gas was switched to a hypoxic mixture (12.4% O_2, rest N_2) from a rubber balloon during the hypoxia scans. The hypoxia VSEAN scans started 10–15 min after switching the gas when the arterial O_2 saturation level stabilized below 90%. A non-AN scan was performed first, followed by AN scan. The imaging parameters were the same as in other VSEAN scans, except that the repetitions were 96, 4 min 48 s each, for subject 5, including six "cos" modulated repetitions.

RESULTS

Experiments Using a Stationary Phantom

As shown in Fig. 4, the signal from stationary spins was suppressed after "sin" modulated VSE. The residual static signal ("real" component) was neatly separated from the moving signal ("imaginary" component) after projection, which was kept around the noise level. The residual signal in QUIXOTIC (not shown here) after subtraction was well above noise level. However, after increasing the gaps (approximately 6–8 ms) after the flow-weighting gradients, the residuals were reduced to similar level as in the VSE experiment after T_2 decay correction. This suggested that the subtraction error observed in the QUIXOTIC experiment could be mainly from eddy current effects. The error due to diffusion attenuation was not observed in QUIXOTIC experiment on this phantom. In comparison, increasing the gaps in the VSE pulse train only improved the residual static tissue signal suppression before projection; and no effect was observed on the "imaginary" component after projection.

Experiments Using a Rotating Phantom

Measured velocity excitation properties of different components in the VSE pulse train are shown in Fig. 5. Flow

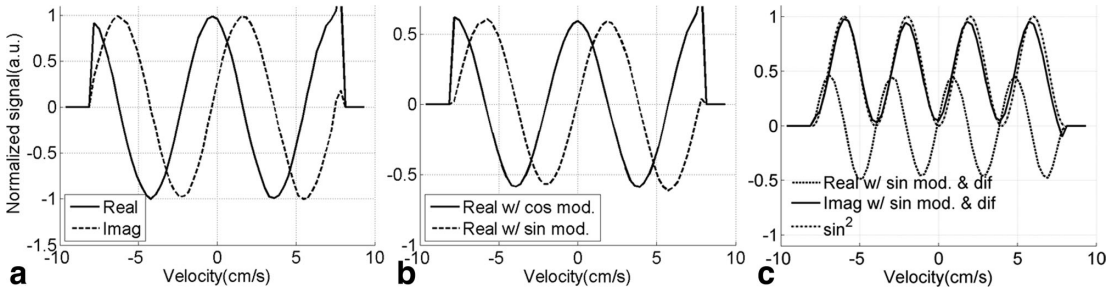

FIG. 5. Velocity excitation profile measured in a rotating gel phantom. **a**: Real and imaginary components with flow weighting in imaging only; **b**: Real components with only "cos" modulation and only "sin" modulation, the imaginary components of both "cos" and "sin" modulation were close to zero and are not shown here; **c**: Real and imaginary components with "sin" modulation and flow weighting in imaging, resulting in a $\sin^2$ dependence for the imaginary component, which closely matched an ideal $\sin^2$ curve (see text).

weighting in the imaging sequence alone (Fig. 5a) and a VSE module alone (Fig. 5b) both gave sinusoidal and cosinusoidal components as expected. A clear $\sin^2$-shaped velocity excitation profile was observed in the imaginary component using "sin" modulated VSE and flow-weighting gradients in imaging, matched well with the prediction (Fig. 5c) and the excitation response was flat and close to zero at zero velocity as expected.

Experiments Using a Flow Phantom

A velocity map, VSEAN images, and T_2 maps are shown in Fig. 6. The maximal velocities in ROIs 1, 2, and 3 were 2.1, −2.1, and 7.5 cm/s, respectively, and the averaged velocity in ROI = 4 was −0.18 cm/s. As shown in Fig. 6e and f, the actually measured signal from static spins in ROI = 5 was almost completely suppressed by the "sin" modulated VSE pulse train, while the fast, intermediate, and slow flows were preserved, and they matched very well with the predicted signal patterns shown in Fig. 6b and c, which were calculated from the magnitude image Fig. 6a and the predicted velocity excitation profile generated from the velocity map Fig. 6d. These also matched well with the velocity excitation profile measured in the rotating phantom experiment. The results of ROI analysis are summarized in Table 1.

The T_2 values measured in high SNR ROIs were similar; however, slightly decreased T_2 values (<10%) were observed in the fast flow ROI while circulating, presumably due to unstable flow there. And the T_2 fitting in ROI = 4 was noisy due to low SNR.

Healthy Human Volunteer Experiments Under Normoxia

Figure 7 shows arterial-and-venous weighted, venous weighted and arterial weighted VSEAN images acquired from subject 1 at different eTEs, normalized by the averaged brain tissue signal estimated from reference scans and expressed as percentage maps, as well as T_2 maps calculated from each data set. VSEAN, QUIXOTIC, and TRUST data at the lowest eTE from subjects 1–4 are shown in Fig. 8a, b, and f, respectively. The representative ROIs are shown in Fig. 8d, the ROI analysis of signal intensities and T_2 values are summarized in Table 2, and also shown in Fig. 8e, and a pixel-wise comparison on the GM T_2 values measured by VSEAN and QUIXOTIC for each subject were shown as scatter plots in Fig. 8c.

For the VSEAN data, the arterial component was weaker than venous component on all scanned volunteers. Given the velocity sensitivity range (v_e = 2 cm/s) in this study, and the fact that the arterial blood decelerates quickly from relatively high velocities while the venous blood slowly accelerates to moderate velocities, it is possible that less arterial blood distributes within this velocity range than the venous blood; another possibility could be that some of the inverted arterial blood was replaced by fresh blood in this velocity range; therefore, only a subset of available arterial signal was detected, or a combination of both.

As shown in Fig. 8, the VSEAN signal was higher than the QUIXOTIC signal, especially on subject 4. In addition to the higher SNR efficiency in theory (Fig. 1), another reason could be that QUIXOTIC and VSEAN measured different populations of venous blood: QUIXOTIC assumes that the venous blood is accelerating, thus it detects only the portion that accelerates above v_{cut} (2 cm/s), while VSEAN measures venous blood mainly in the velocity range 0–4 cm/s. So, it is possible that the QUIXOTIC sampled only a portion of the venous blood that VSEAN captured.

It is notable that the VSEAN signals (arterial and venous) are related to but not proportional to cerebral blood volumes (CBVs), because these signals are modulated by a $\sin^2$-shaped velocity excitation profile. The arterial VSEAN signal may be further reduced by incomplete inversion of the arterial blood pool. Nevertheless, these signals provide rough estimates of the arterial, venous, and total CBVs, and they are in the expected range, less than 3% in the brain tissue (Figs. 7 and 8 and Table 2).

To quantitatively assess if the mean venous T_2 values in SS across subjects are consistent using VSEAN, QUIXOTIC, and TRUST, a one-way ANOVA was performed. No significant difference was found (P = 0.61, F = 0.52, doff = 2, total sample size = 10, post-hoc power > 0.73 using the statistical software package G*power 3.1.3 (46)). However, the T_2 values from GM using QUIXOTIC were higher than all other measurements including

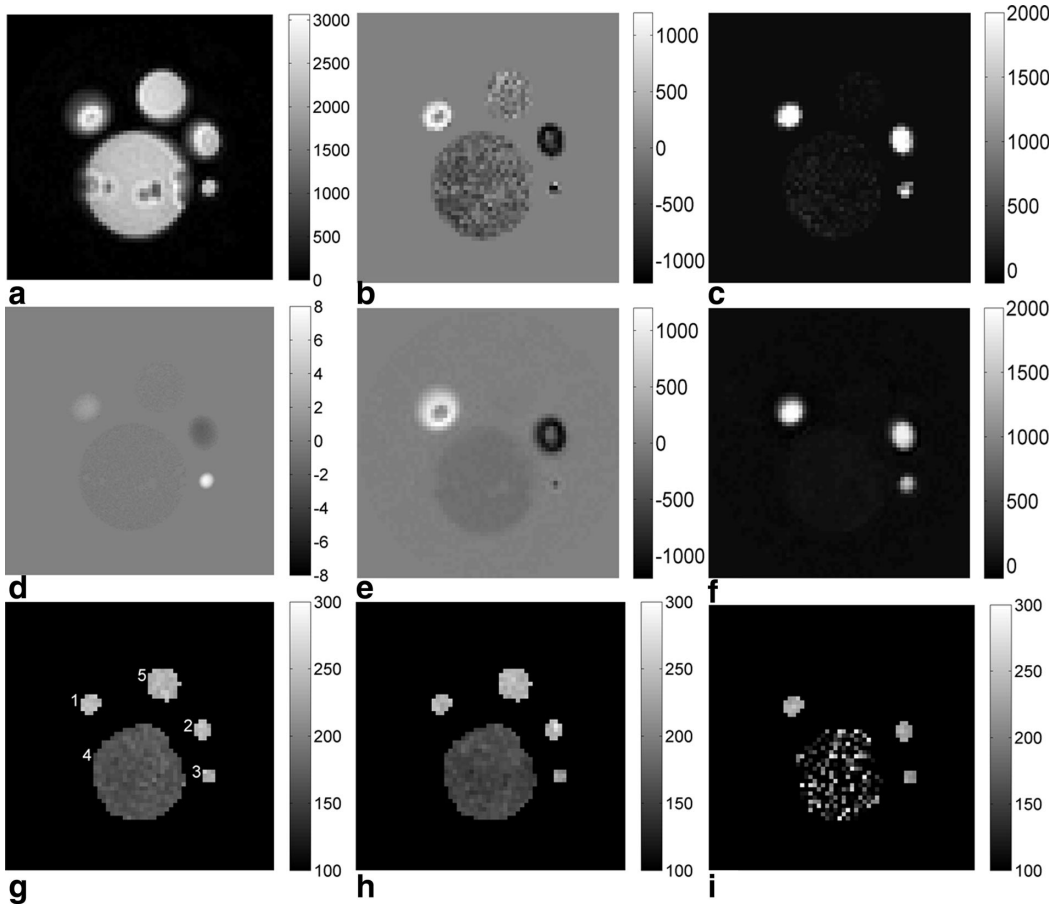

FIG. 6. **a:** "cos" modulated reference image (magnitude, a.u.); **b**: Predicted (from **a** and **d**) "sin" modulated real components (a.u.); **c**: Predicted "sin" modulated, imaginary components (a.u.); note that the noise outside the phantom was removed due to the mask used on velocity map; **d**: Velocity map (cm/s); **e**: Measured "sin" modulated real components (a.u.); **f**: Measured "sin" modulated, imaginary components (a.u.); note that this component is rectified across positive and negative flow directions, as expected for a $\sin^2$ velocity dependence, and both the real and imaginary components closely matched the predicted signal pattern; **g**: T_2 maps when the phantom was stationary (ms), ROIs labeled; **h**: T_2 maps when the phantom was circulating (ms); **i**: T_2 maps measured with VSE (ms).

QUIXOTIC in SS, a same trend was found when comparing QUIXOTIC in GM and TRUST in SS in Ref. 27. A paired *t*-test was performed on the mean GM venous T_2 values across subjects measured by VSEAN and QUIXOTIC, and showed that T_2 values measured by QUIXOTIC were significantly higher than those by VSEAN ($t(3) = 7.87$, $P = 0.004$, post hoc power > 0.78). The higher T_2 values in the GM ROI by QUIXOTIC could be due to CSF contamination from diffusion attenuation, or subtraction error from eddy current effects for the reasons discussed above.

For VSEAN measurement, the T_2 values calculated from the arterial, arterial and venous, venous components followed a descending trend as expected. The mean venous T_2 values measured in the SS were close to those measured in the GM ROI, except in subject 1 where the mean T_2 value in the SS ROI was higher.

The venous T_2 value measured in the GM/whole brain was 35.3 ± 1.6ms (mean ± SD) and 37.6 ± 2.8ms in the SS across subjects 1–4 under normal condition. Although the T_2 fitting of the arterial components was noisier than that of the venous components due to lower SNR, higher arterial T_2 values (55.7 ± 9.6ms) were observed with a difference of 20.4 ms on the group means, except that on subject 3 where a lower than group mean arterial T_2 value was observed.

The mean oxygenation levels measured in the SS were 67.2 ± 2.5% ($n = 4$) by VSEAN, 66.7 ± 3.9% ($n = 4$) by QUIXOTIC, and 64.0 ± 1.1% ($n = 2$) by TRUST, which are consistent with another study using TRUST [64.8 ± 6.3% ($n = 24$) (25)]. The mean oxygenation level measured in the GM was 60.5 ± 2.5% ($n = 4$) by VSEAN, which is comparable with literature values: (1) 61.7 ± 5.3% using qBOLD ($n = 9$, GM and WM, calculated

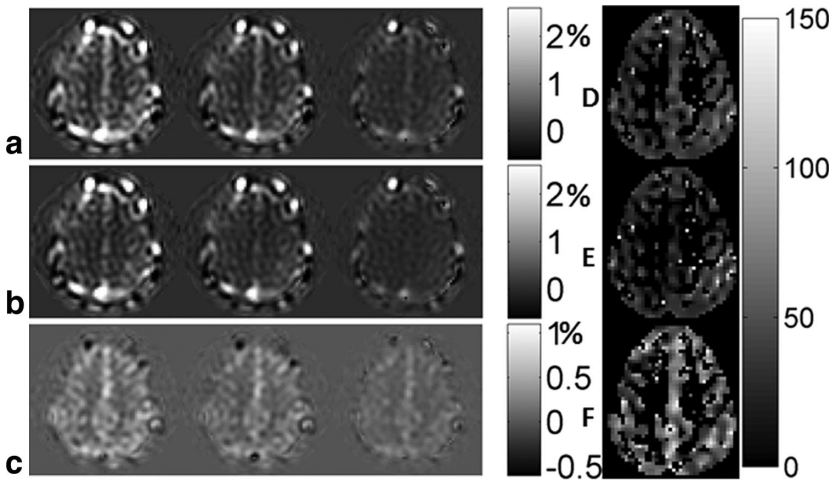

FIG. 7. **a**: Non-AN VSEAN images at different eTEs (arterial and venous, normalized and windowed from −0.5 to 2.5%, see text); **b**: AN VSEAN images (venous, the display range from −0.5 to 2.5%); **c**: difference images of a–b, (arterial, −0.5 to 1.1%); **d**: T_2 map calculated from a (arterial and venous, ms); **e**: T_2 map calculated from b (venous, ms); **f**: T_2 map calculated from c (arterial, ms).

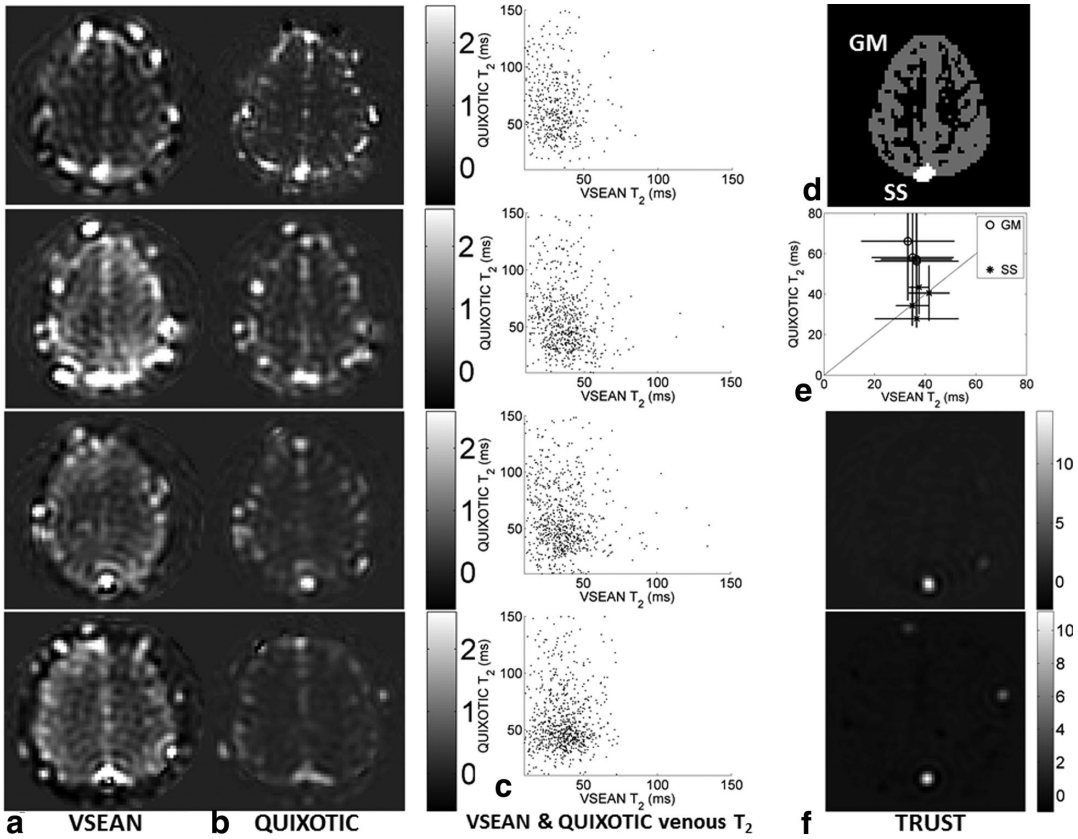

FIG. 8. **a**: VSEAN, **b**: QUIXOTIC, and **f**: TRUST images at eTE = 20 ms, acquired under normoxic conditions on subjects 1–4 (top to bottom, TRUST data only on subjects 3 and 4); **c**: Scatter plots showing the pixel-wise comparison of T_2s measured from Gray Matter ROI for each subject; **d**: representative ROIs of Gray Matter and Sagittal Sinus used in analysis; **e**: comparison of means and standard deviations of T_2 values measured using VSEAN and QUIXOTIC with the unity line shown diagonally, and the standard deviations of VSEAN T_2 shown horizontally and QUIXOTIC vertically.

Table 3
T_2 Values and Oxygenation Levels Measured Under Normoxic and Hypoxic Conditions

		Normoxia		Hypoxia	
		SS		SS	
Subject Sex	ROI	T_2 (ms)	O_2 (%)	T_2 (ms)	O_2 (%)
2 M	A&V	41.8 ± 5.0	70.9 ± 3.7	29.7 ± 1.8	59.4 ± 2.1
	V	37.8 ± 3.2	67.8 ± 2.8	29.2 ± 2.8	58.7 ± 3.3
5 M	A&V	45.5 ± 5.8	73.5 ± 3.8	38.1 ± 6.9	67.6 ± 5.5
	V	45.7 ± 5.1	73.8 ± 3.2	38.8 ± 6.3	68.3 ± 5.0

using $Y_a = 100\%$ and OEF = 38.3 ± 5.3%) (10); and (2) 62% using positron emission tomography ($n = 24$, GM, calculated from $Y_a = 100\%$ and OEF = 38%) (47). In contrast, the mean GM oxygenation level measured by QUIXOTIC was76.9 ± 2.8% ($n = 4$), which is significantly higher ($t(3) = 6.50$, $P = 0.007$, post hoc power > 0.75) than VSEAN.

Venous T_2 Measurements Under Hypoxia

During the normoxia scans, the arterial O_2 saturation levels were 98% for both subjects 2 and 5; in the hypoxia scans, the saturation levels on subject 2 were between 84–86% during non-AN scan and 82–84% during AN scan; the saturation levels on subject 5 were between 86–88% in both AN and non-AN scans. The average changes of arterial O_2 saturation were 14% for subject 2 and 11% for subject 5.

Abnormal signal variations near the center of the brain were observed in subjects 2 and 5 (images not shown), but the high SNR signals in SS ROI seemed not to be affected, so only the SS ROI was used for both subjects 2 and 5 when comparing the normoxic and hypoxic experimental results.

The results of SS ROI analysis are listed in Table 3. A change of T_2 was detected, corresponding to an oxygenation change. The smaller venous oxygenation change in subject 5 was also reflected in the VSEAN results. The O_2 saturation changes measured by VSEAN (on the venous side) was smaller than that measured by oximeter (on the arterial side), this could be due to increased blood flow during acute hypoxia (48), which reduced the oxygenation change.

On both subjects 2 and 5, decreased VSEAN signals were observed during the hypoxia scans compared with the normoxia scans at the same eTE. This was mainly due to signal decay with lowered T_2 during hypoxia. Another factor that may affect the magnitude of the VSEAN signal is that the blood flow change during hypoxia might shift its velocity distribution, causing a change in the amount of flowing spins under observation. However, a decreased VSEAN signal should not bias the T_2 values, although its accuracy may be affected by decreased SNR.

DISCUSSION

The central features of the proposed VSEAN sequence were successfully demonstrated in phantom and human volunteer experiments, including static tissue suppression, VS excitation, arterial nulling and T_2, and oxygenation estimation. With a strictly positive $\sin^2$-shaped velocity excitation profile, VSEAN technique is immune to signal cancellation from flows in opposite directions. Flow geometry will affect the amplitude of the VSEAN signal, but in theory should not bias the T_2 measurement. However, the flow phantom studies indicated a minor trend of T_2 value lowering when the sample was moving and the VSEAN signal was very low. This may be caused by noise introduced by unstable flows in the phantom, or because the eTEs (10/30/70 ms or 30/50/90 ms) used here were not optimal to measure the sample with such long T_2 (~240ms), or flow effects. Fortunately, this effect would be less significant when measuring the blood T_2 (<120 ms). Nevertheless, this bias should be investigated more carefully in the future.

The velocity sensitivity of VSE pulse train and the contribution of blood from different sizes of vessels can be adjusted by changing the flow-weighting gradients. Analogous to the consideration of v_{cut} in VSASL experiment (49), lower v_e will bring the measurement closer to the tissue with improved localization but may cause signal reduction. In this study, the chosen v_e of 2 cm/s corresponds to venules/veins of diameters ranging from 100 to 200 μm in human retina (50). However, one would expect the mean velocities in venules/veins of the same size to be lower, as found by other studies on small animals, in the range of 0.8–1.8 cm/s (hamster) (51), 0.3–0.5 cm/s (cat sartorius muscle) (52). These results from small animals may not be directly applicable to the human brain. However, they suggest that lower v_e may be used in future experiments to optimize the SNR, which depends on the velocity distribution of the venous or arterial population of interest, and also to improve the localization of the VSEAN signal to tissue. The contribution from CSF was found to be negligible since the T_2 values were not biased towards that of CSF. However, lower v_e may generate a stronger signal from CSF, as the velocity of CSF on the surface of the brain is as high as 1.26 cm/s in the anterior cranial subarachnoid space (SAS) or 0.28 cm/s in the posterior cranial SAS within a cardiac cycle (53).

It is notable that in contrast to the VSASL experiment, there is not enough time between the VSE pulse train and the image acquisition for the blood at various velocities to mix, thus the $\sin^2$-shaped velocity excitation profile will largely remain, and higher harmonics (e.g., $v = 3v_e$, $5v_e$, ...) will also contribute to the total signal (Fig. 6). This provides the opportunity to observe the VSEAN signals in large vessels at the same time (Figs. 7

and 8). In brain tissue, the contribution from higher harmonics may not be significant due to the relatively narrow velocity distribution range on the venous side.

In order to eliminate the arterial contribution to the venous weighted signal, the nulled arterial blood should occupy the vessels with the velocity range of interest. This requires that at the time of imaging: (1) the leading edge of the inverted arterial bolus decelerates below v_e; and (2) the tail of the bolus has not yet entered the slice of interest. The former depends on the arterial transit time (ATT), i.e., the time for the inverted arterial blood to travel to arterioles or the arterial side of the capillaries, so that TI>ATT; while the latter depends on both the arterial transit time and the temporal width of the inverted arterial bolus, τ, so that TI $<$ ATT $+$ τ. A 20-mm gap between the inversion slab and the imaging slab yields an ATT of about 630 ms (54). In this study, we estimated an ATT of about 700 ms with the 25-mm gap used. With an inversion slab thickness of 200 mm, τ should be above 800 ms, because a typical inversion slab thickness of 100 mm yields a τ of 600 ms (55), so the TI $=$ 1150 mm in this study should satisfy both TI $>$ ATT and TI $<$ ATT $+$ τ. However, if the ATT increases significantly such that it exceeds the null point of arterial blood, e.g., under diseased conditions, this could bias the VSEAN measurement towards arterial side. On the other hand, ATT in QUIXOTIC is short and less likely to change under diseased conditions, although it has lower SNR and potential diffusion and eddy current issues as discussed before. Thus, combining these two techniques together may provide a solution in the presence of prolonged ATT, i.e., combining the VS modules from QUIXOTIC for insensitivity to ATT with "cos/sin" modulation and signal projection from VSEAN for venous signal isolation.

In this study, T_2 preparation was used to measure the T_2 values. Multiecho SE measurement provides higher temporal resolution and efficiency and is less sensitive to fluctuations across TRs. However, the accuracy of the T_2 measurement may be compromised by artifacts from flow through the multiecho imaging gradients, even echo refocusing effects (20,56), and wash-out effects across slice-selective refocusing pulses. Nevertheless, because of the higher temporal and SNR efficiency, multiecho approaches to T_2 measurement are an ongoing subject of study in our laboratory.

It is notable that the measured arterial T_2 values in this study were lower than those measured in big vessels (23), but in good agreement with the trend found in Refs. 32 and 33, that the arterial T_2 decreases as the arterial blood travels to smaller arteries and arterioles or even in capillaries due to the fast water exchange with tissues. As for the venous-weighted signal, when T_2-prep pulses were applied, water traveled downstream in venules where the fast water exchange was less likely to occur, possibly resulting in more reasonable T_2 values. Although lowered hematocrit in small vessels (57,58) is expected to raise the T_2 values (29,59), this was not observed in our experiments or was overwhelmed by the influence of fast water exchange.

The T_2 values measured with BIR4-based VSE/T_2prep module with variable gaps (VG) were lower than those measured using variable numbers (VN) of refocusing pulses (23,25). There may be at least two reasons for this. First, according to the Luz-Meiboom model (60), the apparent T_2 depends on the repetition rate of refocusing pulses in the presence of proton exchange between sites. With the VN method, the refocusing rate is kept constant, while with the VG method the rate decreases. Second, in VN method, spins experience more $T_{1\rho}$ relaxation and less T_2 decay during the refocusing pulses in ΔeTE, while in the VG method, spins experience pure T_2 decay during ΔeTE. Among the available calibration models from the literature, the one given in Ref. 29 used the VG method and was the most suitable for this study. However, the sequence to acquire the T_2 values in this study was not exactly the same as in Ref. 29 and may still result in inaccurate estimate of oxygenation level, as suggested from the arterial T_2–Y measurement in this study. Therefore, a calibration curve acquired using the same BIR4-based VSE/T_2prep would be preferred to give a better estimate of oxygenation measured by VSEAN, or a more careful study should be carried out to characterize the behavior of the pulse when the flow signal is very low.

It is also notable that the arterial O_2 saturation levels in GM were lower than one would expect, especially in subject 3. Possible reasons include: (1) lower T_2 due to fast water exchange resulting in lower apparent O_2 saturation levels; (2) actual oxygen loss along the vascular tree might occur earlier in the arterioles (61,62), e.g., the maximum oxygen saturation in arterioles could be as low as 89.6 $\pm$ 6.0% (51), or the measurement was biased toward the capillary side rather than to the arteriole side when the postlabeling delay was long; (3) low SNR; and (4) possible bias to the O_2 saturation introduced by errors in the T_2–Y calibration curve.

The detection and separation of venous and arterial signal in the GM and SS was demonstrated in this study. As noted in Fig. 8, the VSEAN technique can be applied on other vessels or tissues, e.g., the vessels on the scalp to monitor the metabolic rate of the scalp, or the vessels of the neck to simultaneously measure the arterial and venous oxygenation, and thereby the metabolic rate of the whole brain.

Currently, the VSEAN technique is limited to single-slice acquisition due to the single nulling point of arterial blood. To increase coverage, this technique is amenable to 3D acquisition.

CONCLUSIONS

The new VSEAN technique was demonstrated to efficiently isolate flow signals from static signals in phantoms, and venous-weighted signals from surrounding static tissue in both small and big veins in human volunteers. T_2 and oxygenation mapping of both venous and arterial blood in the brain was shown, as well as successful detection of the change of T_2 and oxygenation during a hypoxia challenge. Compared to the QUIXOTIC technique, the SNR, temporal efficiency and insensitivity to slow motion are improved, and contamination from diffusion attenuation is eliminated.

ACKNOWLEDGMENTS

The authors thank David Dubowitz and Zachary Smith for their help on data collection.

REFERENCES

1. Astrup J, Siesjo BK, Symon L. Thresholds in cerebral ischemia—the ischemic penumbra. Stroke 1981;12:723–725.
2. Baron JC, Bousser MG, Rey A, Guillard A, Comar D, Castaigne P. Reversal of focal "misery-perfusion syndrome" by extra-intracranial arterial bypass in hemodynamic cerebral ischemia. A case study with 15O positron emission tomography. Stroke 1981;12:454–459.
3. Baron JC. Mapping the ischaemic penumbra with PET: implications for acute stroke treatment. Cerebrovasc Dis 1999;9:193–201.
4. Guadagno JV, Warburton EA, Aigbirhio FI, Smielewski P, Fryer TD, Harding S, Price CJ, Gillard JH, Carpenter TA, Baron J-C. Does the acute diffusion-weighted imaging lesion represent penumbra as well as core? A combined quantitative PET/MRI voxel-based study. J Cereb Blood Flow Metab 2004;11:1249–1254.
5. Sobesky J, Weber OZ, Lehnhardt FG, Hesselmann V, Neveling M, Jacobs A, Heiss WD. Does the mismatch match the penumbra? Magnetic Resonance imaging and positron emission tomography in early ischemic stroke. Stroke 2005;36:980–985.
6. Abate MG, Trivedi M, Fryer TD, Smielewski P, Chatfield DA, Williams GB, Aigbirhio F, Carpenter TA, Pickard JD, Menon DK, Coles JP. Early derangements in oxygen and glucose metabolism following head injury: The ischemic penumbra and pathophysiological heterogeneity. Neurocrit Care 2008;9:319–325.
7. Heiss WD. Identifying thresholds for penumbra and irreversible tissue damage. Stroke 2004;35(11_suppl_1):2671–2674.
8. Ogawa S, Lee T-M. Magnetic resonance imaging of blood vessels at high fields: in vivo and in vitro measurements and image simulation. Magn Reson Med 1990;16:9–18.
9. Davis TL, Kwong KK, Weisskoff RM, Rosen BR. Calibrated functional MRI: mapping the dynamics of oxidative metabolism. Proc Natl Acad Sci USA 1998;95:1834–1839.
10. He X, Yablonskiy DA. Quantitative BOLD: mapping of human cerebral deoxygenated blood volume and oxygen extraction fraction: default state. Magn Reson Med 2007;57:115–126.
11. Yablonskiy DA, Haacke EM. Theory of NMR signal behavior in magnetically inhomogeneous tissues—the static dephasing regime. Magn Reson Med 1994;32:749–763.
12. Christen T, Lemasson B, Pannetier N, Farion R, Segebarth C, Remy C, Barbier EL. Evaluation of a quantitative blood oxygenation level-dependent (qBOLD) approach to map local blood oxygen saturation. NMR Biomed 2011;24:393–403.
13. Jain V, Langham MC, Wehrli FW. MRI estimation of global brain oxygen consumption rate. J Cereb Blood Flow Metab 2010;30:1598–1607.
14. Fernández-Seara MA, Techawiboonwong A, Detre JA, Wehrli FW. MR susceptometry for measuring global brain oxygen extraction. Magn Reson Med 2006;55:967–973.
15. Haacke EM, Lai S, Reichenbach JR, Kuppusamy K, Hoogenraad FGC, Takeichi H, Lin WL. In vivo measurement of blood oxygen saturation using magnetic resonance imaging: a direct validation of the blood oxygen level-dependent concept in functional brain imaging. Hum Brain Mapp 1997;5:341–346.
16. Lu HZ, van Zijl PCM. Experimental measurement of extravascular parenchymal BOLD effects and tissue oxygen extraction fractions using multi-echo VASO fMRI at 1.5 and 3.0 T. Magn Reson Med 2005;53:808–816.
17. An HY, Lin WL. Quantitative measurements of cerebral blood oxygen saturation using magnetic resonance imaging. J Cereb Blood Flow Metab 2000;20:1225–1236.
18. Foltz WD, Merchant N, Downar R, Stainsby TA, Wright GA. Coronary venous oximetry using MRI. Magn Reson Med 1999;42:837–848.
19. Oja JM, Gillen JS, Kauppinen RA, Kraut M, van Zijl PC. Determination of oxygen extraction ratios by magnetic resonance imaging. J Cereb Blood Flow Metab 1999;19:1289–1295.
20. Golay X, Silvennoinen MJ, Zhou J, Clingman CS, Kauppinen RA, Pekar JJ, van Zij PC. Measurement of tissue oxygen extraction ratios from venous blood T(2): increased precision and validation of principle. Magn Reson Med 2001;46:282–291.
21. Wright GA, Hu BS, Macovski A. Estimating oxygen saturation of blood in vivo with MR imaging at 1.5T. J Magn Reson Imaging 1991; 1:275–283.
22. Chien D, Levin DL, Anderson CM. MR gradient echo imaging of intravascular blood oxygenation: T_2^* determination in the presence of flow. Magn Reson Med 1994;32:540–545.
23. Lee T, Stainsby JA, Hong J, Han E, Brittain J, Wright GA. Blood Relaxation Properties at 3T—Effects of Blood Oxygen Saturation. In: Proceedings of the 11th Annual Meeting of ISMRM, Toronto, Ontario, Canada, 2003. p 131.
24. Yablonskiy DA. Quantitation of intrinsic magnetic susceptibility-related effects in a tissue matrix. Phantom study. Magn Reson Med 1998;39:417–428.
25. Lu HZ, Ge YL. Quantitative evaluation of oxygenation in venous vessels using T_2-relaxation-under-spin-tagging MRI. Magn Reson Med 2008;60:357–363.
26. Bolar DS, Rosen BR, Sorensen AG, Adalsteinsson E. QUantitative Imaging of eXtraction of Oxygen and TIssue Consumption (QUIXOTIC) using velocity selective spin labeling. In: Proceedings of the 17th Annual Meeting of ISMRM, Honolulu, Hawaii, USA, 2009. p 628.
27. Bolar DS. Magnetic resonance imaging of the cerebral metabolic rate of oxygen ($CMRO_2$) [Ph.D. Thesis]. Cambridge: Massachusetts Institute of Technology; 2010.
28. Guo J, Wong EC. Imaging of Oxygen Extraction Fraction Using Velocity Selective Excitation with Arterial Nulling (VSEAN). In: Proceedings of the 18th Annual Meeting of ISMRM, Stockholm, Sweden, 2010. p 4057.
29. Zhao JM, Clingman CS, Närväinen MJ, Kauppinen RA, van Zijl PCM. Oxygenation and hematocrit dependence of transverse relaxation rates of blood at 3T. Magn Reson Med 2007;58:592–597.
30. Chen JJ, Pike GB. Human whole blood T_2 relaxometry at 3 Tesla. Magn Reson Med 2009;61:249–254.
31. Stefanovic B, Pike GB. Human whole-blood relaxometry at 1.5T: assessment of diffusion and exchange models. Magn Reson Med 2004;52:716–723.
32. Wells JA, Lythgoe MF, Choy M, Gadian DG, Ordidge RJ, Thomas DL. Characterizing the origin of the arterial spin labelling signal in MRI using a multiecho acquisition approach. J Cerebral Blood Flow; Metabolism 2009;29:1836–1845.
33. Liu P, Uh J, Lu H. Determination of spin compartment in arterial spin labeling MRI. Magn Reson Med 2011;65:120–127.
34. Wong EC, Guo J. BIR-4 based B1 and B0 insensitive velocity selective pulse trains. In: Proceedings of the 18th Annual Meeting of ISMRM, Stockholm, Sweden, 2010. p 2853.
35. Wong EC, Cronin M, Wu W-C, Inglis B, Frank LR, Liu TT. velocity selective arterial spin labeling. Magn Reson Med 2006;55:1334–1341.
36. Norris DG, Schwartzbauer C. Velocity selective radiofrequency pulse trains. J Magn Reson 1999;137:231–236.
37. Garwood M, DelaBarre L. The return of the frequency sweep: designing adiabatic pulses for contemporary NMR. J Magn Reson 2001;153: 155–177.
38. Silver MS, Joseph RI, Hoult DI. Selective spin inversion in nuclear magnetic resonance and coherent optics through an exact solution of the Bloch-Riccati equation. Phys Rev A 1985;31:2753–2755.
39. Wong EC, Buxton RB, Frank LR. Implementation of quantitative perfusion imaging techniques for functional brain mapping using pulsed arterial spin labeling. NMR Biomed 1997;10:237–249.
40. Edelman RR, Siewert B, Darby DG, Thangaraj V, Nobre AC, Mesulam MM, Warach S. Qualitative mapping of cerebral blood flow and functional localization with echo-planar MR imaging and signal targeting with alternating radio frequency (STAR) sequences: applications to MR angiography. Radiology 1994;192:513–520.
41. Kwong KK, Belliveau JW, Chesler DA, Goldberg IE, Weisskoff RM, Poncelet BP, Kennedy DN, Hoppel BE, Cohen MS, Turner R, Cheng H-M, Brady TJ, Rosen BR. Dynamic magnetic resonance imaging of human brain activity during primary sensory stimulation. Proc Natl Acad Sci USA 1992;89:5675–5679.
42. Kim S-G. Quantification of regional cerebral blood flow change by flow-sensitive alternating inversion recovery (FAIR) technique: application to functional mapping. Magn Reson Med 1995;34:293–301.
43. Nezafat R, Ouwerkerk R, Derbyshire AJ, Stuber M, McVeigh ER. Spectrally selective B_1-insensitive T_2 magnetization preparation sequence. Magn Reson Med 2009;61:1326–1335.
44. de Graaf RA, Rothman DL, Behar KL. Adiabatic RARE imaging. NMR Biomed 2003;16:29–35.
45. Lu H, Clingman C, Golay X, van Zijl PCM. Determining the longitudinal relaxation time (T_1) of blood at 3.0 Tesla. Magn Reson Med 2004;52:679–682.

46. Erdfelder E, Faul F, Buchner A, Lang AG. Statistical power analyses using G*Power 3.1: tests for correlation and regression analyses. Behav Res Methods 2009;41:1149–1160.
47. Leenders KL, Perani D, Lammertsma AA, Heather JD, Buckingham P, Healy MJR, Gibbs JM, Wise RJS, Hatazawa J, Herold S, Beaney RP, Brooks DJ, Spinks T, Rhodes C, Frackowiak RSJ, Jones T. Cerebral blood-flow, blood-volume and oxygen utilization—normal values and effect of age. Brain 1990;113:27–47.
48. Dubowitz DJ, Dyer EA, Theilmann RJ, Buxton RB, Hopkins SR. Early brain swelling in acute hypoxia. J Appl Physiol 2009;107:244–252.
49. Wu WC, Wong EC. Intravascular effect in velocity-selective arterial spin labeling: the choice of inflow time and cutoff velocity. Neuroimage 2006;32:122–128.
50. Riva CE, Grunwald JE, Sinclair SH, Petrig BL. Blood velocity and volumetric flow rate in human retinal vessels. Invest Ophthalmol Vis Sci 1985;26:1124–1132.
51. Alves de Mesquita J, Jr., Bouskela E, Wajnberg E, Lopes de Melo P. Improved instrumentation for blood flow velocity measurements in the microcirculation of small animals. Rev Sci Instrum 2007;78:024303 1–6.
52. House SD, Johnson PC. Diameter and blood-flow of skeletal-muscle venules during local flow regulation. Am J Physiol 1986;250: H828–H837.
53. Kurtcuoglu V, Gupta S, Soellinger M, Grzybowski DM, Boesiger P, Biddiscombe J, Poulikakos D. Cerebrospinal fluid dynamics in the human cranial subarachnoid space: an overlooked mediator of cerebral disease. I. Computational model. J Royal Society Interface 2010; 7:1195–1204.
54. Qiu M, Paul Maguire R, Arora J, Planeta-Wilson B, Weinzimmer D, Wang J, Wang Y, Kim H, Rajeevan N, Huang Y, Carson RE, Constable RT. Arterial transit time effects in pulsed arterial spin labeling CBF mapping: insight from a PET and MR study in normal human subjects. Magn Reson Med 2010;63:374–384.
55. Wong EC, Buxton RB, Frank LR. Quantitative imaging of perfusion using a single subtraction (QUIPSS and QUIPSS II). Magn Reson Med 1998;39:702–708.
56. Kucharczyk W, Brant-Zawadzki M, Lemme-Plaghos L, Uske A, Kjos B, Feinberg DA, Norman D. MR technology: effect of even-echo rephasing on calculated T_2 values and T_2 images. Radiology 1985; 157:95–101.
57. Fahraeus R. The suspension stability of the blood. Physiol Rev 1929; 9:241–274.
58. Levin VA, Gilboe DD. Blood volume, hematocrit and pressure relationships in the isolated perfused dog brain. Stroke 1970;1:270–277.
59. Hayman LA, Ford JJ, Taber KH, Saleem A, Round ME, Bryan RN. T_2 effect of hemoglobin concentration—assessment with invitro MR spectroscopy. Radiology 1988;168:489–491.
60. Luz Z, Meiboom S. Nuclear magnetic resonance study of protolysis of trimethylammonium ion in aqueous solution—order of reaction with respect to solvent. J Chem Phys 1963;39:366–370.
61. Popel AS, Pittman RN, Ellsworth ML. Rate of oxygen loss from arterioles is an order of magnitude higher than expected. Am J Physiol 1989;256:H921–H924.
62. Kobayashi H, Takizawa N. Imaging of oxygen transfer among microvessels of rat cremaster muscle. Circulation 2002;105:1713–1719.

Acknowledgements

Chapter 3, in full, is a reprint of the material as it appears in Magnetic Resonance in Medicine 2012. Guo J, Wong EC. Venous oxygenation mapping using velocity-selective excitation and arterial nulling. Magn Reson Med. 2012 Nov;68(5):1458-71. doi: 10.1002/mrm.24145. The dissertation author was the primary investigator and author of this paper.

CHAPTER 4 : Blind detection of vascular sources and territories using random vessel encoded arterial spin labeling

Eric C. Wong · Jia Guo

Received: 14 August 2011 / Revised: 22 December 2011 / Accepted: 26 December 2011

Abstract
Object The goal of this work is to use vessel encoded arterial spin labeling (VEASL) methods to detect feeding arteries without prior knowledge of their positions, and map the vascular territory of each.
Materials and methods Five healthy subjects were scanned, each with four different tagging planes. The VEASL tagging method was modified to use 60 different pairs of encoding steps with random orientation and spacing. A signal model was developed to calculate the theoretical ASL signal resulting from a vessel in any position in the tagging plane. For each voxel, the location of the feeding vessel was estimated by finding the theoretical signal that correlates most closely with the data.
Results The main intracranial arteries, including carotid, vertebral, basilar, and cerebral arteries above the Circle of Willis were identified and localized from the ASL data in all subjects. In addition, external carotid branches were detected in all subjects.
Conclusions Randomly encoded VEASL provides data that allows for blind detection of source vessels. This method simplifies the VEASL prescription process and allows for efficient detection of atypical or collateral circulation.

E. C. Wong (✉)
Departments of Radiology and Psychiatry, UCSD Center for Functional MRI, 9500 Gilman Drive, MC 0677, La Jolla, CA 92093-0677, USA
e-mail: ecwong@ucsd.edu

J. Guo
Department of Bioengineering, University of California, San Diego, CA, USA

Keywords Magnetic resonance imaging · Stroke · Collateral circulation · Cerebral arteries · Cerebrovascular circulation

Introduction

For most ASL methods, the primary goal is to provide accurate and robust measures of perfusion. However, through manipulation of the tagging process, ASL can be extended to provide additional information on which source vessels supply which target tissues. This information, which is typically in the form of vascular territory maps, may be useful for applications such as the evaluation of stroke, risk assessment in cerebrovascular disease, and planning of treatment for tumors. ASL-based territory mapping methods include some which apply ASL tags to single vessels [1–3], and others which encode the tagging process for two or more feeding arteries such that multiple vascular territories can be decoded and mapped simultaneously [4–6]. One of these methods is vessel encoded arterial spin labeling (VEASL) [5], in which pseudo-continuous ASL (PCASL) tagging [7] is used with additional gradient pulses applied across the tagging plane to encode the ASL data with information about the location of the feeding arteries. As originally described, VEASL requires prior knowledge of the locations of vessels to be tagged in order to prescribe a series of Hadamard encoding steps across the source vessels. This in turn necessitates the collection of an angiogram, and user input or an automated algorithm for detection of vessel locations in the tagging plane. In an effort to automate the scan prescription process, Gevers et al. introduced a planning-free VEASL method [8] that uses a small number of generically defined encoding steps, and demonstrated repeatable detection of

flow territories using this approach. We explore here the use of a large number of random encoding steps to not only map vascular territories without planning, but to also uniquely identify the locations of the source arteries in the tagging plane. This provides the opportunity to identify collateral or atypical routes of circulation that may not previously be known, and may be clinically relevant.

In addition to the positions of feeding arteries, resonance offsets at the locations of the arteries in the tagging plane can also significantly affect the tagging efficiency, and methods have been proposed to either measure and correct for these offsets [9, 10] or to reduce sensitivity to them using multiphase PCASL [11]. The randomly encoded method proposed here allows for efficient estimation of both the locations and resonance offsets of feeding arteries without prior knowledge of either. Portions of this work were presented in abstract form in [12].

Materials and methods

In the original implementation of VEASL, transverse gradient pulses of alternating sign were used between RF pulses to provide vessel encoding. In the presence of resonance offsets in the tagging plane, this approach results in decreased tagging efficiency, as shown in Fig. 1a. These curves were calculated by Bloch simulation, assuming a range of flow velocities uniformly distributed from 5 to 40 cm/s in the direction of the tagging gradients, the RF and gradient parameters given below, an assumed T_2 of 200 ms for arterial blood, and neglecting T_1 decay. We note that using unipolar transverse gradient pulses for vessel encoding can provide similar encoding functionality, but with two differences [12]. First, the tagging curve as a function of the location between fully inverted and unperturbed vessels has a different shape (Fig. 1b). This curve is very well fit using three Fourier coefficients, and is given by:

$$\Delta M_Z = 2.092\,cos(\theta) - 0.322\,cos(3\theta) + 0.053\,cos(5\theta),$$

where θ is the phase along the periodic function. SNR efficiency in VEASL can be calculated using Equation 4 of [5], and is maximized using Hadamard encoding. Because the unipolar encoding curve of Fig. 1b is more weighted towards ± 1 than that of bipolar encoding (Fig. 1a), unipolar encoding more closely approximates Hadamard encoding steps, and the overall SNR is higher. Second, for unipolar encoding, resonance offsets at the tagging location result in a simple shift in the tagging curve, which does not affect the overall tagging efficiency and SNR, as opposed to the decrease in tagging efficiency that is seen with resonance offset in the bipolar case (Fig. 1). For these reasons we are currently using the unipolar approach. In order for the RF pulses to follow the phase of the spins in a vessel to be inverted, the additional phase ϕ_i (described in [5]) is given by $\phi_i = i\pi a/\lambda$, where i is the pulse number, a is the projection of the vector from isocenter to the vessel onto the direction of encoding (see [5]), and λ is encoding wavelength. For the original alternating gradient method, $\phi_i = (i\%2)\pi a/\lambda$, where % represents the integer modulus function.

Five healthy subjects were studied in a General Electric MR750 3T scanner, using a commercial 8-channel head RF coil, under a protocol approved by the local IRB. MR angiograms were acquired and were used to select the four tagging planes shown in Fig. 2. Location A features a trapezoidal arrangement of internal carotid and vertebral arteries, has relatively straight arterial segments, and allows for the possibility of separately tagging the two vertebral arteries. Location B has an anatomically very consistent arrangement of carotid and basilar arteries, but has tortuous segments nearby and typically large resonance offsets. Locations C and D are two candidate locations for tagging above the Circle of Willis (CoW) that may allow for tagging of anterior, middle, and posterior cerebral arteries. Between these two locations the anterior cerebral artery runs nearly straight posterior-anterior and is difficult to tag.

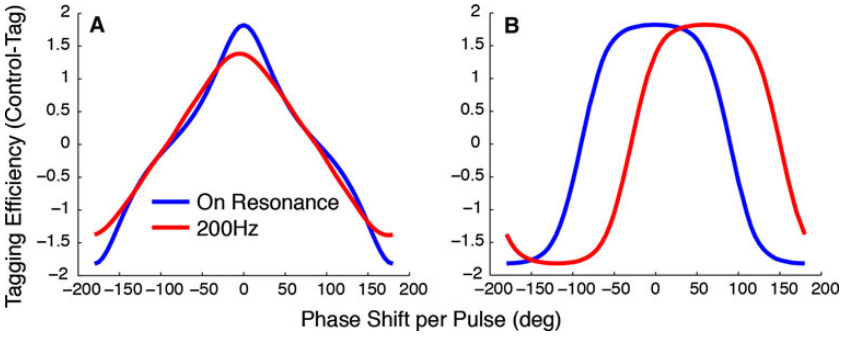

Fig. 1 Calculated VEASL signal as a function of transverse gradient induced phase shift per pulse. **a** Bipolar gradient pulses; **b** Unipolar pulses used in this study. A resonance offset at the tagging location results in reduced tagging efficiency for the bipolar pulse train, but a simple shift without amplitude reduction for the unipolar pulse train

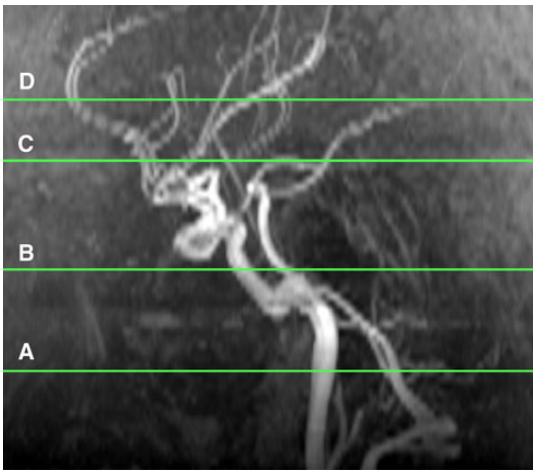

Fig. 2 Tagging planes superimposed on a sagittal projection of an MR angiogram. *A* Trapezoidal arrangement of internal carotid and vertebral arteries; *B* Triangular arrangement of internal carotid and basilar arteries at the level of the sphenoid sinus; *C* and *D* Above the Circle of Willis, allowing tagging of anterior and posterior cerebral arteries, and branches of the middle cerebral artery

At each of these tagging locations, the same 60 pairs of encoding steps were acquired, with random orientation, random phase θ, and random wavelength λ ranging from 15 to 85 mm, in addition to two pairs of non-vessel encoded steps for a total of 124 TR periods per scan. The random encoding steps were generated once and the same encodings used for every subject. The actual encodings used are available at http://cfmriweb.ucsd.edu/ecwong/public/rveasl_encodings.txt. For the second of each pair of encoding steps, the RF phase was alternated between 0 and 180° relative to the first step, such that a difference signal between the pair removes static tissue signal and leaves a symmetrical dependence of the ASL signal upon vessel location, as shown in Fig. 1b. Scan parameters were: single shot gradient echo spiral acquisition with 64^2 matrix, 22 cm FOV, nine 8 mm slices with 2 mm spacing, spatial spectral excitation, 2 μs sampling, 1.6 s tag duration, 800 μs Hamming shaped pulses with 1.4 ms spacing, tagging gradients with 8mT/m amplitude and 0.6 mT/m mean value, 1 s post labeling delay, and 3 s TR.

Images were subtracted pairwise, resulting in 61 difference images, one without transverse encoding averaged from the two pairs of non-encoded scans. For a uniform array of assumed vessel locations spanning ±64 mm with 2 mm spacing in both X and Y directions, and resonance offsets spanning ±220 Hz with 11 Hz spacing, the theoretical ASL signal across encoding steps was calculated using the random but known encoding parameters and assuming the response of Fig. 1b. This generates a matrix that maps X and Y vessel coordinates and Frequency (XYF) space into 61 dimensional ASL signal space. For each voxel in the data, the correlation coefficient (CC) between the acquired signal and the theoretical ASL signal from every XYF location was calculated, and the point in XYF space corresponding to the highest CC (CCmax) was assigned to that voxel. For this vessel detection step, images were down sampled to 32^2 using a 2×2 box shaped kernel to speed up the processing. The choice of 2 mm spacing in XY, and 11 Hz spacing in F is somewhat arbitrary. It is not the resolution in these dimensions, but simply needs to be fine enough so that correlation maxima (CCmax) in XYF space are not missed. Finer spacing than is necessary for identifying vessels is not likely to be useful, and increases computation time. Processing time for one scan (7 slices, 124 images of each) was less than one minute running in Matlab on a 8-core Linux server.

Results

A map of CCmax, and a histogram thereof are shown in Fig. 3. The histogram clearly shows a bimodal distribution, with the lower peak corresponding to areas of low or no

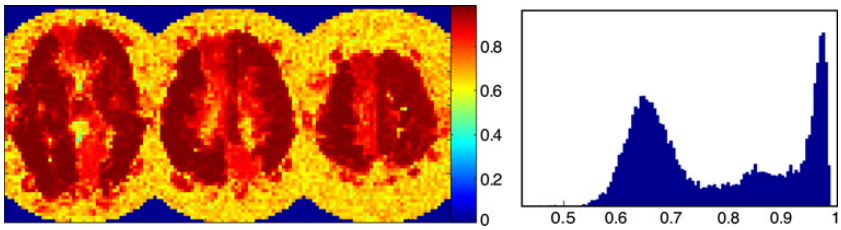

Fig. 3 Maximum correlation coefficient (CCmax) between signal from each voxel and predicted signal from any point in the XYF tagging space (see text). *Left* A map of CCmax shows high values in *gray* matter. In this subject, both the right anterior cerebral and the left posterior cerebral artery territories receive mixed supplies, and CCmax is lower in these areas. Note the high CCmax areas outside the brain, which correspond to extracranial vessels. *Right* A histogram of CCmax values shows a peak near 0.65 which corresponds to noise voxels. A CCmax threshold of 0.8 was used in this study to identify voxels that fit the signal model well, and were used to detect source vessels

perfusion (including noise outside the head), and the higher peak corresponding to voxels with high perfusion and good fit to the signal model. Voxels with CCmax >0.8 were used for estimation of vessel locations, and histograms of those voxels in XYF space were constructed. An example, with three orthogonal projections of this 3-dimensional histogram are shown in Fig. 4. Clusters in this histogram were identified manually, and the centroids of the clusters represent estimated vessel locations and resonance offsets in the tagging plane. These vessels locations were used to construct an encoding matrix and used in a linear analysis as in [5], allowing for detection and estimation of mixed supplies where they occur. In the color vascular territory maps shown, the brightness is proportional to the total flow from all feeding arteries, and the color is derived from the colors assigned arbitrarily to each vessel, mixed in RGB color space weighted by the relative contribution from each vessel.

In the example shown in Fig. 4, eight clusters are apparent in the projection of the XYF histogram onto the XY plane (Fig. 4a). The locations of these clusters are superimposed on an anatomical image of the tagging plane in Fig. 4d, and show that the central four vessels are the internal carotid and vertebral arteries. The left and right carotid arteries are designated blue and red, respectively, and the purple color of the right anterior cerebral artery territory in Fig. 4e indicates that in this subject, that territory receives a mixed supply from left and right carotids. This is consistent with data from this subject using conventional (non-random) VEASL, and MR angiography that shows a patent anterior communicating artery (data not shown). The measured resonance offsets (horizontal axis in Fig. 4b and vertical axis in Fig. 4c) are relatively small among these four vessels, ranging from −18 to 24 Hz. In addition to the four intracranial arteries, four peaks in the histogram, indicated by the arrows in Fig. 4a, presumably correspond to the temporal and occipital branches of the external carotid arteries. The vascular territories of these four arteries are indicated by arrows with corresponding colors in Fig. 4e. These territories have been increased in brightness by a factor of three for visibility, and are likely mainly cutaneous arteries, many of which are blurred by the spiral acquisition. External carotid territories were detected consistently in all scans.

Figure 5 shows the vascular territories of the intracranial arteries for all five subjects, for three of the four tagging planes. Only one of the nine slices is shown. The highest tagging plane (Fig. 2d) yielded results similar to plane c, and is not shown. In this figure, the relevant region of the tagging plane is shown below each territory map, with the XY projection of the XYF histogram overlayed on the anatomical image in magenta. Vessels locations were chosen manually at the peaks of the histogram, and are indicated by asterisks, with colors corresponding to associated

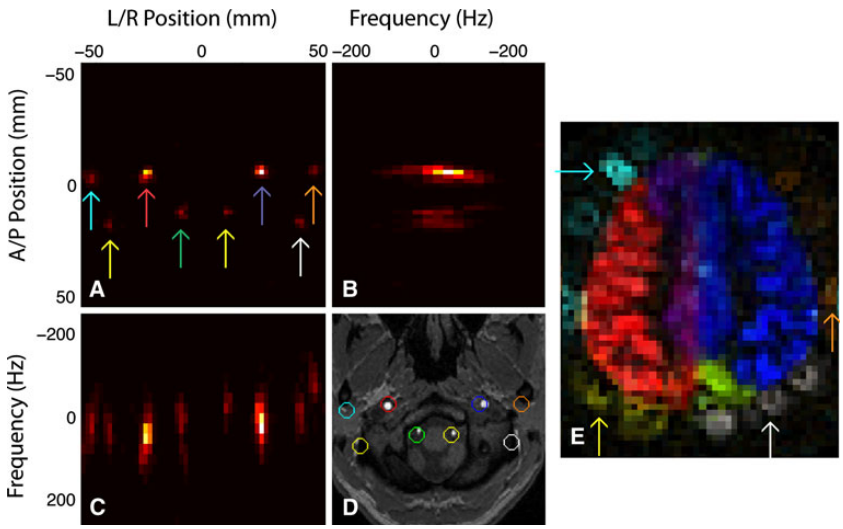

Fig. 4 Detection of source vessels. Three orthogonal projections of 3D histogram of voxels projected into XYF space (see text). **a** Projection onto XY plane; **b** Projection onto FY plane; **c** Projection onto XF plane. Peaks in these projections correspond to source vessels. **d** Eight peaks seen in **a**, shown as colored circles, superimposed on an anatomical image of the tagging plane. These eight vessels correspond to two carotid arteries, two vertebral arteries, and four extracranial arteries. **e** Territories mapped using the same color scheme as the circles in **d**, with extracranial territories increased in brightness by a factor of three for visibility. Extracranial territories were detected in all subjects, and are indicated by arrows. Right anterior cerebral territory receives mixed left and right carotid contributions, resulting in a *purple color* (a mix of *red* and *blue*)

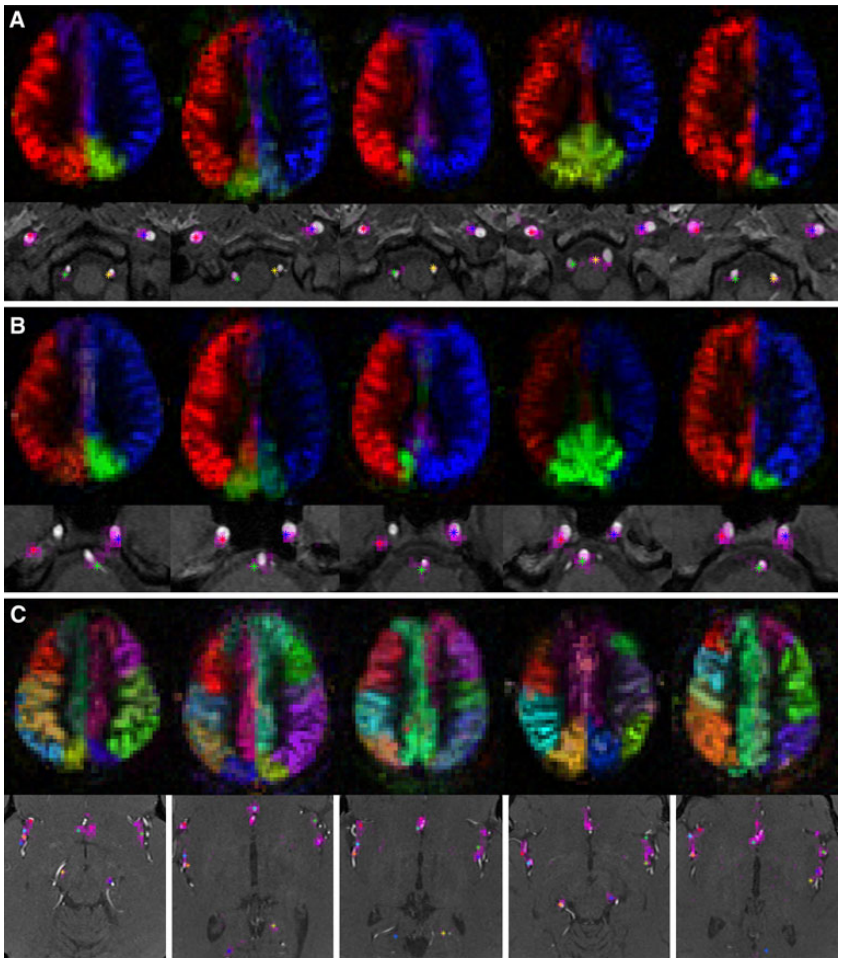

Fig. 5 Source vessels and vascular territories for all 5 subjects (*left to right*). *From Top* tagging planes **a**, **b**, and **c** (see Fig. 2). Below each territory map, an anatomical image of the tagging plane is shown, with a projection of the histogram in XYF space superimposed in magenta. Peaks in this histogram are identified with colored asterisks, with colors corresponding to the vascular territory map

vascular territory. In all subjects, separate peaks in the histogram corresponding to left and right vertebral arteries were seen (top row), although the number of voxels appearing at each vertebral location can be small. In row 2, subects 1 and 3, the localization of the right carotid artery was significantly off, but the nearest peak in the XY histogram did correctly identify the vascular territory. The resonance offsets at this tagging plane can be very large, as the vessels are close to the sphenoid sinus, and it was suspected that the resonance offset could affect the vessel localization. However the offsets measured at the two mislocalized carotid arteries were 21 Hz and 75 Hz, while larger offsets were measured in other subjects. For example, offsets of 214 Hz, 184 Hz, and 227 Hz were measured for subject 2 in this plane, and the localization in that subject was good. For tagging above the CoW (row 3), multiple vessels, including anterior and posterior cerebral arteries, and several branches of the middle cerebral arteries are consistently detected.

Discussion

The data shown here demonstrates that randomly encoded VEASL data can provide sufficient information to decode source vessel locations. Using a threshold on CCmax was an effective means of identifying voxels that will provide accurate vessel localization. The simple VEASL signal model used here, which assumes a single response function independent of flow velocity, is accurate enough to provide

fits to the data with CC >0.8, and often exceeding 0.95. We initially used signal variance across encodes as a parameter to select voxels for source analysis, but found that cardiac pulsations, which generate large and synchronous signal modulation across many voxels, often cluster to a spurious point in XYF space, leading to identification of a vessel that does not exist. The use of a CCmax threshold effectively reduces this problem, as we have not found vascular pulsations to pass the threshold. Because of the large number of points in XYF space ($65 \times 65 \times 41$), the CC between even pure noise and the best fitting signal model is relatively high (i.e the peak centered around 0.65 in Fig. 3). For smaller numbers of encoding steps, CCmax for noise is even higher, and was found to be 0.75 with 30 pairs of encoding steps, and 0.90 with 15 pairs of encodings. Thus, for the CCmax threshold of 0.8 used in this study, approximately 60 pairs of encoding steps (as used in this study) are required to provide a clear separation in CCmax between well perfused voxels and noise.

In areas that receive mixed supply, the VEASL signal should not correlate well with the signal model associated with any single point in XYF space. The potential for this to compromise vessel detection is clearly present when tagging the vertebral arteries, as they join to form the basilar artery prior to entering the CoW. Apparently in all five of the subjects studied, there is a sufficient lack of mixing in at least some portion of the posterior territory that both vertebral arteries could be identified. This is consistent with [13] in which a general lack of complete vertebral mixing was found, but it is not yet known whether this is reliably the case across the population.

In this work we have demonstrated that it is not necessary to identify source vessels within the tagging plane prior to VEASL scanning. However, we did use an angiogram to choose tagging planes that contain relatively straight and well separated vessel segments. A study to determine the effect of the choice of tagging plane on the effectiveness of random VEASL is currently underway. It is possible that choosing a tagging plane based on anatomical landmarks, as is commonly done for conventional PCASL, is sufficient for random VEASL, but this remains to be seen. Under most circumstances where VEASL data is of interest, an angiogram is likely to be desired as well, so it is unlikely that random VEASL would reduce the scan time per se. One goal of random VEASL is to reduce the required user input for scan prescription, which may save time, but the more important goal is to detect all source vessels. An obvious example is the detection of an external carotid collateral in a patient with cerebrovascular disease such as stroke or carotid stenosis, and it is promising that in this study, the territories of extracranial arteries were consistently detected.

The SNR efficiency of random VEASL is in principle similar to that of multiphase PCASL [11]. While multiphase PCASL uniformly samples the tagging efficiency curve of Fig. 1 to provide insensitivity to resonance offsets, random VEASL randomly samples the same curve, but with a different random sampling pattern for each point in the tagging plane. The SNR efficiency can be calculated as described in [5] for any given encoding matrix, and depends on proximity of other detected vessels. If two vessels are close to one another in XYF space, this translated into a poorly conditioned encoding matrix and noise amplification in the decoding process. For vessels that are far apart, the encoding matrix is well conditioned, and the SNR efficiency approaches the RMS value of the tagging efficiencies of the encoding steps. For conventional PCASL with perfect tagging efficiency and no resonance offset the SNR efficiency is 1. If the tagging efficiency curve was a simple sinusoid, then the SNR efficiency for either densely sampled MP-PCASL or random VEASL would be $1/\sqrt{2} = 0.707$, as this is the RMS value of a sin function. For the calculated curve of Fig. 1b, the RMS value is slightly higher (0.74), which is identical to the SNR efficiency calculated through the decoding matrix for distant vessels. Our preliminary calculations show that the SNR efficiency falls to half of this value (0.37) due to noise amplification when two vessels are 6 mm apart. More complete characterization of the SNR behavior of random VEASL is currently underway.

Localization of the decoded vascular sources was accurate in most but not all cases. In particular, the localization of the right internal carotid at the level of the sphenoid sinus in subjects 1 and 3 was significantly off, and the cause of this is currently under investigation.

The vessel locations in this study were chosen by hand at the local peaks of the histogram of voxels in XY tagging plane space. For most of the cases, particularly below the CoW, a simple threshold detected the same vessel locations, but above the CoW the identification of vessels is more uncertain. The automation of vascular territory detection is an important next step in this line of work, as it would more fully realize the potential of automated vascular territory mapping without a priori knowledge of vessel locations. Approaches of interest include clustering methods [14, 15] in any combination of three spaces: physical brain space, as territories tend to be contiguous in the brain; raw data space, where the noise often has predictable characteristics; and XYF tagging plane space, where the vessels are inherently sparse. Bayesian estimation methods have also been applied with success to the general problem of VEASL data processing [16, 17], and can be adapted to the methods described here. The authors are willing to share the raw data from this study with researchers who are interested in developing or testing algorithms for improved detection of vessels and/or mapping of territories.

Conclusion

We have demonstrated here that randomly encoded VEASL allows for the unique identification of source vessel locations and resonance offsets. We expect that this new method may provide important and specific information for the diagnosis and management of cerebrovascular disease, tumors, and other conditions where collateral or aberrant flow patterns may be present and it is important to identify the arterial supply.

Acknowledgments This work was supported by Grant R01 EB002096 from the National Institutes of Health.

References

1. Davies NP, Jezzard P (2003) Selective arterial spin labeling (SASL): perfusion territory mapping of selected feeding arteries tagged using two-dimensional radiofrequency pulses. Magn Reson Med 49(6):1133–1142
2. Werner R, Norris DG, Alfke K, Mehdorn HM, Jansen O (2005) Continuous artery-selective spin labeling (CASSL). Magn Reson Med 53(5):1006–1012
3. Helle M, Norris DG, Rufer S, Alfke K, Jansen O, van Osch MJ (2010) Superselective pseudocontinuous arterial spin labeling. Magn Reson Med 64(3):777–786
4. Gunther M (2006) Efficient visualization of vascular territories in the human brain by cycled arterial spin labeling MRI. Magn Reson Med 56(3):671–675
5. Wong EC (2007) Vessel encoded arterial spin labeling using pseudo-continuous tagging. Magn Reson Med 58(6):1086–1091
6. Zimine I, Petersen ET, Golay X (2006) Dual vessel arterial spin labeling scheme for regional perfusion imaging. Magn Reson Med 56(5):1140–1144
7. Dai W, Garcia D, de Bazelaire C, Alsop DC (2008) Continuous flow-driven inversion for arterial spin labeling using pulsed radio frequency and gradient fields. Magn Reson Med 60(6):1488–1497
8. Gevers S, Bokkers RP, Hendrikse J, Majoie CB, Kies DA, Teeuwisse WM, Nederveen AJ, van Osch MJ (2011) Robustness and reproducibility of flow territories defined by planning-free vessel-encoded pseudocontinuous arterial spin-labeling. Am J Neuroradiol. doi:10.3174/ajnr.A2410
9. Jung Y, Rack-Gomer A, Wong E, Buracas G, Liu T (2009) Pseudo-continuous arterial spin labeling with optimized tagging efficiency for quantitative ASL fMRI. In: Proceedings 17th scientific meeting, ISMRM, Honolulu, p 1578
10. Jahanian H, Noll DC, Hernandez-Garcia L (2011) B(0) field inhomogeneity considerations in pseudo-continuous arterial spin labeling (pCASL): effects on tagging efficiency and correction strategy. NMR Biomed. doi:10.1002/nbm.1675
11. Jung Y, Wong EC, Liu TT (2010) Multiphase pseudocontinuous arterial spin labeling (MP-PCASL) for robust quantification of cerebral blood flow. Magn Reson Med 64(3):799–810
12. Wong EC, Guo J (2011) Blind detection of source vessel locations and resonance offsets using randomly encoded VEASL. In: Proceedings 19th scientific meeting, ISMRM, Montreal, p 294
13. Kansagra AP, Wong EC (2008) Mapping of vertebral artery perfusion territories using arterial spin labeling MRI. J Magn Reson Imaging 28(3):762–766
14. Kansagra A, Wong E (2009) Automated segmentation of multiple vascular territories from vessel encoded pseudo-continuous arterial spin labeling MRI data. In: Proceedings 17th scientific meeting, ISMRM, Honolulu, p 3652
15. Wong E, Kansagra A (2008) Mapping middle cerebral artery branch territories with vessel encoded pseudo-continuous ASL: sine/cosine tag modulation and data clustering in tagging efficiency space. In: Proceedings 16th scientific meeting, ISMRM, Toronto, p 182
16. Chappell MA, Okell TW, Jezzard P, Woolrich MW (2010) A general framework for the analysis of vessel encoded arterial spin labeling for vascular territory mapping. Magn Reson Med 64(5):1529–1539
17. Chappell MA, Okell TW, Jezzard P, Woolrich MW (2009) Vascular territory image analysis using vessel encoded arterial spin labeling. Med Image Comput Comput Assist Interv 12(Pt 2):514–521

Acknowledgements

Chapter 4, in full, is a reprint of the material as it appears in Magnetic Resonance Materials in Physics Biology and Medicine 2012. Wong EC, Guo J. Blind detection of vascular sources and territories using random vessel encoded arterial spin labeling. Magn Reson Mater Phy. 2012 Apr;25(2):95-101. doi: 10.1007/S10334-011-0302-7. The dissertation author was a co-investigator and co-author of this paper.

CONCLUSION

Development of VSASL along with other mainstream ASL techniques

Since the invention of ASL, the past 22 years have seen tremendous technical development on ASL labeling methods, imaging techniques and extensive validation against other perfusion imaging methods. Recently, an ASL "white paper" has been published for the recommendation of ASL techniques to use in clinical settings (1), where basic PCASL and PASL are relatively mature and well-validated, therefore recommended in clinical settings. In contrast, as a relatively newly invented technique, VSASL is considered in development at current stage and needs additional validation for routine clinical use.

The first part of my dissertation (Chapters 1 and 2) has been devoted to development of VSASL in two main aspects: Chapter 1 focuses on development of a robust VS labeling module with B_0 and B_1 insensitivity and minimized EC effects; Chapter 2 focuses on development of a labeling strategy using multiple VSS modules for maximized SNR efficiency.

In Chapters 1, the sym-BIR-8 VSS design was demonstrated to be the most robust VSS module across two scanners from different vendors among all the VSS modules tested (2). Its superior performance on reducing ECs with long time constants comes from the symmetry in the design, while the ECs with short time constants are mainly suppressed by inserting delays after each gradient pulse. These two main principles to reduce EC effects are applicable across different scanners even if they may have dramatically different EC characteristics (amplitude, time constant, etc.), as I have shown that was the case in Chapter 1. However, this does not mean that the sym-BIR-8 cannot be adjusted flexibly to best match the actual EC properties of a scanner. For example, the symmetry of the module can be slightly relaxed to allow adjustment

of the amplitude and timings of the gradient pulses, in order to optimally reduce the effects of ECs of a specific range of time constants.

In addition to the two main principles above, the usage of "mild" gradient pulses, i.e., lower amplitude and longer ramp time, but longer duration to keep the first moment constant, also helps reduce EC effects. However, inserted delays and prolonged gradient pulses also increases the duration of the VSS module, resulting in additional T_2 relaxation during VS preparation thus reduced labeling efficiency and SNR. However, this SNR loss is small and can be compensated by using mm-VSASL labeling strategy as presented in Chapter 2, or acquiring more data to average as a second choice. The need for artifact-free and accurate quantification of perfusion outweighs the small SNR loss by lengthening of the VSS modules. With the design consideration and tradeoff mentioned above, sym-BIR-8 VSS is the most robust recommended for VSASL.

In Chapter 2, I have demonstrated that using multiple VSS modules can significantly improve the SNR efficiency of VSASL to an extend even comparable to that of PCASL with labeling parameters recommended for clinical use (1). However, this is not to state that VSASL is a replacement for the mainstream ASL techniques such as CASL/PCASL and PASL. Currently PCASL is recommended for clinical use because of its superior SNR efficiency, especially when the TDs are not too long (< 2s) and relatively short PLDs are sufficient for accurate perfusion quantification. This may be the most frequently encountered case for healthy subjects or in most of the applications ASL has been used (1). However, aging (3) or vascular diseases such as steno-occlusive disease (4) and Moyamoya disease (5) can prolong the TDs significantly. On one hand, the conventional ASL techniques such as PASL, PCASL may not be recommended in these cases (4,5); on the other hand, combined with TD insensitivity and improved SNR efficiency using mm-VSASL technique (6), VSASL should be a preferred alternative in these cases, or maybe the only alternative when the TDs are extremely long. In

this sense, VSASL may serve more as a complementary ASL technique to the mainstream ASL techniques such as PCASL in routine clinical setting. In cases of very long TDs caused by aging and/or vascular diseases, VSASL should be most suitable for accurate and efficient perfusion measurement, supported by a preliminary study on Moyamoya patients (5).

As mentioned earlier, VSASL is still in development and more validation is required before routine clinical use. In addition to validation of VSASL against other ASL/non-ASL techniques, further technical development may help prepare VSASL for more clinical studies. There may be further improvement on the SNR efficiency by development of VS preparation. As discussed in Chapter 2, if each VSS module has less SNR loss, using multiple VSS modules can achieve more SNR improvement. It is possible that even more VSS modules (>2) can be used to further improve the SNR efficiency. However, the need for EC reduction usually results in longer VSS preparation duration, so there is a tradeoff between a shorter VSS module duration and a more robust EC reduction to make. Another way of improving the labeling efficiency of VSASL is to use inversion instead of saturation. The inversion of spins with a wide range of velocities is technically challenging. There have been some attempts to tackle this problem, including our lab (7,8), but with only limited success so far.

As the research and development of VSASL advances, more reports of application and validation of VSASL may be expected, along with the acceptance of the mainstream ASL techniques by both the research and clinical communities.

VSEAN and future development

The second part of this dissertation (Chapter 3) is on application of a modified VS preparation (VSE) in measurement of venous oxygenation. As demonstrated in the chapter, the VSEAN method is capable of conducting true *in situ* venous oxygenation measurement which only qBOLD and QUIXOTIC methods can do, but without the complex modeling and fitting of

the signal in qBOLD, or the suboptimal SNR and contamination from CSF. The oxygenation estimates in sagittal sinus (SS) using VSEAN were consistent with that using TRUST, a more established method of measuring venous oxygenation in SS. Results from the experiments involving a hypoxic mixture had validated VSEAN's capability of measuring venous oxygenation changes.

There are aspects of VSEAN technique to be further improved. Firstly, implementation of multi-echo SE T_2 measurement will allow VSEAN to yield oxygenation information every TR, significantly improving the SNR efficiency and the temporal resolution of this technique. Currently the T_2 measurement is done via T_2-preparation, which can only yield venous information every a few TRs. This is fundamentally challenging, because on one hand the phase information in the signal is used to differentiate venous signal from static tissue signal; on the other hand the multi-echo SE T_2 acquisition induces different phase condition on the venous signal and static tissue signal. To tackle this problem, different phase alternation strategies can be applied to the refocusing pulse train, e.g., CPMG SE train, CP SE train, and CP SE train with phase alternation patterns such as MLEV-4, MLEV-8, MLEV-16 (9) or XY-4, XY-8, XY-16 (10). Our preliminary results showed that CP SE train with XY-4 phase alternation pattern might be a good candidate for multi-echo SE T_2 measurement. In addition, B_1-insensitive refocusing pulse trains, such as BIR-4, DRHS pulses, may be used in combination with the XY-4 phase alternation to improve the robustness of the measurement against B_1 variation. As multiple refocusing pulses are used, there may be artifacts generated by stimulated echoes. To minimize these artifacts, spoiler gradient pulses around the refocusing RF pulses may be arranged as recommended in (11).

Secondly, for a better coverage of the brain tissue, implementation of 3D image acquisition may be a better choice for VSEAN than 2D multi-slice acquisition, because in this way, the whole volume can be acquired at the null point of the arterial blood, therefore free of

contamination from arterial signal. Thirdly, as the venous signal is intrinsically low-SNR, optimal sampling strategy (12) may be used in designing of the T_2 acquisition for a more robust measurement of T_2. This is applicable in both T_2-preparation and multi-echo SE T_2 methods.

Re-VEASL and **future development**

In the last part of the dissertation (Chapter 4), a development in VEASL using unipolar encoding gradients and randomized encoding strategy has been demonstrated to be truly plan-free and capable of providing accurate vessel territory information for labeling below and above the CoW. The use of randomized encoding gradients makes VEASL immune to inaccurate CBF quantification caused by off-resonance effect, as the off-resonance is accounted in the model and its effect can be compensated in the fitting process. This technique is capable of detecting collateral flows even if the source vessels are unknown in advance of imaging. This is particularly important in clinical setting, because it helps avoid neglecting any possible source arteries in the first place, therefore saving the possibility of rescanning the patient. As the re-VEASL technique is plan-free, it should be able to save precious scanning time because typically the planning is performed during the scanning session, or avoid potential errors made in the process of planning.

In the study presented in Chapter 4, the re-VEASL data were collected with a series of randomized encoding steps based on our empirical knowledge of the locations of source vessels. It should be helpful to include some prior knowledge about the distribution of the locations of the vessels from a realistic atlas in the process of designing the randomized encoding steps, such as an atlas in (13). As the parameters for generating randomized encoding steps can be adjusted to best reflect the characteristics of the vessel locations in the labeling plane, e.g., below or above the CoW, where the number of target vessels and the separation between vessels are different, it makes sense to utilize different pre-generated randomized encoding steps for

labeling vessels in these frequently chosen labeling planes for a “customized” and more optimal encoding efficiency.

References

1. Alsop DC, Detre JA, Golay X, Gunther M, Hendrikse J, Hernandez-Garcia L, Lu H, Macintosh BJ, Parkes LM, Smits M, van Osch MJ, Wang DJ, Wong EC, Zaharchuk G. Recommended implementation of arterial spin-labeled perfusion MRI for clinical applications: A consensus of the ISMRM perfusion study group and the European consortium for ASL in dementia. Magn Reson Med 2014. doi: 10.1002/mrm.25197.

2. Guo J, Meakin JA, Jezzard P, Wong EC. An optimized design to reduce eddy current sensitivity in velocity-selective arterial spin labeling using symmetric BIR-8 pulses. Magn Reson Med 2014. doi: 10.1002/mrm.25227.

3. Liu Y, Zhu X, Feinberg D, Guenther M, Gregori J, Weiner MW, Schuff N. Arterial spin labeling MRI study of age and gender effects on brain perfusion hemodynamics. Magn Reson Med 2012;68(3):912-922.

4. Mutke MA, Madai VI, von Samson-Himmelstjerna FC, Zaro Weber O, Revankar GS, Martin SZ, Stengl KL, Bauer M, Hetzer S, Gunther M, Sobesky J. Clinical evaluation of an arterial-spin-labeling product sequence in steno-occlusive disease of the brain. PLoS ONE 2014;9(2):e87143.

5. Qiu DQ, Straka M, Zun ZH, Bammer R, Moseley ME, Zaharchuk G. CBF measurements using multidelay pseudocontinuous and velocity-selective arterial spin labeling in patients with long arterial transit delays: Comparison with xenon CT CBF. J Magn Reson Imaging 2012;36(1):110-119.

6. Guo J, Wong EC. Increased SNR Efficiency in Velocity Selective Arterial Spin Labeling using Multiple Velocity Selective Saturation Modules (mm-VSASL). Magn Reson Med 2014. doi: 10.1002/mrm.25462. [In press].

7. Wong EC, Guo J. Velocity Selective Inversion Pulse Trains for Velocity Selective Arterial Spin Labeling. In Proceedings of the 17 th Annual Meeting of ISMRM; Honolulu, Hawai'i, USA. 2009. p. 620.

8. Qin Q, van Zijl PCM. Velocity-Selective Inversion Prepared Arterial Spin Labeling for 3D Whole-Brain Perfusion Measurment. In Proceedings of the 22 th Annual Meeting of ISMRM; Milan, Italy. 2014. p. 420.

9. Shaka AJ, Rucker SP, Pines A. Iterative Carr-Purcell Trains. J Magn Reson 1988;77(3):606-611.

10. Gullion T, Baker DB, Conradi MS. New, Compensated Carr-Purcell Sequences. J Magn Reson 1990;89(3):479-484.

11. Poon CS, Henkelman RM. Practical T2 quantitation for clinical applications. J Magn Reson Imaging 1992;2(5):541-553.

12. Jones JA. Optimal sampling strategies for the measurement of relaxation times in proteins. J Magn Reson 1997;126(2):283-286.

13. Forkert ND, Fiehler J, Suniaga S, Wersching H, Knecht S, Kemmling A. A statistical cerebroarterial atlas derived from 700 MRA datasets. Methods Inf Med 2013;52(6):467-474.